Diffusion phenomena in chemically stabilized multilayer structures

Saskia Bruijn

PhD committee

Chairman:	
Prof. dr. G. van der Steenhoven	University of Twente
Secretary:	
Prof. dr. G. van der Steenhoven	University of Twente
Promotor:	
Prof. dr. F. Bijkerk	University of Twente FOM Rijnhuizen
Assistant promotor:	
Dr. ir. R.W.E. van de Kruijs	FOM Rijnhuizen
Members:	
Prof. dr. ir. H.J.W. Zandvliet	University of Twente
Prof. dr. K.J. Boller	University of Twente
Prof. dr. R.A. Hoekstra	University of Groningen
Prof. dr. ir. W.G. van der Wiel	University of Twente
Prof. dr. P.H.L. Notten	Eindhoven University of Technology

Cover: Picture of a Menelaus Blue Morpho (*Morpho menelaus*) made by Saskia Bruijn in the botanical garden of the University of Utrecht. The butterfly in this picture does not get its beautiful blue colour from pigments, but from diffraction similar to that in the multilayers described in this thesis.

Diffusion phenomena in chemically stabilized multilayer structures
Saskia Bruijn
Thesis, University of Twente, Enschede - illustrated
With references - With summary in English and Dutch
ISBN: 978-94-91211-22-5
Printed by Ipskamp Drukkers (2011)

DIFFUSION PHENOMENA IN CHEMICALLY STABILIZED MULTILAYER STRUCTURES

PROEFSCHRIFT

ter verkrijging van
de graad van doctor aan de Universiteit Twente,
op gezag van de rector magnificus,
Prof. dr. H. Brinksma,
volgens besluit van het College van Promoties
in het openbaar te verdedigen
op woensdag 27 april 2011 om 16:45 uur

door

Saskia Bruijn

geboren op 30 november 1980
te Strijen

Dit proefschrift is goedgekeurd door de promotor

Prof. dr. F. Bijkerk

en de assistent promotor

Dr. ir. R.W.E. van de Kruijs

Nature composes some of her loveliest poems for the microscope and the telescope.

-Theodore Roszak, Where the Wasteland Ends, 1972

This work is part of the FOM Industrial Partnership Programme I10 (XMO) which is carried out under contract with Carl Zeiss SMT GmbH, Oberkochen and the ‘Stichting voor Fundamenteel Onderzoek der Materie (FOM)’, the latter being financially supported by the ‘Nederlandse Organisatie voor Wetenschappelijk Onderzoek (NWO)’. We also acknowledge financial support from Agentschap NL (EXEPT project).

Inhoudsopgave

Chapter 1

Introduction

1.1 Multilayered structures

In recent years there has been great interest in multilayer structures. Smartly chosen combinations of thin layers of two or more materials combined in such structures can have extraordinary new properties. For instance, multilayered structures can have much higher mechanical strengths than single layers of similar total dimensions [1, 2]. By layering materials, the advantageous properties of the two separate materials can be combined. As an example, a hard but brittle material can be combined with a flexible material in a multilayer stack, to obtain hard, yet flexible properties. Another example of the beneficial use of multilayered structures is from the field of spintronics, where novel material properties such as giant magnetoresistance [3] have emerged. Where magnetoresistance is a bulk material property that results in a small resistance change by applying a magnetic field, giant magnetoresistance shows a much larger resistance change by combining nanometer thin layers of ferromagnetic and anti-ferromagnetic materials in a multilayered structure. In this thesis, however, we will focus on the optical properties of thin film multilayered structures. Especially on their ability to function as Bragg reflectors to reflect short wavelength radiation, so called multilayered optics.

1.1.1 Multilayer optics

Nature provides us with original examples of complex, multilayered structures, which will be used to explain the principle behind multilayer optics. The butterfly shown on the cover of this thesis is a Menelaus Blue Morpho (*Morpho menelaus*). Its brilliant bright blue colour does not originate from pigments in its wings, as is the case in most other butterflies. Instead, its wings are build from ridges, which can be seen in figure 1.1a. A cross section of a ridge consists of a structure of several lamellae

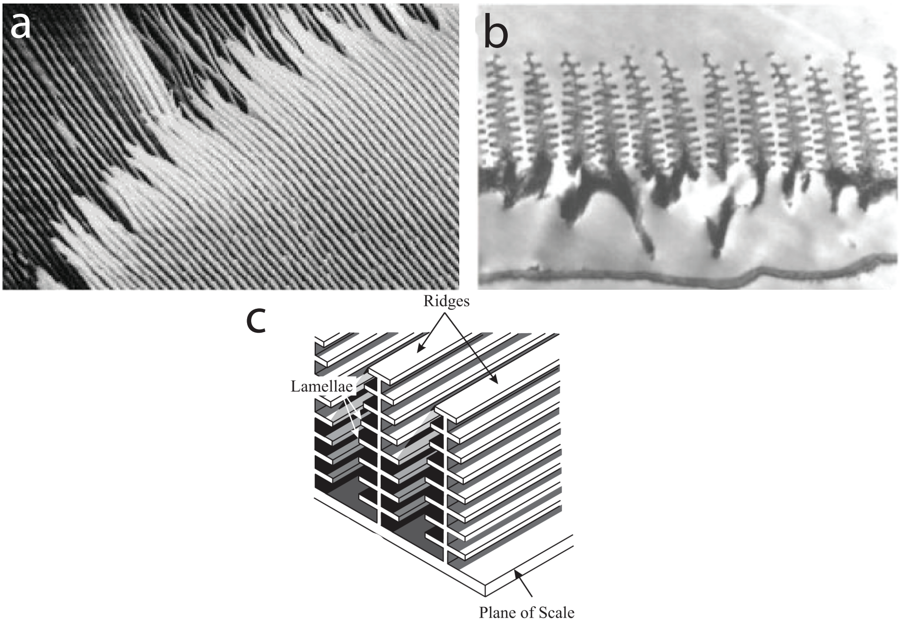

Figure 1.1: Wing of a Morpho butterfly. In figure *a* we see a TEM image of the ridges in the wing [7]. In figure *b* we see a cross section of such a ridge [8] and in *c* a schematic graph of the ridges and lamellae [4].

which have approximately the same distance from each other. The cross section of a ridge is shown in figure 1.1b. A schematic drawing of the ridges and lamellae from the paper of Smith [4] is included in figure 1.1c. The lamellae work as a Bragg reflector* [4, 6, 7] where at every layer a part of the incoming light is reflected. Only the wavelength that obeys Bragg's law, in this case blue light, will show positive interference and will be observed by us. In its simple form, Bragg's law is defined as:

$$m\lambda = 2d \sin\theta \tag{1.1}$$

where m is an integer, λ is the wavelength of the radiation which is reflected, d is the period of the layers and θ is the angle of incidence (with respect to the surface plane). The spacing of the layers in the wing of the butterfly is exactly half that of the wavelength of blue light, so due to positive interference the wings look blue at a near-normal angle of incidence. When one looks at the butterfly from a more glancing angle, the wings appear to be more violet in colour, because θ becomes smaller and the reflected wavelength (λ) is smaller according to equation 1.1. This change in colour is why they are called Morpho (changing) butterflies.

The example of the Menelaus Blue Morpho butterfly shows how we can reflect

---

*It is noted that the ridges do not function as a diffraction grating, since their height is irregular [4, 5].

light by using a periodic structure. In the case of the Menelaus Blue Morpho butterfly a wavelength of 450 nm is reflected. The multilayer structures studied in this thesis are designed for reflecting extreme ultraviolet (EUV) radiation, which has a wavelength around 13.5 nm. The EUV is generally denoted as a part of the wider XUV band, ranging from few tens to few tenths of nanometers, but the nomenclature is not consistent in literature. In the EUV, and in general also in the full XUV wavelength region, all materials have a very high absorption, making it impossible to use refractive optics (lenses). Therefore, reflective mirrors are the only practical option to focus, defocus or 'control' light at angles above the critical angle for total reflection, θ_c [†] [9].

In general the theoretical reflectance from a completely smooth interface is dependent on the refractive index difference between the two interfaces. The refractive index is defined as:

$$n = 1 - \delta + i\beta, \tag{1.2}$$

where δ is the real part of the refractive index and β the imaginary part. The constant β relates to the absorption in the material. Since the refractive index is close to unity for all materials in the XUV regime, one interface only reflects a few percent of the radiation, therefore many interfaces reflecting in phase are needed to obtain a high reflection, a condition which can be fulfilled using a multilayer stack. From one single interface the reflectance will be highest if the two materials have a high optical contrast, or a high Δn. The absorption (β) in the material needs to be as low as possible and therefore, to make the difference in n as large as possible, the difference between the δ values of the materials must be as high as possible. So a multilayer mirror should have alternating layers of high and low δ, which is schematically represented in figure 1.2.

An important wavelength in the XUV regime is 13.5 nm, since this wavelength will be applied in EUV lithography (EUVL), which will be discussed in section 1.2. Figure 1.3 shows the optical constants of different materials for a wavelength of 13.5 nm. The materials most often used at this wavelength are Mo and Si, because they have a large difference in δ and a relatively low absorption (β). For a Mo/Si multilayer mirror with 50 periods and perfectly sharp interfaces this results in a theoretical reflection of 74%. In reality, the reflection is limited to approximately 70%, because the interfaces of the multilayer structures are not perfectly sharp, due to stochastic deposition and growth effects, silicide formation during deposition, materials intermixing, crystallization, roughness, etcetera. An example of a reflectance curve for a Mo/Si multilayer optical coating is shown in figure 1.2.

1.2 Application of multilayer optics

Multilayer XUV optics are in principle useful in all applications where short wavelength radiation is used and where the light needs to be focused, defocused or made

---

[†] At angles below θ_c all light is reflected from the surface. The critical angle is given by $\sin\theta_c \simeq \sqrt{2\delta}$. Since n is close to unity in the XUV regime, this angle is small.

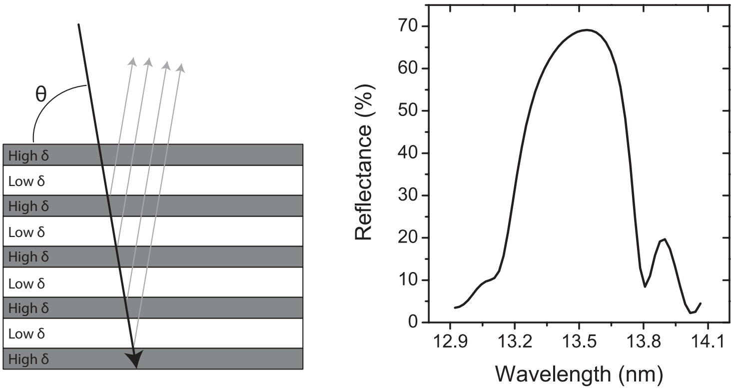

Figure 1.2: Left: Schematic picture of a multilayer mirror. Right: example of the reflectance curve of a Mo/Si multilayer [10].

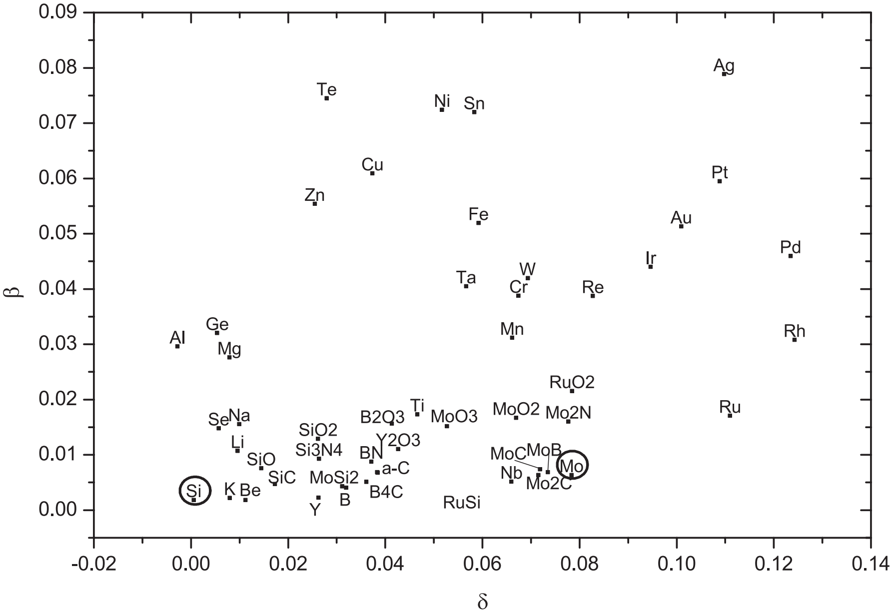

Figure 1.3: The real (δ) and imaginary (β) parts of the refractive index for several materials at a wavelength of 13.5 nm.

monochrome. Examples are space telescopes [11], synchrotron beam-lines, free electron lasers (FELS) in the X-ray regime and in future lithography equipment. This section further focusses on the latter two applications, with an emphasis on future lithography equipment; the work is highly motivated by the application in lithography. The research in this dissertation is done in the framework of the FOM-programme 'XMO', which is partly financed by Carl Zeiss in Oberkochen, Germany.

1.2.1 Extreme Ultraviolet Lithography

Photolithography is well known as a technique for manufacturing integrated circuits, as in the semiconductor industry. In the photolithography process a light source illuminates a reticle or mask, which has a pattern on it. This object is then demagnified and projected onto a Si wafer, coated with a layer of photoresist (photo-sensitive lacquer). The pattern is then transferred onto the wafer and etched correspondingly. For most integrated circuits, several steps of illumination and deposition of different materials are needed to build a complex layered structure. These integrated circuits can for instance be used in laptops and mobile phones.

The maximum resolution (R) that can still be resolved in a microscopic system is given by the Rayleigh criterion [9]:

$$R = \frac{0.610\lambda}{NA}, \tag{1.3}$$

where NA is the numerical aperture, which is defined as $n \sin \omega$, with ω the acceptance angle of the microscope and n the refractive index of the surrounding medium (for air $n = 1$). The factor 0.610 originates from the principle properties of a perfect lens [12]. For the, complicated, lithography systems the equation is written as [13]:

$$R = k_1 \frac{\lambda}{NA}, \tag{1.4}$$

in which k_1 is an empirical process constant. At this moment ultraviolet laser light with a wavelength of 193 nm is primarily used for photolithography. The so-called immersion lithography variant, in which the final lens element and the wafer are connected by a thin water film, is becoming the mainstream technology in lithography. Since water has a higher n than air (1.33 and 1 respectively), this will increase the NA to above 1, and increase the resolution (see equation 1.4). But, to continue the development of increasing the number of transistors on an integrated circuit, a switch to a shorter wavelength is unavoidable.

The next generation of lithography equipment currently in development will likely use a wavelength of 13.5 nm, which is currently being introduced and scheduled for mass chip fabrication around 2013 [14]. Given this major reduction in wavelength, the lenses in the system need to be replaced by reflective imaging optics. A schematic picture of such EUV lithography (EUVL) equipment can be seen in figure 1.4. The light source of an EUVL machine can no longer be a laser, and the light originates from a source that makes use of a Sn or Xe plasma, which strongly emits (among many other wavelengths) 13.5 nm radiation. The plasma can be produced

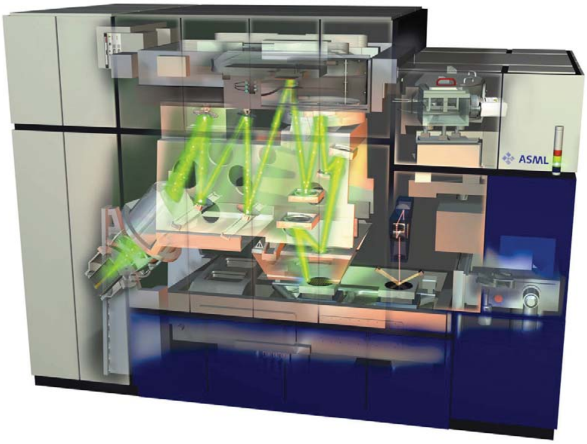

Figure 1.4: Schematic view of an example of extreme ultraviolet lithography apparatus as made by ASML and Carl Zeiss.

either by laser illumination or using a discharge, with different producers of such sources.

The entire optical path may consist of as many as 10 mirrors, which makes the reflectivity of the individual mirrors very important. If the reflectance from all optical elements would for instance reduce from 70% to 65%, the total transmission of the optical train would reduce with more than 50%. On the other hand if the reflectivity of the multilayer optics could be increased from 68% to 70%, for instance by using improved diffusion barrier layers, the total transmission could increase by 33%.

The reflective properties of a multilayer can be very sensitive to surface contamination and/or small changes in the internal structure. The reflectance can for instance reduce due to the formation of an unavoidable layer of several contamination materials, which are present in the vacuum and are deposited on the mirror during operation. The contamination originates from the other parts in the vacuum vessel, like hydrocarbon outgassing from the photoresist (which forms a carbon layer), Sn from the source [15–17], and oxidation due to residual oxygen in the chamber. The contamination can be mitigated by hydrogen cleaning [17, 18], but such cleaning procedures come at the cost of added system complexity and reduced uptime. Residual oxygen in the system can oxidize the first layers of the multilayer, which is a problem because of increased EUV absorption as well as changing reflection coefficients (see the higher β values for oxides in figure1.3). A solution for oxidation may require a capping layer of a noble material [19, 20], but these materials usually have a higher absorption coefficient as well.

1.2.2 Free electron lasers

An other possible application for multilayer optics are fourth generation light sources such as free electron lasers (FELS) working in the soft X-ray regime. Free electron lasers produce pulsed (typically 10-100 fs), coherent, extremely bright radiation. Multilayers can be used in these new free electron lasers to focus, monochromate or transport the radiation [21]. The radiation in a FEL can be used to study for instance biomolecules and dynamics of chemical reactions. These examples are discussed below. The principle behind the functioning of XUV FELS is often based on Self-Amplified Spontaneous Emission (SASE) which will be discussed in section 2.2.2.

One of the examples of the use of FEL radiation is the comprehensive structural analysis of large biomolecules (for instance proteins) [22]. At the moment, the structure of biomolecules is usually determined by crystallizing the molecule and analyzing the diffraction pattern. This is a powerful tool, but many biomolecules do not crystallize and the structure of the crystallized biomolecule might be different from the structure in vivo. In order to study a single molecule one should choose a short wavelength to obtain enough resolution (equation 1.3). Furthermore, the total intensity scattered from the molecule should be high enough to form an image. This high intensity poses a problem, since radiation damage could change the molecule before it can be fully measured. Chapman et al. [23] showed that, using FEL radiation of 32 nm, an image of an object can be made *before* the object is destroyed by the radiation. In this experiment the diffraction image was projected on a CCD camera using a multilayer mirror. The image is later reconstructed from the diffraction image with an iterative algorithm [24]. The imaged object in that study had a size of a few microns, which is convenient for analysis. Such imaging thus forms a promising technique for imaging biomolecules at shorter wavelengths than 32 nm.

In the previous example, the FEL radiation is used to image a *static* molecule. With the fs pulses from a FEL we can on the other hand also study the *dynamics* of (bio-)chemical reactions in a pump and probe experiment. In this case the reaction is triggered/induced by a first (pump) pulse and a short time later, the molecule is imaged by a second (probe) pulse to observe the changed configuration. The time delay between the pump and probe pulses are varied to observe the full reaction process. The short wavelengths in the FELS allow for imaging of individual molecules, as is discussed in the previous paragraph. The short pulses ensure minimal changes within the molecule during the pulse.

Since the intensities are much higher and the pulse durations much shorter in FELS than those expected in for example EUVL, the damage mechanisms in multilayer optics can also be very different. In the study described in chapter 7 we investigate the damage mechanisms in MoN/SiN multilayers when irradiated with FEL radiation from the FLASH FEL source (Hamburg) [25, 26]. The damage mechanisms are compared to samples which are annealed in a vacuum oven. A similar comparison between damage from annealing and FLASH radiation is made in a separate paper [27] on Mo/Si multilayer structures. In both cases the damage threshold for a single pulse is determined in order to find a working range in FELS for multilayer optics. Mo/Si was selected because it is a very well studied system [28–31].

MoN/SiN on the other hand was selected because it has shown to be very temperature resilient in annealing experiments [32] and therefore a high damage threshold was expected.

The comparison between damage caused by radiation and damage caused by thermal annealing only, is considered to be relevant for EUVL as well. The studies on stability of multilayer optics have up to now always been performed by thermal annealing. This presumes that the absorption of radiation in applications will cause no other damage than the damage caused by increased temperature. The high intensity pulses from a FEL are an extreme case, and they permit the study of a much accelerated degradation compared to the relatively moderate peak intensity sources employed in EUVL. The paper from Khorsand et al. [27] showed that for Mo/Si multilayers the damage mechanism (i.e. crystallization and silicide formation) is thermally induced, and actually the same for annealing and irradiation with FEL radiation. This suggests that thermal annealing is a good technique to study effects of EUV induced Mo/Si multilayer damage, but much slower than FEL studies. In chapter 7 we investigate if this is true for MoN/SiN multilayers as well.

1.3 Radiation induced thermal damage

Mo and Si have relatively low absorption coefficients (figure 1.3) at wavelengths around 13.5 nm. Nevertheless, the Mo and Si layers absorb a part of the radiation, which will cause the multilayer optics to heat up during applications, which might lead to intermixing of the individual thin films. The different mechanisms for these types of damage are discussed in this section.

1.3.1 Thermal damage in Mo/Si multilayer optics

An important threat to the reflectance of multilayer optics is silicide formation at the interfaces at enhanced temperatures [33]. The Mo and Si layers in a multilayer form silicides already upon deposition [29], due to the negative formation enthalpy of most silicides. The formation enthalpies of molybdenum silicides are listed in Table 1.1.

Table 1.1: The formation enthalpies of the most common molybdenum silicide compounds [34].

Compound	ΔH (kJ/mol of atoms) [†]
$MoSi_2$	-44
Mo_5Si_3	-39
Mo_3Si	-27

[†] These enthalpies are expressed in the unconventional unit of kJ/mol of *atoms*. The more common unit of kJ/mol is difficult to use, since each compound has a different amount of atoms in the stoichiometry. This unit is therefore the most honest comparison.

The formation of silicides not only reduces the optical contrast between the Mo and Si layer, it also changes the period of the multilayer [35], due to increased density of the silicides compared to the average density of the Mo and Si layers. This changes the Bragg conditions of the mirror and reduces the reflection at the desired wavelength significantly. For example, for a multilayer designed for 13.5 nm radiation, a change in the period of 1 Å can reduce the reflectance at 13.5 nm from 70% to 50%. In EUVL, a change in reflectance of one percent is already too large, which means that the period may not change more than approximately 20 pm. Therefore the period has to be controlled with a precision of several picometer, during deposition and also during usage. Preventing such diffusion induced silicide formation is therefore crucial for developing multilayer coatings. The general theoretical and experimental procedures used in diffusion in solids and in multilayered structures will be discussed in the next sections.

1.3.2 Diffusion in solids

Diffusion of atoms (A) through a solid (B) can be described by Fick's law, in which the diffusion flux (J) of the atoms is dependent on the gradient of the concentration of the atoms (C). This can be written as Fick's first law:

$$J = -D\nabla C. \tag{1.5}$$

In this equation D is the diffusion coefficient, which is dependent on the material properties of A and B, the temperature and the concentration of A. In a simple system we may also presume that the total amount of atoms A is constant. This is not always the case (which we will see later), since atoms may for instance react to form compounds or escape in gas form. For a constant amount of atoms A, the following condition should be met:

$$-\nabla \cdot J = \frac{\delta C}{\delta t}, \tag{1.6}$$

Which leads in combination with equation 1.5 to Fick's second law:

$$\frac{\delta C}{\delta t} = \nabla(D\nabla C). \tag{1.7}$$

From this equation, the time dependent concentration of A in B can be calculated.

The diffusion constants determined with Fick's law are temperature dependent, since the mobility of atoms is higher at higher temperatures. The temperature dependence of the diffusion constant can often be described by the Arrhenius equation, which is given by

$$D = D_0 \exp \frac{-E_a}{kT}, \tag{1.8}$$

here D_0 is the pre-exponential factor, E_a is the activation energy, k is the Boltzmann constant and T is the temperature in Kelvin. By using the Arrhenius equation the diffusion constants can be scaled with temperature, assuming E_a is constant.

To describe diffusion in thin film solids it is important to know the diffusion constants. The most straightforward way to find these is to measure the concentration profile over time, which is usually done in a two step process. In a first step a layer of the diffusing species is deposited on the substrate. Secondly the sample is annealed, to diffuse the deposited atoms. The atomic concentration before and after annealing then can be measured by X-ray photoelectron spectroscopy (XPS, see section 2.4), low energy ion scattering (LEIS), secondary ion mass spectroscopy (SIMS), radioactive tracer techniques (RTT), and other methods [36, 37].

With XPS and LEIS, the concentration profile can be measured non-destructively within the probe depth of the technique (typically 10 nm), but interpreting this as a depth profile is often not easy. Therefore in most techniques, the concentration is measured layer by layer, while in between (for thin layers) ion beam sputtering is used to sputter off a fixed amount of material. Ion beam sputtering is destructive and can in itself induce extra intermixing, which can distort the results. For layer thicknesses below approximately 5 nm ion sputtering is not suitable, since, due to the extra intermixing caused by the ion sputtering, the concentration can not be determined with adequate resolution anymore. This is clearly seen in figure 2.5, where ion sputtering is combined with XPS measurements.

When we want to measure the diffusion of an atom in a medium which is a compound containing the same atom, a distinction between the compound and the diffusing atom can be made by depositing an isotope of this material. This can be done by radioactive tracers (in case of RTT) or with isotopes with a certain mass (SIMS). But also in these cases, the analysis of the results is destructive, since during the analysis ion beam sputtering is used to analyze the sample layer by layer. In the case of RTT the radioactivity of the sputtered material is measured, in the case SIMS the mass is analyzed.

The above described methods are not suitable for measuring the diffusion profiles directly in multilayered structures with the precision which is needed for the applications (no changes larger than a few pm). For this we need to find an other method.

1.3.3 Diffusion in multilayers

Except for the direct methods of measuring the diffusion coefficient, there are other methods that are more indirect. One of these involves the use of a multilayer of two alternating materials and measuring the intensity decrease of the first order Bragg peak of the grazing incidence X-ray spectroscopy (GIXR) spectrum. This method was introduced by DuMond and Youtz [38] and has since then been used by other authors on different multilayer systems [39–41]. The method assumes a simple sinusoidal function to describe the concentration profile of the two constituents of the multilayer. The diffusion coefficient D can in this case be written as:

$$D = -\frac{p^2}{8\pi^2}\frac{d}{dt}ln\frac{I}{I_0}, \tag{1.9}$$

with p the period of the multilayer, I the intensity of the first order Bragg peak at a specific time, t and I_0 the intensity of the first order Bragg peak before annealing. The derivation of this equation can be found in [38, 39].

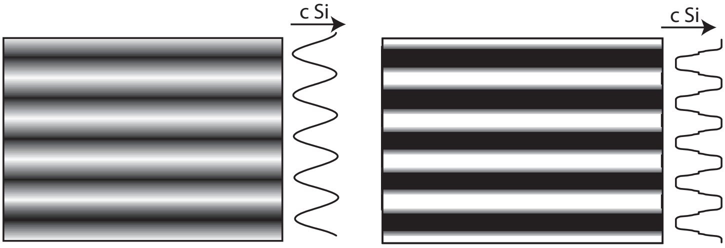

Figure 1.5: Left: Model of a multilayer as proposed by DuMond et al [38], assuming a sinusoidal concentration profile. Right: A more realistic view of a multilayer, including the silicide interfaces.

Obviously, the method described in the previous paragraph is most suitable for EUVL multilayer optics, since the direct methods do not have the high resolution required for this application. However, the assumption of a sinusoidal function may in this case present a problem. It is well known that Mo/Si multilayers form silicides at the interfaces, which are already present directly after deposition and will further grow during annealing [29, 35]. This means that there is not just a gradient of concentrations on the interfaces, but a more complex density/concentration profile should be taken into account. This is illustrated in figure 1.5, where we see the sinusoidal concentration gradient on the left side and the reality, with a silicide interface, on the right.

The fact that a silicide grows at the interfaces poses a problem in Fick's law as well, since there is a sink of atoms which react to form silicides, which makes equation 1.6 invalid. We end up with a system in which there is a diffusion-reaction mechanism. The Mo or Si atoms first diffuse through the silicide interface and then react to form more silicide. The thickness of the silicide is therefore constantly increasing, making this a moving boundary problem. For this reason we propose a different method of following diffusion *in-situ*. This is described in detail in chapter 5 and section 2.3.4. In this new method we measure the change of period in the multilayer during annealing with X-ray reflection. Since the measurements are performed *in-situ* inside the reflectometer, the period change can be followed with high precision and time resolution. The change of the period is a measure for the amount of formed interface in the multilayer structure [31]. Since the interface growth is caused by diffusion, the diffusion coefficients can be determined from this data.

The growth of a compound layer with a diffusion-reaction mechanism can be described with a more empirical model, which has been discussed by Gösele et al. [42]. In this model the two diffusing materials react to form a compound interlayer. This interlayer then acts as a diffusion barrier for further diffusion. The diffusion and reaction are regarded as two separate processes. Since the compound through which the atoms need to travel, is growing over time, the rate of interface formation is expected to reduce over time. In this process there are two limiting regimes. In the beginning, when the silicide interlayer is still thin, diffusion is fast and therefore the interface growth is reaction limited. The interface growth should be linear with time in this regime [42]. After some time, the interface has become so thick that the diffusion through the interface becomes the rate limiting step. This is the diffusion limited regime and interface growth is quadratic with respect to time in this regime [42, 43]. The application of this model to multilayers will be discussed in more detail in chapter 5. The method itself is used to describe the properties of B_4C diffusion barriers in chapter 6.

1.3.4 Diffusion barriers

In order to meet the requirements of many thin film applications, the interface between layers often require extreme sharpness and low atomic roughness. In practice, the interfaces in thin films are almost never atomically sharp, since interdiffusion during production or during usage will cause intermixing at the interfaces, especially at enhanced temperatures. Therefore, in many applications diffusion barriers are introduced between layers to reduce diffusion at the interfaces, requiring materials with a very low diffusion coefficient. Furthermore, the barrier material should be thermodynamically stable with respect to the layer materials, implying the absence of compound formation. In the case of multilayer optics, also the optical properties of the barrier layer should be considered; the layer should not have a high absorption coefficient and preferably improve the optical contrast between the main layers. Since the barrier layer often needs to have sub-nanometer thickness, the layer growth properties are also important, demanding smooth, closed layer growth, and proper adhesive properties with respect to growth on the other materials in the multilayer stack.

In practice the diffusion barrier can also work if the barrier is not fully thermodynamically stable. A possible compound formed at that interface can actually reduce the chemical potential of the atoms in the interface. This will reduce the reaction rate with the other multilayer materials and therefore slow down interface formation. In this case the barrier works not (or not only) as a physical barrier with low diffusion coefficients, but instead as a sacrificial material, sometimes referred to as a chemical diffusion barrier.

In Mo/Si multilayers the most commonly used diffusion barriers are B_4C [33, 44–48], Si_3N_4 [31, 49], C [50, 51] and Mo_2C [52]. It is also possible to replace the entire layer with a thermodynamically more stable compound. Examples of this are, Mo_2C/Si [52], Mo/SiC [53, 54] and MoN/SiN [32] multilayer structures. In this thesis multilayers with Si_3N_4(chapter 3) and B_4C (chapter 4 and 6) diffusion barriers are being investigated. In chapter 7 we study the physics in a MoN/SiN multilayer irradiated with high intensity 13.5 nm radiation.

1.3.5 Diffusion and crystallinity

The crystalline structure of a material can easily influence its material properties. One very striking example is the difference between graphite and diamond. Although both consist of pure carbon, properties such as the optical constants, the wear re-

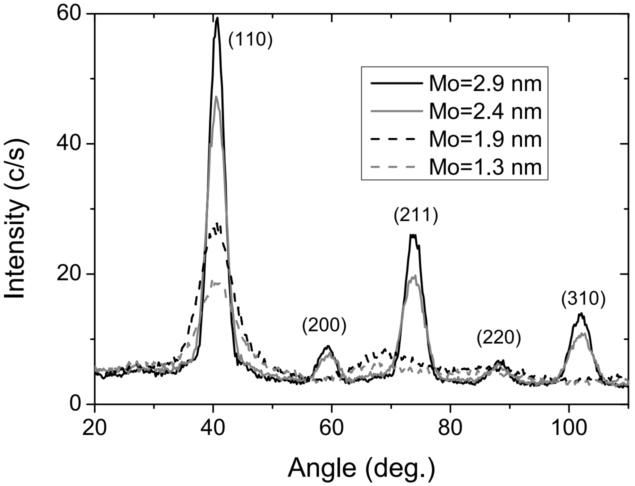

Figure 1.6: XRD spectra of Mo/Si multilayers with 4 different Mo thicknesses. The Miller indices for bcc Mo are given with the peaks.

sistance and thermal conductivity, are dramatically different. An example more close to the subject of this thesis is the so called phase transformation in Mo/Si multilayers. During diffusion amorphous $MoSi_2$ grows at the interfaces, at a certain critical thickness of the interfaces, crystallization of the $MoSi_2$ layer is observed, which is followed by enhanced diffusion. This process has been described by Nedelcu [35] and De Rooij [46].

In the nanometer thick layers of the Mo/Si multilayers discussed in this thesis, the Si layers always exhibit an amorphous structure, which was shown by X-ray diffraction as well as transmission electron microscopy. The Mo layers have a polycrystalline structure with a critical minimum thickness for crystallization, which is approximately 2 nm for a Mo/Si multilayer [35, 55]. Below this thickness an amorphous-like structure is observed. The thickness dependence of the Mo crystallinity is illustrated in figure1.6, where the wide angle X-ray diffraction spectra (see section 2.3.2) of Mo layers with several thicknesses are shown. The spectra of the samples with 2.4 nm and 2.8 nm of Mo show a clear crystalline Mo bcc pattern, while for the 1.9 nm and 1.3 nm cases this pattern is not observed. Although the pattern is clearly not crystalline, a significant peak at 40° is observed, which indicates that at least some order is present. In previous work of Nedelcu et al. [35] it was suggested that this pattern could be identified as Mo_3Si, but an other interpretations is possible, namely the formation of nanoclusters.

The XRD spectrum below the critical thickness for bcc Mo growth could be interpreted as diffraction from nanoclusters in the Mo. Such nanoclusters were proposed for gold by Cervellino et al. [56] and figure 1.7 shows how diffraction from nanoclus-

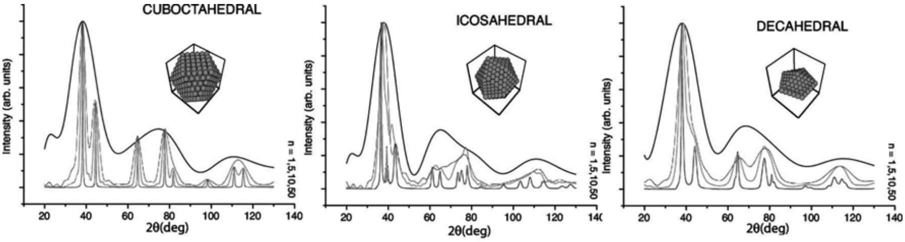

Figure 1.7: The calculated XRD spectra for gold nanoclusters by Cervellino et al. [56].

ters would account for the observed diffraction patterns in their work. The calculated XRD spectra for gold nanoclusters, for different nanocluster structures and sizes, are depicted. The size is determined by the number of shells (n) of atoms around a centre atom, in this case for n = 1, 5, 10 and 50. Naturally the peaks become sharper for larger particles.

The spectra in figure 1.7 are calculated for gold with an fcc structure, while the structure of Mo is bcc. These structures are both close-packed, which makes it very reasonable that the Mo structure might also show nanoclusters in thin films. The pattern for n=1 for all the structures look very similar to the pattern we observe for Mo layers thinner than 2 nm and it is therefore likely that nanoclusters are formed of 1 or 2 atomic shells in thin Mo layers. We will call these thin Mo layers ”quasi-amorphous” throughout this thesis.

For a Mo/Si multilayer design, to meet the Bragg condition, the Mo and Si layers need to be thinner to correct for the thickness of the diffusion barriers. For thick diffusion barriers the Mo thickness might drop below the critical thickness for crystallization. It is therefore important to investigate the differences in properties for crystalline and quasi-amorphous Mo. In reference [46] it was shown that the diffusion speed through the $MoSi_2$ interface is strongly influenced by the crystalline state of the interface. The influence of the Mo layer crystallinity in Mo/Si multilayer structures on the diffusion speed has so far not been investigated. In chapters 3 and 4, the diffusion speeds in multilayer structures with crystalline and quasi-amorphous Mo layers are studied. By reducing the interface on one type of interface (i.e. Mo-on-Si or Si-on-Mo) by a diffusion barrier we are able to study the diffusion properties across the other interface.

1.4 Outline

In many applications of multilayer optical coatings, requirements of the optics lifetime, especially at high power loads, are not a priori fulfilled. A change in the optical response due to thermally induced structural changes in the multilayer can be detrimental for the particular application. Often, thermal diffusion barriers are introduced between multilayer materials to reduce interdiffusion and thereby extend optics lifetime. In the optical design of a multilayer, introducing a diffusion barrier necessarily results in a change of the other layer thicknesses, in order to ensure proper wavelength matching (i.e. for normal incidence optics the total period should remain approximately constant).

Research on the different diffusion properties of crystalline and quasi-amorphous Mo in Mo/Si based multilayers is presented in chapter 3 and chapter 4. In chapter 3 we investigate this by reducing the diffusion on the Mo-on-Si interface by a Si_3N_4 diffusion barrier and so studying the diffusion through the Si-on-Mo interface. The research is performed using WAXRD and GIXR before and after annealing.

In chapter 4 we investigate the different diffusion properties of multilayers with crystalline and quasi-amorphous Mo layers on both interfaces using B_4C diffusion barriers. We find however that B_4C diffusion barriers partly decompose during annealing and form other compounds, especially when Mo is quasi-amorphous. From the results we show that B_4C decomposes and diffuses into Mo, which is studied by WAXRD, GIXR and XPS.

In chapter 5 we report on a new method for studying diffusion in multilayers. Using a hard X-ray diffractometer with a thermal dome, *in-situ* diffraction experiments are carried out during annealing, from which we can determine the period change of Mo/Si multilayers. We show that the multilayer period change can be connected to the increased thickness of $MoSi_2$ interfaces. From the temperature dependence, we extract the activation energy of the diffusion process.

In chapter 6 the *in-situ* annealing technique described in chapter 5 is used to study the improvement of B_4C barrier layers when they are deposited with ion assistance. We study multilayer structures with partially treated B_4C diffusion barriers in order to identify the mechanism behind this improvement.

In chapter 7 the damage mechanisms in MoN/SiN multilayers are studied. Thermal damage, by annealing, is compared to radiation induced damage from fs pulses in the free electron laser FLASH. We determine and explain the damage thresholds for both cases using XRD, TEM, AFM, XRD and Nomarski microscopy analysis.

Finally in chapter 8 the possible applications and the paths for further research are discussed.

Chapter 2

Experimental

2.1 Multilayer deposition setups

The multilayers investigated in this thesis are produced at various deposition facilities present in the nanolayer Surfaces and Interfaces (nSI) department at FOM Rijnhuizen. In these setups multilayers can be deposited by either electron beam (e-beam) deposition or magnetron sputtering in an Ultra High Vacuum (UHV) environment. The layer thicknesses can be monitored during the deposition process by *in-situ* X-ray monitoring or by quartz mass balances. Ion treatments are used to smoothen layers, increase the density, or form compounds. A schematic picture of a coating facility is shown in figure 2.1. A more detailed description of the components will be given in sections 2.1.1-2.1.3.

2.1.1 Multilayer layer growth methods

Various deposition techniques are capable of producing high quality nanometer thick films. In this thesis, two thin film deposition techniques were available in the experimental setups, namely DC pulsed magnetron sputtering and e-beam deposition. Magnetron deposition setups are regularly used for deposition of thin film multilayers, including Mo/Si based multilayers [29, 40, 55]. The magnetron coated multilayers in this thesis are deposited in a vacuum system with a base pressure which is better than 10^{-8} mbar. During deposition, krypton gas is fed into the magnetrons, which is then ionized by electrons which are emitted by a cathode. The target material is negatively biased, which causes the Kr^{+} ions to accelerate towards the target and sputter the target material. The magnetrons used in this study are at a larger distance ($\sim$40 cm) than is traditionally used in magnetron sputtering, in order to reduce the energy of the sputtered atoms by multiple collisions with the gas in the vacuum chamber. The reduced energy of the arriving atoms reduces the chance on damage

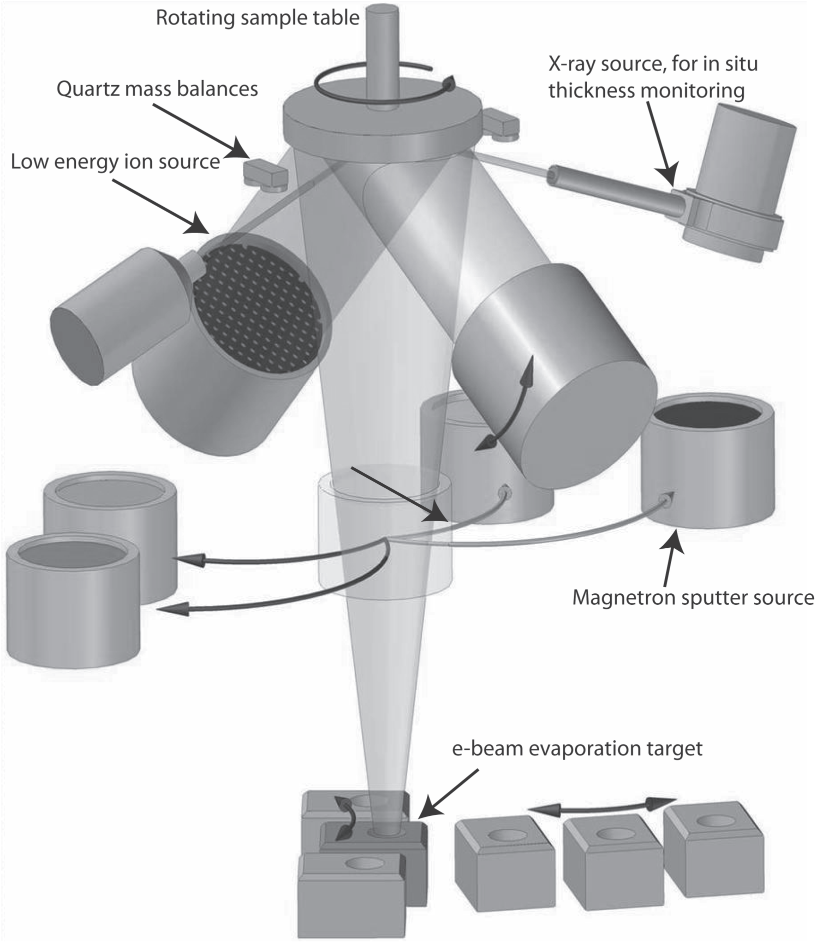

Figure 2.1: Schematic representation of a multilayer coating facility.

of the surface during deposition.

Most of the multilayers used in this thesis are grown by electron beam deposition. During layer deposition an electron beam evaporates a solid material in a cooled crucible. The advantage of this method is that the particles arriving at the substrate have low adatom energy ($<$1 eV). This low energy reduces sub-surface atom implantation and thereby also reduces intermixing with the previous layer or substrate. A disadvantage of this low energy is that the layers may develop roughness and have reduced density. In such cases, low energy ion bombardment during and/or after layer growth may provide a way to increase the density and reduce the roughness.

2.1.2 Ion treatment

Ion beam bombardment is a well established technique for modification of a surface. For ultrathin films, ion bombardment does not only interact with the surface, but depending on the energy of the ions, a significant part of the ion energy is deposited just below the surface, modifying thin film ”bulk” properties such as density, composition, etc. Ion treatment of a thin film can be done with inert or reactive atoms. In the first case, usually ions of noble gases are used to transfer energy to the surface, resulting in sputtering of surface atoms (smoothening of surface roughness) and generally increasing the density of the layer. If a reactive gas is used, different compounds can be formed due to reactions with the sputter gas.

In the setups used to produce the multilayers studied in this thesis, a Kaufman-type ion gun is present to supply a beam of ions. To avoid surface damage in the thin films of a multilayer, the energies which are used are relatively low, between 60 and 150 eV. In the multilayers discussed in this thesis, all the Si layers are treated with Kr^+ ions to reduce roughness building up during the deposition of multilayers. After deposition of each Si layer, approximately 5 Å of the deposited layer is removed in this way. The polycrystalline Mo layers are not treated with ions, since it has been shown that the roughness increases during ion bombardment due to preferential sputtering along specific crystal planes.

In chapter 6, low energy Kr^+ ion bombardment was applied during the growth of a B_4C layer. The B_4C layer was used to act as a barrier layer against diffusion, and we show that ion treatment of the B_4C layers improves their quality as barrier layers in Mo/Si multilayers. The improved barrier quality will be shown to be linked to the increased density of the layer, which reduces diffusion through the B_4C layers.

Another application of surface ion treatment used in this thesis is the reactive ion bombardment of Si and Mo surfaces to form specific compounds. The MoN/SiN multilayers that are reported on in chapter 7 were prepared with this method. In this case, we bombard the sample with nitrogen ions during the deposition of Mo and/or Si atoms, resulting in the formation of silicon nitride and molybdenum nitride respectively. The stoichiometry of the formed compound can be controlled by controlling the balance between the deposition flux of Mo or Si and the ion flux from the Kaufman source. Surface treatment by nitrogen ions can also be used after the deposition of a layer has been completed, to form a thin Si_3N_4 layer at the surface that can act as a diffusion barrier to prevent thermally induced molybdenum silicide formation, as will be shown in chapter 3.

2.1.3 Layer thickness control

In thin film research it is obviously very important to monitor and control the film thickness, because many film properties strongly depend on film thickness (e.g. film density, strain, conductivity, optical parameters, etc). In the case of multilayer optics, thickness control is particularly important, as discussed in section 1.2.1.

The thickness of a layer deposited by magnetrons can be determined by the deposition time. The deposition flux of magnetrons is very stable and reproducible. Once an absolute calibration of the deposited thickness versus the deposition time has been established, controlling deposition time is the easiest way to accurately controlling the layer thicknesses.

To monitor the layer thickness during growth, a ring around the sample holder in the coater holds several quartz mass balances which are mounted next to the sample holder. These are crystals that vibrate at a resonance frequency, which is dependent on their mass. If extra mass is added by depositing a thin film, the frequency changes. From this frequency change the mass deposited on the quartz mass balance can be determined. If the density of the deposited material is known, the quartz mass balances can give an accurate measure of the thickness of the deposited layers. The accuracy of this method is limited to approximately 0.3 Å, due to variations in temperature or pressure (which can influence the vibrations) and uncertainty in the density. In addition, the deposited thickness is measured off-centre in the deposition plume, resulting in uncertainties in deposited thickness on the sample holder due to gradients and instabilities in the deposition plume.

The third method that can be used for layer thickness control uses an *in-situ* X-ray monitoring system. In this setup, soft X-ray (λ = 4.48 nm) reflectivity at a constant grazing incidence angle is measured during layer growth, exhibiting amplitude oscillations connected to the interference between reflection from the surface of the growing layer and all reflection from all buried interfaces. This method is very useful for *in-situ* monitoring of thin film growth, yielding information on surface roughness as well as providing an accurate measure of the layer thickness. In order for this to work, optical contrast between the thin layers is required.

2.2 Sample treatments for damage studies

2.2.1 Annealing

The main focus of this thesis is understanding the physical and chemical processes that occur in Mo/Si based multilayers at enhanced temperatures. To study these processes, two methods were used: sequential thermal annealing in a vacuum oven and *in-situ* annealing inside a hard X-ray diffractometer. The sequential annealing experiments are performed to investigate specifically the temperature dependency

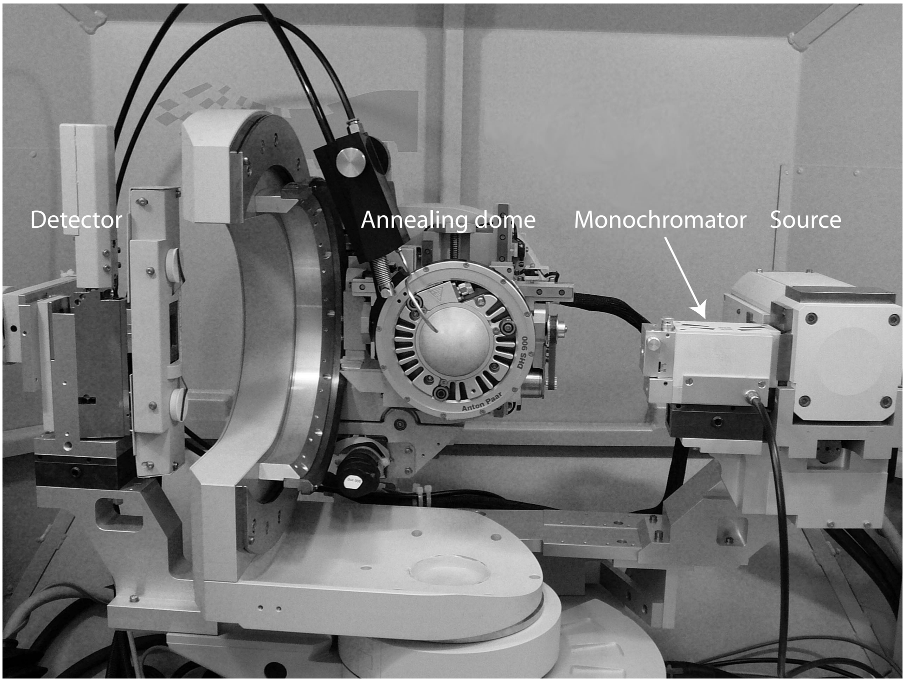

Figure 2.2: Picture of the *in-situ* annealing setup inside the diffractometer. The heating stage is situated under the dome shown in the picture.

of the diffusion processes. In the *in-situ* setup, the focus is on understanding the time dependency of the processes.

The sequential thermal annealing experiments are performed in a vacuum environment of 10^{-5} mbar to prevent contamination and oxidation of the sample. The temperature range of the setup is 250-1200°C with temperature fluctuations during annealing contained within ± 5°C. In typical experiments the temperature was increased in steps of 25°C and annealed for 48 h at each temperature step. The 48 h annealing time is chosen because most of the structural changes occur in the first 20-30 hours with only minor changes afterwards. This is illustrated in [29] and in chapters 5 and 6. Before annealing and after each annealing step the samples were analyzed using grazing incidence X-ray reflection (GIXR), wide angle X-ray diffraction (WAXRD) and/or X-ray photoelectron spectroscopy (XPS). The experimental details on these analysis techniques are given in sections 2.3.3, 2.3.2 and 2.4.

The time (and temperature) dependent annealing experiments were performed inside a hard X-ray diffractometer (Cukα, λ = 0.15406 nm) which is shown in figure 2.2. The temperature stage is capable of reaching temperatures between 25°C and 900°C. The sample is heated via a hotplate which is located under the annealing dome (see figure 2.2). The temperature control, stability and reproducibility of the heating plate is within 0.5°C which makes the temperature control much better as in the sequential annealing setup. However, due to variations in thermal conductivity, the temperature on top of the sample can deviate. At relatively low temperatures however ($<$300°C) this effect is limited to less than 2°C and therefore it can be neglected for all research described in this thesis. The sample stage can rotate in all directions, which makes it suitable for all diffraction studies during annealing. A detailed description of this setup is provided in reference [57].

For the *in-situ* annealing experiments, a vacuum environment cannot be applied during annealing. The dome (which is made from the X-ray transparent material PEEK) does allow for performing experiments in a nitrogen environment by applying a constant flow of 1 l/min through the dome to prevent most of the contamination during annealing. This will also strongly reduce, but never completely prevent oxidation, which means that the top few nanometers of the multilayer may still oxidize. XPS analysis of the samples after annealing has shown that below 400°C these effects are limited to the first layer, above this temperature one full bilayer is affected. Since the results presented in this thesis concern the internal structure of the multilayer and the 0.15406 nm radiation penetrates through all layers, the effect of surface oxidation can be ignored in the analysis. The measurements done during the annealing experiment will be elaborately described in section 2.3.4.

2.2.2 Free electron lasers

In chapter 7 ultra-short (10 fs) pulses of 13.5 nm radiation from a free electron laser (FEL) were used to study the radiation damage of a MoN/SiN multilayer. An FEL uses electrons that are accelerated by a linear accelerator to close to the speed of light (1 GeV). These electrons travel through an undulator, which is a structure consisting of a series of alternating magnets (see figure 2.3). Due to the Lorentz forces the electrons follow an oscillating path and emit bremsstrahlung along their way. Of key importance to FELS in the X-ray regime is Self-Amplified Spontaneous Emission (SASE). In the first part of the undulator the electrons emit X-ray photons spontaneously. These photons travel at the speed of light and overtake the electrons. These photons form an electro magnetic field, which interacts with the electrons. Electrons that are in phase with this field get decelerated, while electrons that are not in phase are accelerated. This will eventually create microbunches of electrons that are overtaken by exactly one photon wavelength each period of the undulator. When this happens all the electrons of the microbunches radiate in phase, producing an extremely short, coherent and intense pulse of X-rays.

The FEL used in this study is the Free electron LASer in Hamburg (FLASH) in Germany. This machine can produce laser radiation in a wavelength range of 4.5 to 47 nm, with a spectral width of 0.5-1%. The pulse duration is between 10 and 50 fs and the maximal pulse energy is 10-50 μJ.

In the study discussed in chapter 7, FLASH is used in different configurations. The sample can be translated in and out of the focus of the beam, creating power densities between 1×10^{11} and 5×10^{13} W/cm^2. The reflectance can thus be

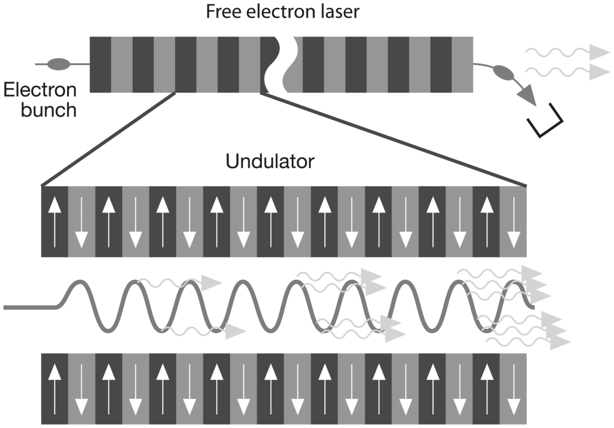

Figure 2.3: Principle of a FEL, the electrons are accelerated to relativistic energies and injected into the undulator. To simplify the picture of the undulator a wavelike electron trajectory is drawn in the plane of the drawing in the undulator while in reality it is perpendicular to this plane. The electrons emit light due to the SASE principle (see text).

measured at 'high intensity mode' (in the focus) and 'low intensity mode' (out of the focus) and linked to the multilayer damage that is observed after the pulse. To determine the damage threshold, the sample is placed in the focus of the beam, which is then attenuated by a gas attenuator to reduce the pulse power to values around the expected damage threshold. Each subsequent pulse was in all cases directed at an unperturbed spot of the multilayer. The illuminated spots were investigated after exposure, with optical microscopy with differential interference contrast, AFM, and STEM.

2.3 Analysis methods

2.3.1 Hard X-ray diffraction

One of the most important measurement techniques used in this thesis is hard X-ray diffraction. These measurements are performed on a Panalytical X'pert MRD diffraction machine. The radiation from the Cu X-ray tube, in line focus, is monochromated to only the Cukα_1 line using a 4-bounce Ge(220) asymmetric monochromator. The monocromator has an internal divergence of 18" and the wavelength spread is less than the width of the CuKα_1 line, the width of the beam is approximately 0.04°. At the detector side two slits are mounted: a programmable receiving slit and a programmable anti scatter slit. On top of that an automatic attenuator is mounted at the site of the detector to avoid damage to the detector during direct illumination. A picture of the setup is provided in figure 2.2. Two different measurement geometries are used in this thesis, and will be discussed in the next two sections.

2.3.2 Wide angle X-ray diffraction

The crystalline structure of Mo/Si multilayers is very important for the physical properties of the multilayer, which is discussed in detail in section 1.3.5. The crystalline structure of the multilayers was investigated using Wide Angle X-Ray diffraction (WAXRD). The measurement geometry is shown in figure 2.4 in the top graph.

In a standard Mo/Si multilayer, Si is amorphous, while Mo is polycrystalline. The diffracted intensity from a polycrystalline structure is much lower than from a single crystal. In order to improve the signal-to-noise ratio, a fixed, glancing source angle of 1° is used to illuminate a large area, which increases the diffracting volume. To increase the intensity even more, the detector slit size is set to an acceptance angle of 0.4° to get the maximum intensity. The 1° angle of incidence gives a peak broadening of about 1°. A 2θ detector scan, usually in the range of 20-150°, is performed to record a spectrum. Since the multilayers investigated in this thesis are generally deposited onto crystalline Si substrates, the samples are rotated by 20° in plane to suppress the signal from the (422) and (311) diffraction peaks from Si. From the pattern of the XRD spectra we can determine the crystalline state, including the crystallite size and the lattice strains.

Lattice spacing's and lattice strains can be determined from the diffraction peak positions using Bragg's law (equation 1.1). The crystallite size L can be determined using the Scherrer equation [58, 59]:

$$L = \frac{K\lambda}{B(2\theta)\cos\theta}, \tag{2.1}$$

where L is the average size of the crystallites, K is the Scherrer constant and $B(2\theta)$ is the full width half maximum (FWHM) of the diffraction peak at position 2θ. The Scherrer constant is 0.94 for lattices with cubic symmetry (which is the case for the Mo crystal structure). The crystal size can be dependent on the orientation of the crystallites in the layer. This is determined by the angle ψ, which is the angle between the surface normal of the substrate and the normal vector of the diffraction planes. For an accurate determination of L, the instrumental broadening should be small compared to B. The peaks were typically 3-4° wide, while the instrumental broadening is about 1°. This experimental broadening is thus quite large, which will give an underestimation of the peak width in measurements. Changes in the crystallite size during annealing can, however, be detected.

To analyze the stress in the crystallites, the measured lattice distances (which can be determined using Bragg's law) are compared to the unstressed/strained values of the lattice. From this the lattice strain can be calculated. This strain can be plotted against $\sin^2\psi$ for all the diffraction peaks in the spectrum. If there is only biaxial stress, this should give a straight line; this dependence can then be correlated to the stress in the lattice through a stress tensor. A detailed description can be found in reference [60].

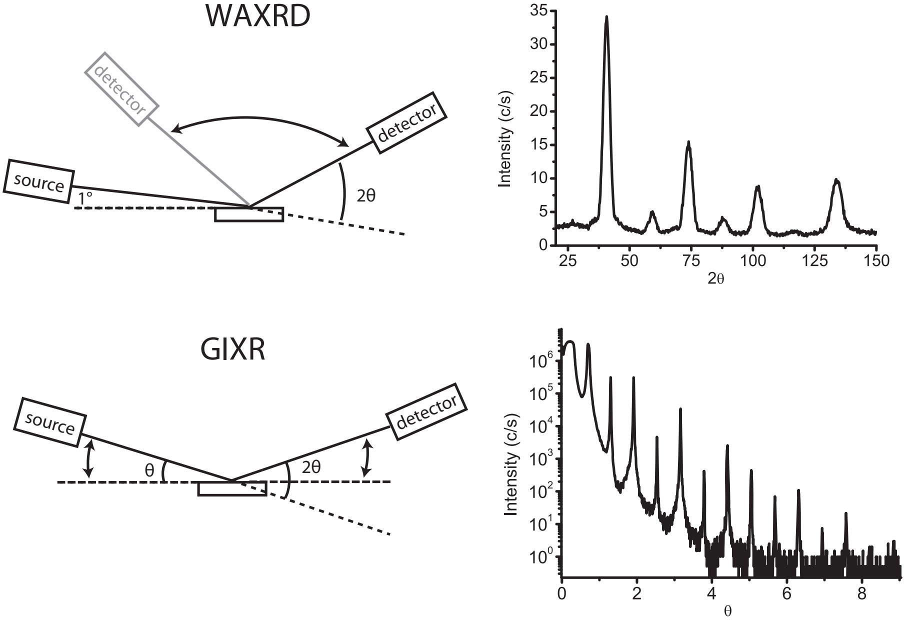

Figure 2.4: Wide angle X-ray diffraction (WAXRD) and grazing incidence X-ray reflection (GIXR) measurement geometries, including corresponding example spectra for a Mo/Si multilayer.

2.3.3 Grazing incidence X-ray reflection

The period of the multilayers considered in this thesis is typically one order of magnitude larger than the distance of the lattice planes in the crystallites. As a result, Bragg reflections from the multilayer lattice will be observed at much smaller angles. To accurately describe the positions of the Bragg reflections at grazing angles of incidence, equation 1.1 is corrected for refraction in the multilayer and can be written as [9]:

$$m\lambda = 2d\sin\theta\sqrt{1-\frac{2\overline{\delta}}{\sin^2\theta}} \tag{2.2}$$

where $\overline{\delta}$ represents the weighted average over the δ values of the materials in the penetration depth, and δ is equal to 1-n. This equation can be rewritten as:

$$\sin^2\theta = \frac{m^2\lambda^2}{4d^2} + 2\overline{\delta}. \tag{2.3}$$

The grazing incidence X-ray reflectivity (GIXR) measurements are performed in a Bragg-Brentano geometry, in the range of 0-10°, the geometry and an example of a GIXR spectrum are shown in figure 2.4. The peak positions of this spectrum can be analyzed using equation 2.3 and from this analysis both the period of the multilayer and the average $\overline{\delta}$ can be determined to provide information on the multilayer. More information about the layered structure, including surface/interface roughness and compound formation at the interfaces can be obtained from model simulation of the complete spectrum using a software package like IMD [61].

2.3.4 *In-situ* grazing incidence X-ray reflection during annealing

To investigate the structural changes occurring during thermal annealing in multilayers *in real time* during thermal annealing, *in-situ*F annealing experiments are performed in the hard X-ray diffraction setup shown in figure 2.2. Prior to the thermal annealing, the sample surface is aligned with respect to the X-ray beam. After that, a reference GIXR spectrum is recorded and subsequently the temperature of the sample is raised to the desired value. Due to thermal expansion of the sample stage and the sample, the sample may need re-alignment in the early stages of annealing, especially with respect to the height of the stage. There might also be a slight misalignment in θ, but this can be corrected for by the fitting procedure described below.

To avoid changes in the multilayer structure during recording of a full GIXR spectrum, only a partial spectrum is recorded during annealing to speed up data collection. The data is then interpreted by comparing the angular positions of specific low and high order diffraction peaks to those obtained for the reference spectrum. The change in multilayer period is determined using a simplification of equation 2.3, where we assume that $\overline{\delta}$ does not change and can therefore be neglected and $\sin\theta \approx \theta$, for small values of θ, yielding

$$(\Delta\theta_2 - \Delta\theta_1) = \Delta m \lambda \left(\frac{1}{2d_0} - \frac{1}{2d} \right), \tag{2.4}$$

where Δm is the Bragg order difference between the low and high order peaks being recorded, d_0 is the period of the multilayer before annealing, d is the period during annealing and $\Delta\theta_1$ and $\Delta\theta_2$ are the peak shifts of the low order and high order diffraction peaks with respect to their reference scan positions.

By specifically considering *relative* shifts in Bragg peak positions this method is independent on a small misalignment of the sample in θ, because this misalignment is equal for both peaks. Furthermore, by comparing the same Bragg orders before and after annealing, this method is not sensitive to errors introduced by differences in peak shapes of the Bragg peaks that complicate the determination of a multilayer period using a single spectrum.

For an accurate determination of the period change, the measured peaks should have a Δm which is as large as possible. The second Bragg order peak is selected, because the first Bragg order peak has experimentally shown to give a larger error in determining the period change, as is discussed by Voorma [62]. One or more other peaks (depending on the specific demands of the experiment) are selected, which retain their shape during annealing and have sufficiently high intensity to accurately determine the peak position.

2.4 XPS

X-ray photoelectron spectroscopy (XPS) is a technique to determine the elemental composition and chemical states in a surface layer. Soft X-rays (photon energy 1486.6 eV) are used to remove a core electron from an atom in the surface, which can then escape from the surface to a detector which detects the energy of the electron. From the difference between the energy of the incoming photon and the outgoing electron the binding energy of the emitted electron can be determined, which is element specific. The chemical bounds of the atom can influence the element specific binding energy slightly (up to 1 eV) which can give information on compound formation. A typical electron mean free path due to recombination is a few nm, yielding a maximum information depth of 5-10 nm, depending on the emitted core electron energies.

Non-destructive depth information can be obtained within the total sample depth by angular resolved XPS. At grazing angles, the emitted electrons will have originated close to the surface, while at larger angles, the electrons can originate from deeper in the sample. The angular dependence of emitted electrons therefore provides an in-depth concentration profile within the information depth. In this thesis we are interested in the in-depth structure of the multilayer over several periods of typically 7 nm. The top few layers of this structure are often contaminated with oxygen and/or carbon. Angular resolved XPS is therefore not very suited for studying the internal structure of the multilayer.

Another way to obtain information about the in-depth atomic concentration in a multilayer is by ion beam sputtering, combined with XPS measurements. In this

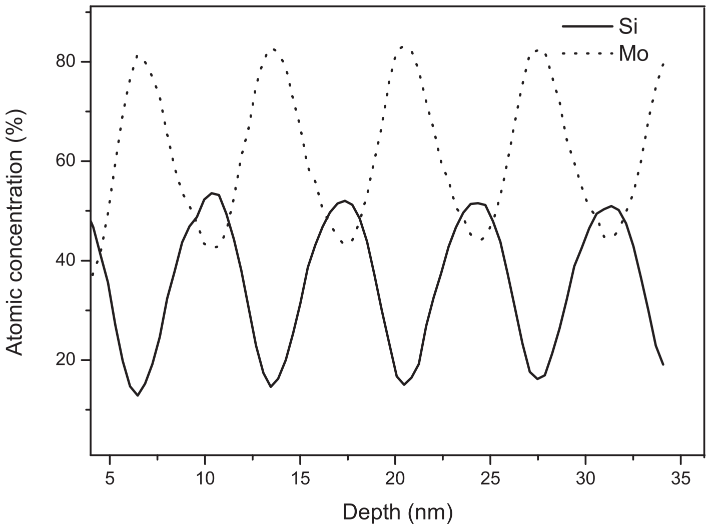

Figure 2.5: Example of a XPS dept profile, of a standard Mo/Si multilayer.

thesis, 0.5 eV Ar^+ ions are used to erode a thin layer from the surface, and subsequently an XPS measurement is performed. Alternatively eroding and measuring provides in depth information on the composition of the multilayer. With this technique we have to keep in mind that the erosion process does intermix the layers and the sampling depth is larger than the typical layer thickness. Therefore it is expected that we do not observe a sharp atomic concentration transition between the materials, but a more gradual transition. An example of an XPS depth profile of a Mo/Si multilayer is shown in figure 2.5. As can be seen the concentrations of both Mo and Si never go to 100%, which is caused by the sampling depth and intermixing by sputtering. An other deviation from the real concentration can occur due to preferential sputtering of light atoms. Although, for the reasons mentioned here, we cannot determine the *absolute* atomic concentration profile from the XPS data, in our diffusion studies XPS provides valuable information on the *relative* changes in the atomic concentration profiles before and after annealing.

Chapter 3

The effect of Mo crystallinity on diffusion through the Si-on-Mo interface

Abstract

Thermally induced diffusion through the Si-on-Mo interface of multilayers with either quasi-amorphous or polycrystalline Mo layers has been investigated using grazing incidence and wide angle X-ray reflectometry. Diffusion through the Mo-on-Si interface was reduced by applying a diffusion barrier, allowing us to probe the diffusion at the opposite, Si-on-Mo interface. We found that diffusion through this interface is much slower for polycrystalline Mo than for quasi-amorphous Mo layers. The reason for this difference might be the larger defect concentration in quasi-amorphous Mo as compared to crystalline Mo.

3.1 Introduction

Extreme ultraviolet lithography (EUVL), designed to operate at a wavelength of approximately 13.5 nm, is a serious candidate for next generation projection lithography systems to be applied in the semiconductor industry [63]. The optics in EUVL systems contain reflective multilayer coatings basically consisting of alternating Mo and Si layers. The theoretical multilayer reflection for 13.5 nm is 74%: in practice the reflectivity is limited to below 70% due to interface roughness as well as interaction of Mo and Si at the interfaces, where a molybdenum silicide is formed [64].

This molybdenum silicide formation is known to further accelerate at the enhanced temperatures that multilayers are exposed to under high intensity EUV illumination, leading to further reduction of the reflectivity as well as a change in the period of the multilayer. This causes the wavelength where maximum reflectivity occurs to deviate from the target value of 13.5 nm. Improvement of Mo/Si coatings in this respect requires fundamental knowledge on the structure of the deposited layers as well as a detailed understanding of the processes that take place at the interfaces during deposition. It is already known from literature that amorphous Si layers are formed during deposition, whereas the Mo layers crystallize above a critical thickness of about 2 nm [30, 31]. For crystalline Mo, it is also known that the formed Mo-on-Si interface is about 1 nm thick, while the formed Si-on-Mo interface is about 0.5 nm thick. When Mo is quasi-amorphous however, both interfaces are about 1 nm thick [28, 29, 55].

Knowledge on the exact nature of interface formation is critical in understanding and controlling the processes that occur at the enhanced temperatures to which multilayer coatings will be exposed during EUV illumination. Previous studies on the thermal behaviour of Mo/Si multilayers showed that when Mo is crystalline the growth of the interface due to diffusion at the interfaces is much faster through the thick Mo-on-Si interface than through the thin Si-on-Mo interface [29]. As high temperature applications of multilayers might require thick diffusion barriers, the Mo layer thickness generally needs to be reduced to maximise the reflectivity and this may bring the Mo layer thickness below the critical thickness value for crystallization. In this chapter we report on a study of the diffusion speed through the Si-on-Mo interface in multilayers with quasi-amorphous Mo layers. We do this by applying a Si_3N_4 diffusion barrier which has shown to reduce diffusion at the Mo-on-Si interface [31] and is used as an example barrier in this study. The single sided applied diffusion barrier allows us to uniquely isolate the diffusion phenomena to one type of interface. This is required in view of the asymmetry between the two types of interfaces described above.

3.2 Experimental

All samples were prepared by electron-beam evaporation, using a coater with a controlled UHV environment (base pressure $< 2 \cdot 10^{-8}$ mbar). The thicknesses of the layers are controlled by an *in-situ* X-ray reflectometer that monitors X-ray reflection of the sample during multilayer growth. In addition, quartz mass balances are used to monitor layer thicknesses during the deposition. The sample holder rotates at 1 Hz to ensure a homogeneous coating in the azimuth direction. A detailed description of the setup can be found in [65]. The multilayers were deposited on 25 x 25 mm^2 super-polished silicon substrates.

Multilayers with different Mo thicknesses are made in order to obtain both crystalline and quasi-amorphous Mo layers. A deposition flux shaping mask was used during the deposition of Mo in order to create a linear Mo thickness gradient from 3.6-1.6 nm on the samples mounted on the holder. To reduce the interface roughness during deposition, every Si layer was smoothened using a Kr^+ ion beam. After polishing, the Si thickness was 4.5 nm. The Si_3N_4 interface on Si was created by ion treatment with nitrogen directly after the Kr^+ surface smoothening. More details on the process of nitride formation and the actually formed stoichiometries will be presented elsewhere.

To characterise the diffusion speeds through the Mo-on-Si interface, all samples were sequentially annealed in a vacuum environment ($< 10^{-5}$ mbar) for 48 h at temperatures between 300°C and 375°C with steps of 25°C. This method is applied to accelerate the diffusion phenomena, since the diffusion scales exponentially with temperature (Arrhenius equation, see equation 5.5). It is already known [31] that annealing either sequentially or directly to a final temperature does not result in a noticeable difference in multilayer structure after annealing. After each 25°C step, the multilayer structure is analyzed using grazing incidence X-ray reflectivity (GIXR) on a Philips X'pert Cu-K_α diffractometer using a wavelength of 0.15406 nm. The crystalline structure of the layers is investigated using wide angle X-ray diffraction (WAXRD) on the X'pert diffractometer. During WAXRD measurements an incident angle of 1° is used to maximise diffracted intensity. The sample is rotated 20° in the sample plane in order to suppress diffraction from the crystalline Si substrate [30].

3.3 Results and discussion

Figure 3.1 shows WAXRD spectra of Mo/Si multilayers in which a Si_3N_4 diffusion barrier is applied on the Mo-on-Si interface to reduce diffusion through this interface. For Mo thicknesses of 2.2, 2.8 and 3.4 nm, the spectra clearly indicate the formation of bcc polycrystalline Mo layers. For a Mo thickness of 1.4 nm, the diffraction spectrum is identified as quasi-amorphous (see section 1.3.5).

Figure 3.2 shows the change in multilayer period as a function of the annealing temperature for multilayers with a single-sided Si_3N_4 diffusion barrier and a multilayer without barriers as a reference. The diffusion through the Mo-on-Si interface is stopped, or at least hampered by the barrier. Therefore the change in multilayer period that is caused by diffusion is expected to be much smaller than that for a multilayer without barriers, because this interface has shown to grow slower than the Si-on-Mo interface in high resolution transmission electron microscopy (HRTEM) studies [29]. For crystalline Mo, the period change is indeed reduced compared to a multilayer without diffusion barriers, as reported in [31]. In the case of quasi-

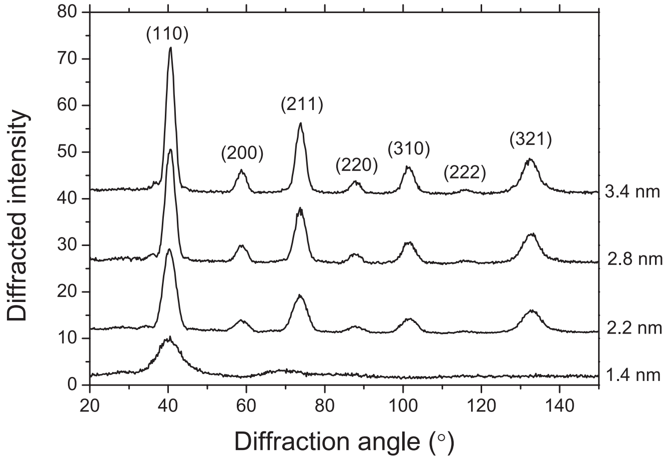

Figure 3.1: WAXRD spectra of as-deposited Mo/Si multilayers with Si_3N_4 diffusion barriers at the Mo-on-Si interfaces. The spectra for Mo = 2.2, 2.8 and 3.4 nm have been shifted for clarity. The top three spectra have been assigned to be crystalline Mo, the Miller indexes of the diffraction peaks are indicated above the upper spectrum. The spectrum for Mo = 1.4 nm is assigned to be quasi-amorphous.

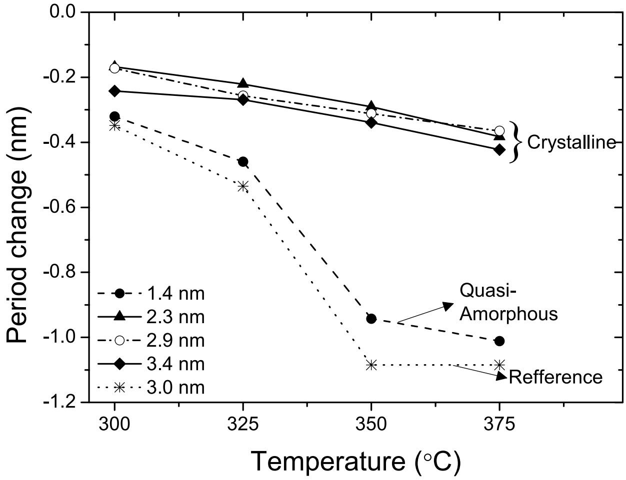

Figure 3.2: Period change as a function of annealing temperature for multilayers with Si_3N_4 diffusion barriers at the Mo-on-Si interfaces. The samples in which the Mo is crystalline show less change than those in which Mo is quasi-amorphous, suggesting slower diffusion through the interfaces. The period change measured for a multilayer without any diffusion barrier is included as a reference.

amorphous Mo however, diffusion is equally fast for a multilayer without barriers. Clearly, diffusion through the Si-on-Mo interface is much faster when the Mo layer is quasi-amorphous.

This shows that indeed the crystallinity of the Mo layer has a large influence on the diffusion behaviour through the interfaces of a Mo/Si multilayer. The Si-on-Mo interface is thicker, and is a less effective diffusion barrier during thermal annealing when Mo is quasi-amorphous, than when Mo is crystalline.

A possible explanation for the observed differences in diffusion speed is the defect concentration in the Mo layer. It is a well known phenomenon that the diffusion speed through crystalline material is dependent on the amount of defects [66], since atoms are known to hop from one defect to the other. This makes diffusion through a polycrystalline material faster compared to diffusion through a fully crystalline lattice, because it has more defects around the grain boundaries. The quasi-amorphous state of materials has even more defects than a polycrystalline state and therefore it would be expected that in the quasi-amorphous state diffusion is faster.

3.4 Conclusions

We investigated the diffusion through the Si-on-Mo interface in multilayers with quasi-amorphous and polycrystalline Mo, depending on the initial thickness of the Mo layers in the multilayer samples. To study this phenomenon at a single type of interface, possible diffusion through the opposite, in this case the Mo-on-Si interface was reduced by applying a Si_3N_4 diffusion barrier. The diffusion in the multilayers was investigated by thermal annealing followed by analysis using GIXR. We show a clear difference in diffusion speed through the Si-on-Mo interface for crystalline and quasi-amorphous Mo layers. When Mo is crystalline the diffusion through the Si-on-Mo interface is slow, but when the Mo is quasi-amorphous, the diffusion is considerably faster. The explanation posed for this difference is the higher defect concentration in quasi-amorphous Mo as compared to crystalline Mo.

Chapter 4

Thermally induced decomposition of B_4C barrier layers in Mo/Si multilayer structures

Abstract

We investigate the influence of the Mo crystalline state (quasi-amorphous or crystalline) on the thermal stability of Mo/Si thin film multilayers with B_4C diffusion barrier layers at either of the two interfaces. We find that multilayers containing amorphous Mo layers are more stable than those containing crystalline layers. This observation is in contrast to the case where Si_3N_4 diffusion barriers are used, in chapter 3. Using X-ray diffraction, X-ray reflection and X-ray photo-electron spectroscopy we show that this difference can be attributed to the dissociation of B_4C followed by diffusion of B in the Mo. Due to the favourable thermodynamic properties of Mo_xB_y compounds, the boron atoms react with the Mo layer, forming a Mo_xB_y layer that effectively improves the multilayer thermal resistance.

4.1 Introduction

Multilayers with a period of around 7 nm are useful for application as reflective optics for future Extreme Ultraviolet (EUV) photolithography equipment. Mo/Si based multilayers are the most promising mirror system to provide high reflectivities [13]. The EUV light source power in such equipment has to increase to over 100 W in the coming years. This will put a substantial thermal load on the optical elements, and multilayer coatings. These coatings are known to deteriorate due to diffusion at the interfaces when subjected to high temperatures, which shortens their lifetime. Understanding the thermal diffusion effects in multilayers is therefore an important research topic [31, 44, 67–69]. To improve the stability of these coatings, diffusion barriers are generally applied in between the Mo and Si layers.

The presence of B_4C barriers has been demonstrated to lower diffusion rates, thereby effectively lengthening the lifetime of multilayer optics [47, 70]. To obtain the required lifetime for high temperature applications thick B_4C barrier layers are considered. To compensate the multilayer period for this, the Mo and Si layers will need to be thinner. Mo crystallizes at a thickness of approximately 2 nm into a polycrystalline bcc lattice [30, 35].

In chapter 3 we investigated multilayers with a Si_3N_4 diffusion barrier on the Mo-on-Si interface. The results showed that the diffusion through the Si-on-Mo interface (which did not have a diffusion barrier) was much faster if the Mo layer was quasi-amorphous as compared to when Mo was crystalline. So far, the dependence of the diffusion rate on the crystallinity of Mo has not been explored in the case of B_4C barrier layers. Therefore, we study the thermal stability and chemical interactions of both crystalline and quasi-amorphous Mo layers combined with B_4C barriers. We observe and explain a surprising difference with the Si_3N_4 results when B_4C is used as a barrier layer.

4.2 Experimental

Two types of multilayers were prepared, one set with a B_4C barrier on the Mo-on-Si interface and one with a B_4C barrier on the Si-on-Mo interface. For reference, multilayers with only Mo and Si were studied as well. All samples were prepared by electron-beam evaporation, using a deposition setup with a controlled UHV environment (base pressure $< 2 \cdot 10^{-8}$ mbar). The thickness of the layers was controlled by an *in-situ* X-ray reflectometer that monitors X-ray reflection of the sample during multilayer growth. In addition, quartz mass balances were used to monitor layer thicknesses during the deposition. The sample holder rotates at 1 Hz to ensure a homogeneous coating in the azimuthal direction of the sample holder. A detailed description of the setup can be found in reference [65].

The multilayers were deposited on 25 x 25 mm^2 super-polished Si substrates. A deposition flux shaping mask was used during the deposition of Mo in order to create a linear gradient in the Mo thickness between 1 and 3 nm over the samples. The specific Mo thicknesses for the 9 samples are given in Table 4.1. These values

Table 4.1: The layer thicknesses of the individual Mo layers (Q_{Mo}) calculated from the shape of the mask and the thicknesses measured by quartz mass balances. Also indicated is the state of Mo (crystalline (C) or quasi-amorphous (QA)), as observed from WAXRD experiments.

Sample		Q_{Mo} (nm)	State Mo
1	B_4C on Mo	2.8±0.1	C
2		1.9±0.1	QA
3		1.3±0.1	QA
4	B_4C on Si	2.7±0.1	C
5		1.8±0.1	QA
6		1.2±0.1	QA
7	No B_4C	2.8±0.1	C
8		1.9±0.1	QA
9		1.3±0.1	QA

are determined from the thickness by unobscured quartz mass balances, by scaling to the amount of obscuration of the samples by the mask. The B_4C thicknesses were selected to be 0.8 nm for all studied multilayers, which is a typical value for several applications. To reduce the interface roughness during deposition, every Si layer was smoothened using Kr^+ ions. The Si layer thickness is 4.5 ± 0.1 nm for all samples.

The thermal stability of these multilayers was investigated by sequential annealing, in a vacuum environment ($< 10^{-5}$ mbar) for 48h at temperatures between 300°C and 375°C. After each 25°C step, the multilayer structure was analyzed using grazing incidence X-ray reflectivity (GIXR) on a Philips X'pert Cu-K_α diffractometer ($\lambda = 0.15406$ nm).

The crystalline structure of the layers was investigated using wide angle X-ray diffraction (WAXRD) on the X'pert diffractometer. During WAXRD measurements a fixed incident angle of 1° was used to maximise the illuminated area. The sample was rotated 20° in the sample plane in order to suppress the (422) and (311) diffraction peaks from the crystalline Si substrate. A detailed description of WAXRD measurements in Mo/Si multilayers is given in reference [30].

To determine the multilayer composition before and after annealing, XPS depth profiles were measured. The atomic composition of the top 10 nm of the multilayer was determined using monochromatic Al-K_α radiation. To get in-depth information, the surface was then etched using 0.5kV Ar^+ ions at a rate of approximately 1 nm per minute. An in-depth profile of elements was obtained by alternately etching and performing an XPS measurement.

4.3 Results

4.3.1 Sequential annealing

All multilayers were annealed sequentially in 25°C steps, in order to determine the thermal stability. After each 25°C step, the period was determined by fitting the GIXR peak positions using Bragg's law. After annealing, a period reduction is observed for all multilayer systems considered here. This period change has been linked to the formation of $MoSi_2$ at the interfaces between the Mo and Si layers [35, 68, 71, 72] resulting in a densification at the interfaces and subsequent period reduction.

The period changes for the different multilayers for temperatures between 300 and 375°C are shown in figure 4.1a. The diffusion at either the Mo-on-Si or the Si-on-Mo interface is significantly reduced by a B_4C diffusion barrier, which allows us to follow the diffusion on the opposite interface, that does not have a diffusion barrier layer. In the graph we compare multilayers with B_4C on top of the Si layer (dashed lines) with B_4C on top of the Mo layer (solid lines). For multilayers with Mo thicknesses of 1.3 and 1.8 nm the location of the B_4C barrier layer does not influence the period change. In contrast, in the case of a Mo thickness of 2.8 nm the multilayer with B_4C on top of Mo shows clearly more period change. WAXRD measurements (which will be discussed in more detail below) show that the difference between the 1.3 nm or 1.8 nm cases and the case of 2.8 nm is that the former two multilayers contain quasi-amorphous Mo layers, while the latter contains crystalline layers.

The difference in diffusion properties between crystalline and quasi-amorphous Mo layers is linked to the difference between the as-deposited structure of the multilayers. It is known that Mo layers crystallize at a thickness of approximately 2 nm [28, 55]. The as-deposited structure of the interfaces in Mo/Si multilayers is different in the crystalline and quasi-amorphous case. The crystalline Mo layers have an approximately 1 nm interface at the Mo-on-Si interface and a 0.5 nm interface at the Si-on-Mo interface. In multilayers with an quasi-amorphous Mo layer, both interfaces are about 1 nm thick [28, 29, 55]. If we focus on the crystalline case (2.8 nm Mo) in figure 4.1a we clearly see the difference between the diffusion through the Mo-on-Si interface (B_4C on Mo) and the Si-on-Mo interface (B_4C on Si). The, originally thinner, Si-on-Mo interface shows approximately a factor of two less period change than the, originally thicker, Mo-on-Si interface. This is in agreement with TEM investigations by Rosen et al [29].

The two Mo thicknesses that have a quasi-amorphous structure (1.3 nm and 1.8 nm) both show the same period change regardless of the position of the B_4C layer. In contrast to crystalline Mo multilayers, the quasi-amorphous Mo layers do not have the initially asymmetric interface thicknesses; they are both equally thick [55]. In this work we additionally find that, in contrast to multilayers with crystalline Mo layers, the diffusion through the interfaces of a multilayer is equally fast in the temperature range tested (up to 375°C).

Finally, we compare the period change of a multilayer with and without B_4C diffusion barriers. In figure 4.1b the period changes of two multilayers with B_4C barrier layers (3 and 6 in Table 4.1) are compared to a Mo/Si multilayer without B_4C layers.

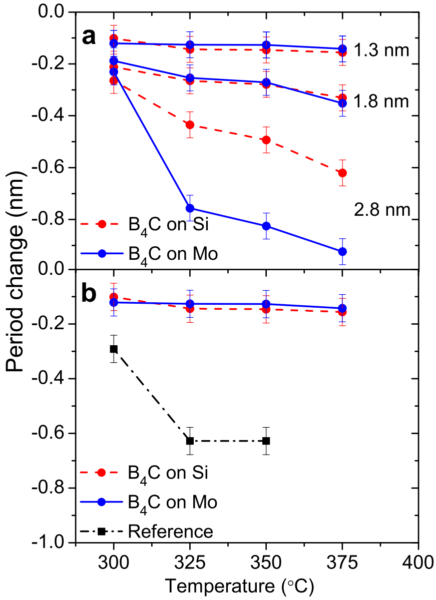

Figure 4.1: Period change as a function of the annealing temperature for a) multilayers with different Mo thicknesses and a B_4C diffusion barrier at either the Mo-on-Si or the Si-on-Mo interface, and b) multilayers with and without B_4C diffusion barriers for samples with the same amount of deposited Mo (1.3 nm) and Si (4.5 nm).

The multilayer without barrier layers shows a sharp increase in period change at 325°C, which has been earlier explained by a crystallization of the formed silicide interlayer [35]. During this phase transformation all Mo reacts with Si to form crystalline $MoSi_2$. The samples 3 and 6 have the same deposited amount of Mo and Si as the Mo/Si multilayer, but show a factor of six less period change compared to the reference Mo/Si multilayer, which will be explained in the discussion section of this chapter.

4.3.2 XRD

To study the crystalline structure of the Mo layers before annealing, WAXRD spectra were measured for all multilayers. Since it is known that the as-deposited crystalline structure of the Mo layer affects the diffusion properties of the multilayer [49], we will discuss this initial crystalline structure. Figure 4.2a shows the spectra for Mo thicknesses of 2.8 nm and figure 4.2b shows the spectra for Mo thicknesses of 1.8 nm. The spectra for 1.3 nm Mo layers are identical to the 1.8 nm Mo spectra (apart from a somewhat lower intensity). In both graphs, the spectra for a reference multilayer (samples 7 or 8, without B_4C) and a sample with B_4C on top of Mo (multilayer 1 or 2)

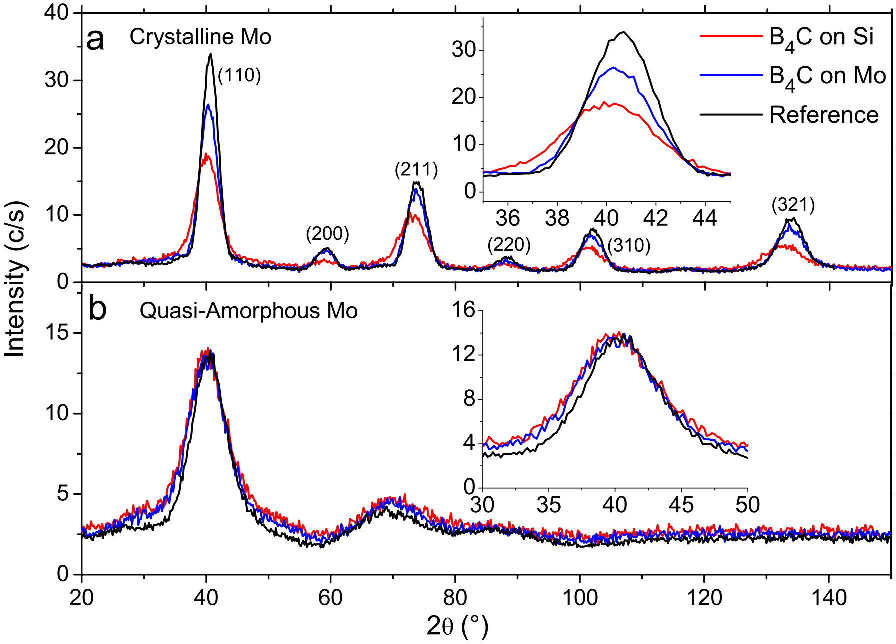

Figure 4.2: a) XRD spectra for samples with crystalline Mo layers (2.8 nm Mo layers). b) XRD spectrum of quasi-amorphous samples. The inserts in both graphs are magnifications of the first peak.

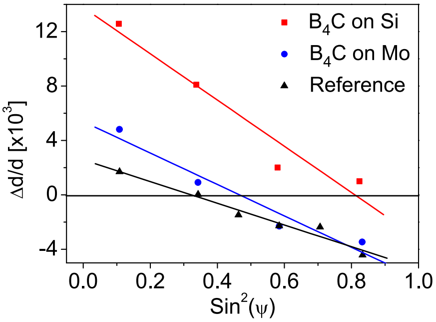

Figure 4.3: Lattice strain versus $\sin^2\psi$ for plot samples 4 (B_4C on Si) and 1 (B_4C on Mo) compared to 7 (No B_4C).

and on top of Si (samples 4 or 5) are compared. The two different thicknesses show a clearly different diffraction pattern. The pattern in figure 4.2a is identified as polycrystalline bcc Mo. The pattern in figure 4.2b clearly differs from the Mo diffraction pattern, although there is still some evidence of a short range order resulting from interaction between the Mo atoms, as described in reference [56]. The morphology of Mo, polycrystalline or quasi-amorphous, is indicated in Table 4.1 for all samples.

The lattice spacing's of the Mo crystallites are studied by analyzing the peak positions of the diffraction maxima. The insert of figure 4.2a shows the (110) peak in more detail. We observe a shift of this peak for both B_4C on top of Si as well B_4C on top of Mo, although the shift is more pronounced in the first case. These shifts indicate an expansion of the Mo lattice in the direction perpendicular to the surface. The expansion of the multilayer with B_4C on top of Si has also been observed by Böttger et al. [44]. In their work the expansion of the Mo lattice is attributed to stress. Although stress can be the cause of lattice expansions, in this case we should also consider the presence of interstitial B and/or C atoms in the Mo lattice, causing a change in the lattice constants.

To analyze possible causes for the lattice expansion, we have plotted the relative shift of the XRD peak positions from the theoretical values against $\sin^2(\psi)$, where ψ is the angle between the multilayer surface normal and the normal of the lattice planes. In Mo/Si multilayers the stress can be calculated from the slope of this graph according to the method described in textbooks such as [60]. Compared to the Mo/Si multilayer, the multilayer with a B_4C on top of Mo shows a small increase of the lattice spacing's only for small angles. This indicates that the crystals are slightly more stressed when B_4C is added. However, when B_4C is underneath Mo (B_4C on top of Si) we observe a clear expansion of the lattice in *all* directions. This indicates that when B_4C is underneath Mo, it causes a change in the lattice constants of Mo. It is known that crystal lattices can expand when small amounts of impurities are added to the matrix [73, 74], which is in support of the expansion of the Mo lattice due to a possible inclusion of boron or carbon atoms from the B_4C.

For the quasi-amorphous Mo spectra a full stress analysis is not possible, but we observe a similar, though smaller, shift of the peak as observed in the crystalline spectra (insert of figure 4.2b). For the quasi-amorphous case the shift is equally large for both B_4C on Mo and B_4C on Si. This indicates that the lattice expansion does not depend on the location of the B_4C barrier, in contrast to the crystalline case.

As a result, we observe, as-deposited, an expansion of the lattice in *both* quasi-amorphous samples. When Mo is crystalline, we only observe this expansion when B_4C is under Mo. We suggest that this expansion and the inclusion of boron or carbon atoms in Mo only takes place in noticeable amounts when Mo is quasi-amorphous. Before the critical Mo thickness for crystallization is reached, the Mo layer grows quasi-amorphous as well. If Mo grows on B_4C boron and carbon can interact with the quasi-amorphous Mo layer before the layer crystallizes, causing an increase of the Mo lattice constants. On the other hand, if B_4C is deposited on top of Mo, B and C interact with a crystalline layer, and therefore no change of the lattice constants is observed.

4.3.3 XPS

The results from XPS studies before annealing and after the final step (at 375°C) of annealing of the multilayer with B_4C on top of Si and a Mo thickness of 1.3 nm (sample 6) are shown in figure 4.4. In this graph the in-depth traces of the atomic concentrations of the four elements of the multilayer are shown. The Mo and C traces do not change significantly during annealing. The dotted lines indicate the maxima in the B and Mo traces before and after annealing. A clear shift of the B maximum towards the Mo maximum is observed. This shift indicates that B diffuses into Mo during annealing. In addition the amplitude of the B signal reduces after annealing, which shows that B is more smeared out, due to the diffusion. The amplitude of the Si trace reduces as well, which is most likely not caused by diffusion (the position is unchanged), but by the different chemical environments that are being Ar^+ eroded (intact B_4C barrier compared to decomposed barrier). The data shown in figure 4.4 is from sample 6, but the shift of B towards Mo due to annealing is observed for all of multilayers in this investigation.

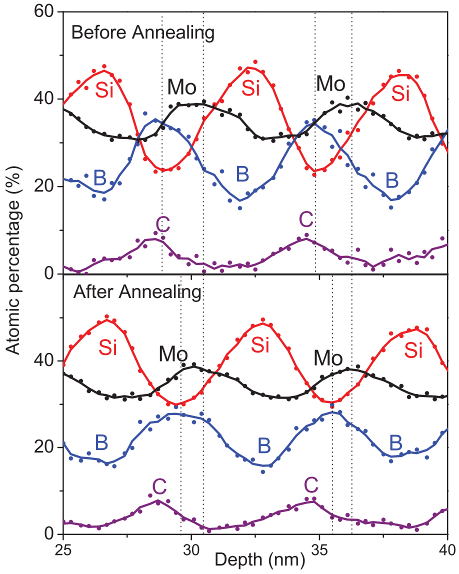

Figure 4.4: XPS depth profile before annealing (top) and after annealing (bottom) at 375°C for B_4C on Mo (sample 3). The vertical lines indicate the top of the Mo and the B layers. A clear shift of B atoms towards Mo is observed.

4.4 Discussion

The sequential annealing data from figure 4.1 shows that diffusion in the samples with quasi-amorphous Mo layers is slower than in those with crystalline layers. This is in contrast with the observations made in our earlier work, where a Si_3N_4 diffusion barrier was applied on top of Si [49]. From those multilayers, the ones with quasi-amorphous Mo layers showed faster diffusion than those with crystalline Mo layers. We propose here that this surprising difference in the behaviour of the systems is caused by the formation of a Mo_xB_y in a part of the Mo layer during annealing.

The WAXRD spectra, before annealing, show lattice expansions if a B_4C layer interacts with an amorphous Mo layer. This is an indication that B or C atoms are already interacting with the Mo layer in the as-deposited state. During annealing, the period change in the sequential annealing experiments shows that thinner Mo layers have less final period change. Additionally, we observe that there is 0.5 nm less period change for multilayers with B_4C layers than in the case of multilayers without B_4C layers. These observations indicate that part of the Mo layer has formed a compound with either B or C atoms during annealing. This compound is thermally more stable than the Mo layer and therefore that part of the layer does not react with Si. This explains why we observe less period change in a multilayer with B_4C than in the multilayer without B_4C. Moreover, if part of the layer has formed a stable compound, this effect is expected to be relatively larger for thinner layers, since a larger fraction of the layer has reacted. Therefore thinner Mo layers are expected to have less final period change, in agreement with our findings

The XPS measurements show a clear shift of the boron distribution towards the Mo layer, suggesting that B forms a Mo compound during annealing. This compound is thermodynamically more stable than the Mo layer and therefore reduces the reaction rate of the formation of $MoSi_2$, which will reduce the diffusion rate as well. The thermodynamic formation enthalpies for Mo compounds are listed in Table 4.2. From this table it is clear that molybdenum borides have a lower formation enthalpy than molybdenum carbides. We also see that some borides (for instance MoB or

Table 4.2: Formation enthalpies (in kJ/mol of atoms) of various Mo compounds taken from reference[34].

Compound	Δ H (kJ/mol)
MoC	-15
Mo_2C	-5
MoB	-62
Mo_2B_5	-54
MoB_2	-57
Mo_3B_2	-35
Mo_2B	-32
$MoSi_2$	-44

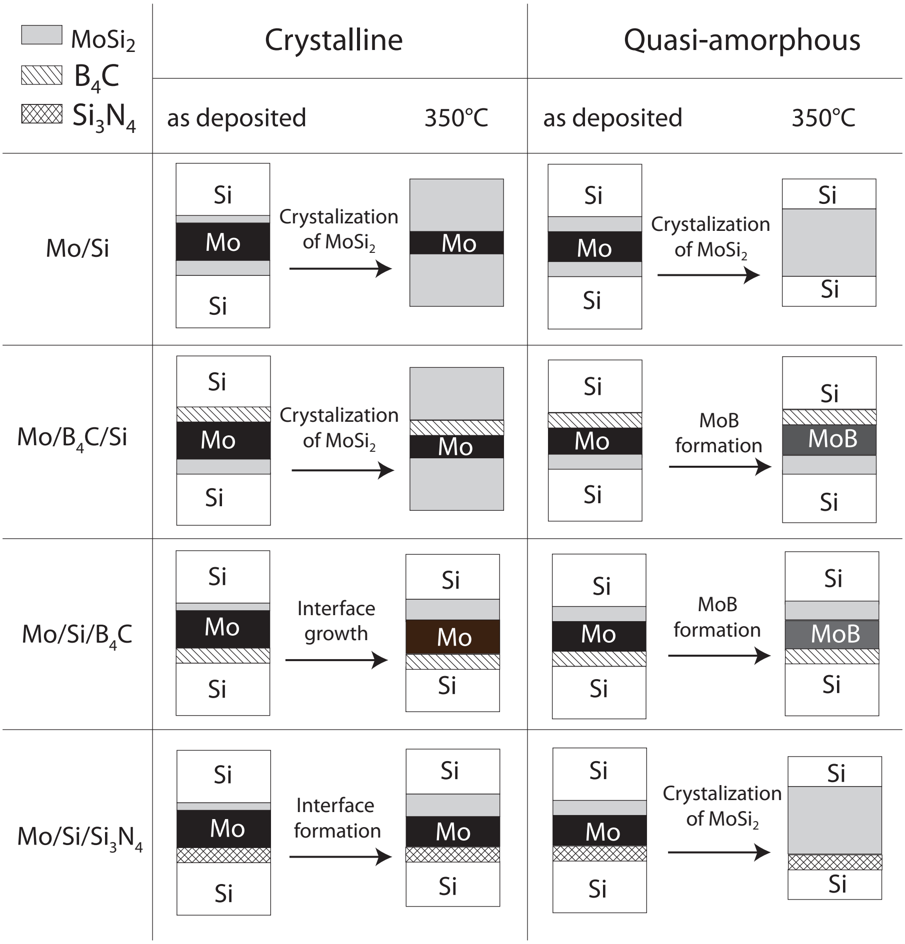

Figure 4.5: Graphical overview of the different diffusion barrier systems discussed in this chapter and chapter 4. The individual layers of all the systems are shown before and after annealing and for crystalline and quasi-amorphous Mo layers.

MoB_2) have a significantly lower formation enthalpy than that of $MoSi_2$, which is the compound formed at the interfaces during annealing of a Mo/Si multilayer. Therefore it is likely that a Mo_xB_y compound indeed stabilizes the layer and slows down the diffusion during annealing, which explains the difference between the results for a B_4C diffusion barrier and a Si_3N_4 diffusion barrier in chapter 3. To illustrate the chemical reactions and diffusion effects taking place during annealing of multilayers with B_4C diffusion barriers and Si_3N_4 diffusion barriers, an overview of the different systems is shown in figure 4.5. The main difference between the two systems is the fact that B_4C has a chemical interaction with the Mo layer, while Si_3N_4 does not.

4.5 Conclusions

The morphology of Mo/Si multilayers with B_4C diffusion barriers was investigated under thermal annealing, using X-ray reflectivity, X-ray diffraction, and X-ray photoemission spectroscopy. Using layered systems separated by B_4C diffusion barriers, the results show that multilayers with quasi-amorphous Mo layers show less period change than multilayers with crystalline layers. This result is in contrast to previous data on with Si_3N_4 diffusion barriers (chapter 3) where the multilayers with crystalline Mo were found to be more stable. We have shown that this enhanced thermal stability with B_4C barrier layers is caused by the formation of Mo_xB_y layers. Since Mo_xB_y is thermodynamically more stable than $MoSi_2$, which forms during the thermally induced diffusion in Mo/Si systems without diffusion barriers, the reaction rate and therefore also the diffusion rate is reduced significantly.

Chapter 5

In-situ study of the diffusion-reaction mechanism in Mo/Si multilayered films

Abstract

We present a low temperature diffusion study on the formation of intermixing zones between periodic, nanometer thick films consisting of Mo and Si. An *in-situ* X-ray diffraction method at pm-accuracy was developed, including a model that explains the period change observed by diffusion limited interface growth. Experiments were carried out on Mo/Si multilayered films in the temperature range of 100°C-275°C, resulting in the determination of diffusion coefficients. Temperature scaling showed Arrhenius-type behaviour of the diffusion constant over the entire temperature range, with an activation energy of 0.5 eV.

5.1 Introduction

Diffusion coefficients in thin films at relatively low temperatures (typically a few hundred degrees) are generally lower than 10^{-23} cm^2/s [39], and cannot be measured with traditional diffusion methods, which are limited to typically 10^{-19} cm^2/s [75, 76]. In order to increase the diffusion coefficient to measurable quantities, experiments are generally done at higher temperatures than those relevant for most applications. However, at these elevated temperatures the internal structure of thin films (crystallinity, stress, etc.) can change and this can dramatically influence the diffusion speed [46].

DuMond and Youtz [38] developed a method to measure low diffusion speeds. They monitored the intensity of the first order Bragg peak of the grazing incidence X-ray reflection (GIXR) spectrum of a multilayer stack of bilayers of two alternating materials. From this, they were able to extract diffusion constants at a much higher accuracy than traditional diffusion experiments. This method has since then been used by other authors [39–41] to monitor diffusion in multilayer stacks with different material combinations. A drawback of the model in [38] is that it does not consider that a compound can be formed in between the layers. Such a compound grows over time, thereby decreasing the effective diffusion flux through the interface.

We introduce a new, *in-situ* method for measuring interface growth in multilayers, with high sensitivity at relatively low temperatures. For this we developed a model that accounts for the growing interfaces between the two materials, thereby accounting for the changing diffusion flux through the interface. The procedure is based on the measurement of the changes in Bragg peak positions that result from the change in the multilayer period. This period change is then interpreted in terms of the growth of compound interfaces between the layers. The growth of these interfaces will be shown to be governed by the parabolic growth law, which states that a compound interface grows quadratically over time. From this model the diffusion constant is obtained.

Previous methods for determining the growth of the interface were mostly based on TEM investigations which have a maximum resolution of 50 pm [29, 77]. The method used in this work has a sub-picometer accuracy which has made it possible to study these mechanisms in the required amount of detail for the first time. This essentially makes it possible to measure the diffusion in thin film layered structures at the relatively low temperatures which are needed for many applications.

5.2 Experimental

The multilayer systems in this study consist of 50 alternating layers of Mo (2.8 nm) and Si (4.1 nm) which were deposited using electron-beam deposition onto superpolished 25 × 25 mm Si substrates. The details of the deposition process are described in [64, 65]. After deposition, these samples were annealed *in-situ* during X-ray reflection measurements. The diffractometer uses Cu Kα radiation with a wavelength of 0.15406 nm, which is selected by a four bounce asymmetrically cut

Ge (220) monochromator. The instrumental broadening of the used measurement configuration is 0.005°. A detailed description of the *in-situ* annealing setup inside the diffractometer, which is a commercial Anton Paar stage, is given elsewhere [57].

Before annealing the sample position is aligned with respect to the X-ray beam and a reference spectrum is recorded. An example of such a reference scan is shown in figure 5.1. Afterwards, the sample is heated to the required temperature. To account for thermal expansions in the sample stage, the sample position in the beam is realigned, after which the measurements start. We have determined experimentally that angular realignment is not necessary. The time between the start of heating and the first data point is approximately 10 minutes. During this time no data can be acquired. The data acquisition for each data point takes approximately 5 minutes.

The annealing temperatures selected are between 100°C and 275°C. These temperatures are well below the reported crystallization temperature of 325°C at which crystalline $MoSi_2$ is formed, followed by a change in diffusion properties [31].

The difference of the period of the multilayer before and after a specific time of annealing can be determined by comparing the position of two selected diffraction peaks before and during annealing. The shift between the two is then fitted using the Bragg formula, which for small θ can be written as

$$(\Delta\theta_2 - \Delta\theta_1) = \Delta m \lambda \left(\frac{1}{2d_0} - \frac{1}{2d} \right), \tag{5.1}$$

where Δm is the Bragg order difference between the two peaks used, d_0 is the period of the multilayer before annealing, d is the period during annealing and $\Delta\theta_1$ and $\Delta\theta_2$ are the peak shifts during annealing of the first peak and second peak considered.

To determine $\Delta\theta_1$ or $\Delta\theta_2$ we first fit the n^{th} Bragg order peak of the spectrum measured before and after annealing with a cubic spline function. The shift is then determined by shifting the peak before and after annealing over each other until we find the optimal position by the least squares method. By specifically considering *relative* shifts in Bragg peak positions, this method is independent of a possible misalignment of the sample in θ, since the misalignment is equal for both peaks ($\Delta\theta_1$ or $\Delta\theta_2$), and it is not affected by the instrumental broadening. Furthermore, by comparing the same Bragg orders before and after annealing, this method is insensitive to errors introduced by the shape of the peak. Peak shapes can otherwise make it difficult to determine the exact peak position. But, since the peak shape does not change during annealing, a *shift* in peak position is easy to determine.

For the most accurate determination of the period change, the measured peaks should preferably be well distanced in θ (so that Δm is large). At lower values of θ, the second Bragg order peak is selected, because the position of the first order peak is significantly influenced by the absorption in the multilayer, which causes determination of the period change to be less accurate. This exclusion of the first order Bragg peak is discussed by Voorma [62]. At high θ, we selected the seventh and eighth Bragg orders; higher orders were not considered due to their low intensities. The selected peaks are illustrated in figure 5.1. In the data analysis we calculate the

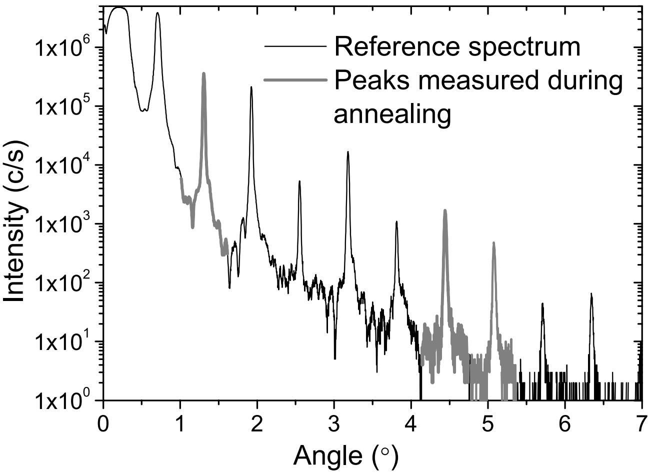

Figure 5.1: Example of a reference scan, the grey lines indicate the peaks which are measured during annealing.

period change with equation 5.1 once using the second and the seventh peak and once more using the second and the eighth peak, showing no significant differences. The data reported here is averaged over both calculations.

5.3 Results and discussion

For each sample a reference spectrum is measured before annealing. An example of such a reference spectrum is shown in figure 5.1. From this spectrum the period before annealing (d_0, equation 5.1) is determined using the modified Bragg equation (equation 2.3. During annealing we observe an angular shift of all the measured Bragg orders. As an example we show the seventh order Bragg peak of the sample annealed at 275°C for annealing up to 1h, 10h and 60h in figure 5.2. In this graph both the data and the cubic splines through the data are depicted. Note that the observed intensity change of the peaks is connected to the angular dependence of the form factor [78].

In figure 5.3 the derived period changes are plotted as a function of annealing time at various temperatures. The data in figure 5.3 is corrected for thermal expansion using bulk thermal expansion coefficients of Mo and Si. These are taken from literature [79] and were experimentally verified to be valid for these multilayers, by measuring the period change after cooling down the multilayer and comparing this to the last data point during annealing. In addition high resolution measurements of the multilayer period between 25 and 100°C were performed at a synchrotron facility using a stabilized multilayer with thin barrier layers. The thermal expansion

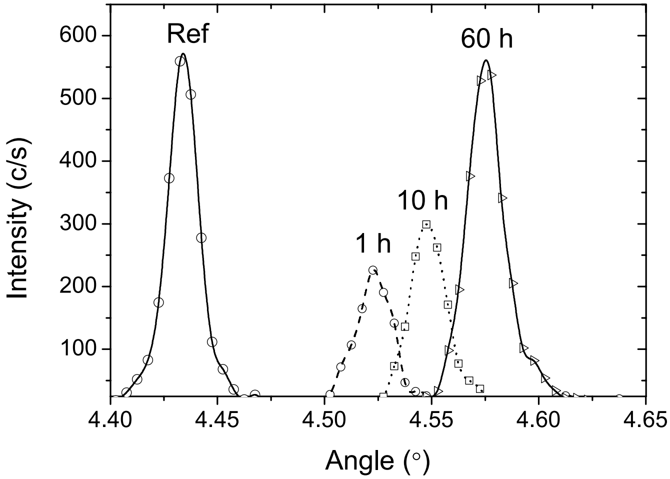

Figure 5.2: The seventh Bragg order peak at different times of the annealing process at 275°C.

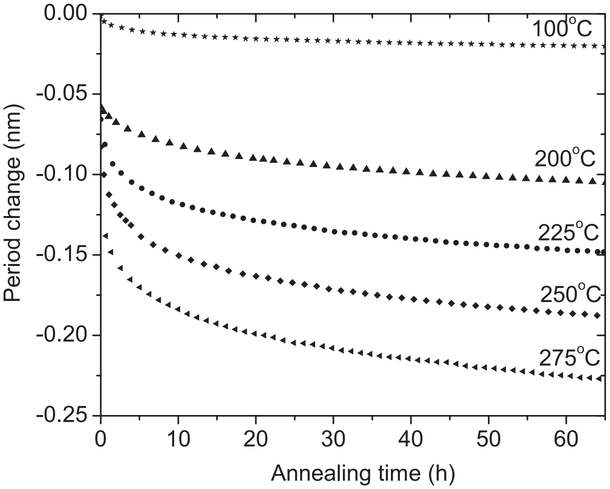

Figure 5.3: The period change of Mo/Si multilayers as a function of annealing time at different temperatures. The period changes are corrected for thermal expansion. For clarity, a window average of 10 data points was taken for all graphs.

of this multilayer exactly matched the values in literature. The statistical error in determining the period change plotted in figure 5.3 is 0.5 pm [77], which is two orders of magnitude lower than the typical 50 pm errors in for instance TEM investigations [29, 53, 80].

We observe that for temperatures higher than 100°C the curve does not start at the origin. This is caused by the fact that no measurements can be performed during initial ramp-up of the temperature and re-aligning of the sample ($\sim$10 minutes).

In principle, the period change observed in figure 5.3 can be caused by either elimination of free volume or the formation of high density silicides at the interfaces. From previous work [31, 33, 70] it is known that amorphous $MoSi_2$ is formed at the interfaces of a Mo/Si multilayer during annealing. The work of Nedelcu et al [31], in which XRD, XPS and TEM measurements were used, shows that the dominating mechanism for period change is the formation of $MoSi_2$. Considering these results we presume that the effect of free volume on the period change can be neglected. For this reason, the change in the multilayer period is directly converted to a change in interface thickness assuming bulk densities for Mo, Si and $MoSi_2$.

It should be noted that the interface changes detected in this study concern the sum of changes on both the Mo-on-Si and the Si-on-Mo interfaces. This means that only the effective diffusion through both interfaces simultaneously is studied. To resolve the diffusion through one type of interface, diffusion barriers on the alternate interfaces could be used.

In general, the growth of compound interfaces between two materials is governed by a diffusion-reaction mechanism and can be described by a two step process. In the first step, atoms diffuse through the initially formed interface. In the second step the materials react chemically forming additional interface. Due to the increasing interface thickness, the diffusion flux through the interface decreases continuously over time.

The mechanism of a growing compound interlayer is described by Gösele et al [42]. They consider two limiting cases:

1. Initially, the compound interface is thin and diffusion through this interface is relatively fast. In this case the chemical reaction to form the compound interlayer is the rate determining step. This will be called *reaction limited* interface growth, and the interface width (x) should increase linear with time (t):

$$x \propto t. \tag{5.2}$$

2. After a sufficiently thick compound interlayer has been formed, the diffusion flux will have slowed down to such an extent that diffusion through the interface becomes the rate limiting step. In the case of *diffusion limited* interface growth, the interface width should follow:

$$x^2 = D^* t, \tag{5.3}$$

   where D^* is an effective interdiffusion coefficient, related to the real diffusion coefficient. Equation 5.3 is also referred to as the parabolic growth law of interfaces. [43].

From figure 5.3 it appears that we do *not* observe the linear part that is expected from the reaction limited stage described by equation 5.2. This phase can already have passed since it is well known that during deposition an interface already forms between Mo and Si [28, 29, 78]. This implies that we should be able to fully describe the data with the diffusion limited case described in equation 5.3 from the very beginning. However, analysis of the data shown in figure 5.3, suggests that it does not obey the parabolic growth law in the very beginning either. Since the data, in the very beginning cannot be described by either the reaction limited or the diffusion limited extreme, it is likely that a transition is observed, in which the interfaces are changed from one compound to another, energetically more favourable one, resulting in the observed period change. This initial compound formation cannot be described by the theory described above and therefore we need to correct for this in our model.

We introduce a correction factor in both the interface thickness and the time, in order to exclude the compound formation during the first hours of annealing from the model. We correct for the amount of interface formed before diffusion limited interface growth becomes dominant and denote by introducing x_0, and the time before this regime is entered by t_0. With these correction factors equation 5.3 becomes:

$$(x - x_0)^2 = D^*(t - t_0). \tag{5.4}$$

The factor x_0 is uniquely fitted to find a linear fit in the diffusion limited regime, that starts at time t_0. Using this model, the experimental data can be accurately described, as shown in figure 5.4, where the expected linear behaviour is obtained for all temperatures. Values of x_0 of a few angstroms were fitted, depending on the temperature. The initial annealing time (t_0) before the diffusion limited case is reached, i.e. where the linear regime as in figure 5.4 and equation 5.4 holds, is determined from the plotted curves to be lower for higher temperatures. This suggests that the initial process, which is most likely reformation of the interface compound, is faster for higher temperatures. A rearranging reaction is expected to go faster at higher temperature, which is consistent with our observations.

Using equation 5.4, values for D^* were determined for all temperatures. Since the value of D^* is proportional to the diffusion coefficient, the data should obey the Arrhenius equation,

$$D^* = D_0 \exp \frac{-E_a}{kT}, \tag{5.5}$$

where E_a is the activation energy, D_0 the pre-exponential factor, k the Boltzmann constant and T the temperature in Kelvin. The Arrhenius plot of the D^* values is given in figure 5.5. The data exhibits clear Arrhenius type behaviour for the temperature range used in this investigation, with an activation energy of 0.5 eV. This value is slightly lower than those found in literature (ranging from 0.8-2.4 eV [29, 40, 81–83]), which could be attributed to the specific growth conditions. In the current study, the Mo/Si multilayers were prepared using electron beam deposition, while in previous literature studies magnetron deposited samples were used. The low energy of the deposited particles in the electron beam deposition process will result in a slightly different structure of the multilayer compared to the structure that forms at

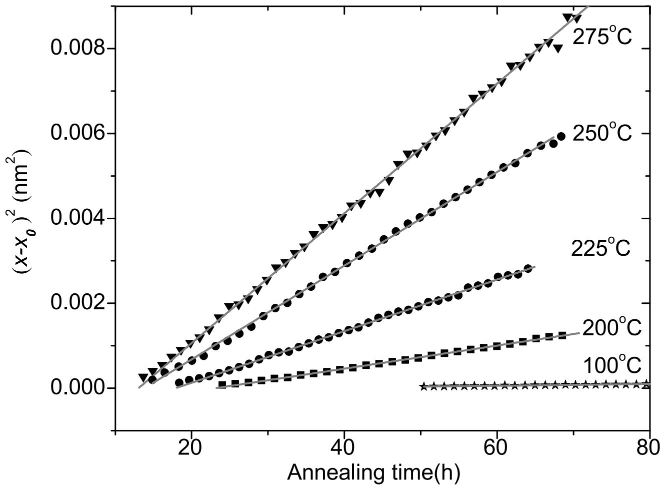

Figure 5.4: The corrected interface width squared, $(x - x_0)^2$, plotted as a function of corrected annealing time. The value $(x - x_0)^2$ can be modelled linearly with time after the formation of x_0 interface and after t_0. For clarity, a window average of 10 data points was taken for all graphs and only the part of the data in the diffusion limited case is shown.

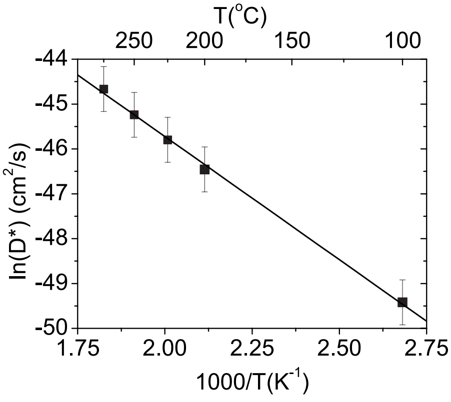

Figure 5.5: Arrhenius plot for the diffusion coefficients in a Mo/Si multilayer.

the higher energies of magnetron deposition, which could explain the difference in activation energy.

5.4 Conclusions

The diffusion kinetics in multilayers consisting of nanometer thick films have been resolved with sub-picometer accuracy. *In-situ* grazing incidence X-ray reflectometry was used to monitor the changes in the multilayer structure during thermal annealing. The experimental data were analyzed by taking into account the compound interface growth. In the first hours of annealing, the multilayer period does not follow either the diffusion or the reaction limited interface growth. The observed initial period changes can be attributed to the rearrangement of the compound at the interfaces. In the next phase of annealing, the interface changes are well described by the parabolic growth law, indicating a clearly diffusion limited interface growth stage. The diffusion coefficients obtained from fitting the data to the parabolic growth law showed Arrhenius-type behaviour over the complete range of temperatures, with an activation energy of 0.5 eV.

This suggests that the initial process, which is most likely reformation of the interface compound, is faster for higher temperatures. A rearranging reaction is expected to go faster at higher temperature, which is consistent with our observations. This method is also suitable for other materials combinations, if the relation between period change and interface formation is known. Without such information only a relative comparison of systems with and without diffusion barrier as well as temperature scaling are still possible.

Chapter 6

Ion assisted growth of B_4C diffusion barrier layers in Mo/Si multilayered structures

Abstract

We investigated the thermal stability of e-beam deposited Mo/B_4C/Si/B_4C layered systems, with and without ion assistance during the growth of the B_4C diffusion barrier layers. The thermal stability was investigated by *in-situ* thermal annealing during grazing incidence X-ray reflection. By studying partially treated B_4C barrier layers, we found that the improvement in thermal stability is caused by an enhanced density of the B_4C layer.

6.1 Introduction

Multilayer mirrors are widely applied to reflect radiation from the far ultraviolet through the soft X-ray wavelength regime. They are used in for instance telescopes that observe ultraviolet radiation, in new XUV and soft X-ray free electron lasers and in Extreme UV photolithography machines. Multilayer mirrors consist of stacks of bilayers, from which UV radiation can be reflected if the Bragg condition is met. For the regime between λ = 12.5-25 nm, Mo/Si multilayers are the most widely used material combination, because of their favourable optical properties; at 13.5 nm, the wavelength of choice for future photolithography, they have a reflection just below 70% of the incident light when used at near normal incidence [55, 64, 84, 85].

Under very high power load conditions or enhanced temperatures, Mo/Si multilayers may be susceptible to layer intermixing because of interdiffusion of Mo and Si and subsequent molybdenum silicide formation at the interfaces [29, 31]. This reduces the optical contrast in these Bragg mirrors and, due to a larger density of the silicides compared to the average densities of the Mo and Si layers, it also reduces the thickness of the bilayer, also referred to as the multilayer period. This reduction in period will cause a large drop in the reflection at the desired wavelength, since the particular Bragg condition is no longer met. To prevent interdiffusion at the interfaces, compound diffusion barriers are often used. One of these materials is B_4C, which has been shown to significantly reduce the diffusion rate through the interfaces in multilayers [47, 70].

Diffusion barriers can work in two ways, namely as a direct physical barrier and as a sacrificial material, in which case the barrier forms a chemical compound upon reaction with the other layer materials. If the chemical potential for that barrier material is lower than for standard Mo-silicides, this will reduce the Mo-silicide formation rate. From previous work [46, 86] and from chapter 4 we know that B_4C barrier layers do react with the Mo and Si layer. In this work we discuss the thermal diffusion properties of B_4C diffusion barriers in Mo/Si multilayers, deposited with different atom surface energies: the energy of the deposited atoms was controlled by using a low energy deposition technique (e-beam evaporation) while subsequently adding energy using ion bombardment during growth. The thermal resistance of these multilayers was studied by annealing at 200°C, a value selected to be sufficiently high to induce interface growth due to diffusion. We show that the physical barrier properties of the B_4C layers can significantly be improved by applying low-energy ion treatment.

6.2 Experimental

6.2.1 Deposition

The multilayer structures were deposited using electron beam deposition onto superpolished Si substrates, using an UHV (base pressure $< 2 \cdot 10^{-8}$ mbar) deposition facility. The thicknesses of the layers were controlled by an *in-situ* X-ray reflectometer that monitored the X-ray reflection of the sample during multilayer growth as well as quartz mass balances. The sample holder rotated at 1 Hz to ensure a homogeneous coating in the azimuthal direction. To prevent the buildup of roughness, all Si layers were smoothened directly upon deposition using low energy Kr^+ ion treatment. A detailed description of the setup can be found in [65].

All multilayers studied had a Mo/B_4C/Si/B_4C stack with a total period of the four layers of 6.95 ± 0.05 nm. The B_4C diffusion barrier layers were 1.0 ± 0.07 nm thick, the Mo layers were 1.8 ± 0.07 nm and the Si layers were 3.2 ± 0.07 nm in all cases. Since the thickness of the Mo layers was below 2 nm they are all quasi-amorphous (see section 1.3.5).

To investigate the influence of ion surface bombardment during deposition of B_4C on the B_4C diffusion barrier quality, we deposited several multilayers with B_4C layers with (partial) Kr^+ ion assisted deposition (IAD). The ions were emitted from a Kaufman type ion source with an energy of 80 eV, at an angle of 45°. The ion (Kr^+) to atom (C or B) ratio was approximately 1:1. The following samples were produced with the above error margins:

- One multilayer sample with full IAD, i.e. during the full evaporation period of all individual B_4C layers, and one sample without any IAD.
- Two multilayer samples where the B_4C layers on only one position (i.e. on-top-of-Si or on-top-of-Mo) were treated.
- Three multilayer samples with partial (25%, 50% and 75%) IAD of both B_4C layers. In these cases the B_4C layer growth was started with IAD applied, while it was switched off when the desired fraction of the full layer was reached.
- One multilayer sample with only post treatment of the B_4C layers i.e. ion treatment after completion of the growth of each B_4C barrier layer.
- Two B_4C single film reference samples, one with and one without ion assistance, were prepared to check the effect of ion assistance during B_4C growth on the density of the B_4C layer. Their nominal thickness was 15 nm, sufficiently thick to rule out interface/surface effects. These samples were made to extract the layer densities and compositions.

6.2.2 Analysis

The reference B_4C single films were investigated by grazing incidence X-ray reflectometry (GIXR) to determine their density, thickness and roughness. The GIXR reflective curves were recorded with a diffractometer using Cu Kα (λ = 0.15406 nm) radiation and fitted with a model in the software package IMD [61]. The stoichiometries of both reference layers were determined using X-ray photoelectron spectroscopy (XPS) with sputter depth profiling.

The thermal diffusion behaviour of all multilayer samples was investigated by thermal annealing at a temperature of 200°C. The multilayer period change, during annealing is connected to the change in the Bragg peak positions observed in the

GIXR reflective curves, as discussed in chapter 5. All period changes presented in this study were corrected for thermal expansion by the factors obtained from literature, which were confirmed by measurement of the period after the sample was cooled down.

The period change measured during annealing is predominantly caused by interdiffusion of Mo and Si, followed by the formation of $MoSi_2$. This interface has a higher density than the average density of the original Mo and Si layers, which causes the period to reduce. The period change was converted to an interface thickness increase using the densities of Mo, Si and $MoSi_2$. From the interface growth rate, a diffusion coefficient was determined. The method of determining the diffusion coefficient is discussed in detail in chapter 5.

6.3 Results and discussion

6.3.1 Thermal stability upon IAD

Figure 6.1 shows the period changes for samples with B_4C at both interfaces, in the case of deposition with and without ion assistance. Both samples had an initial expansion of the period (for the non-IAD treated sample this is not visible in the graph). This expansion was observed in all multilayers containing B_4C barrier layers presented in this work and is most likely caused by initial chemical interaction between the B_4C barrier layer and the Mo and/or the Si layer [86]. After this initial period

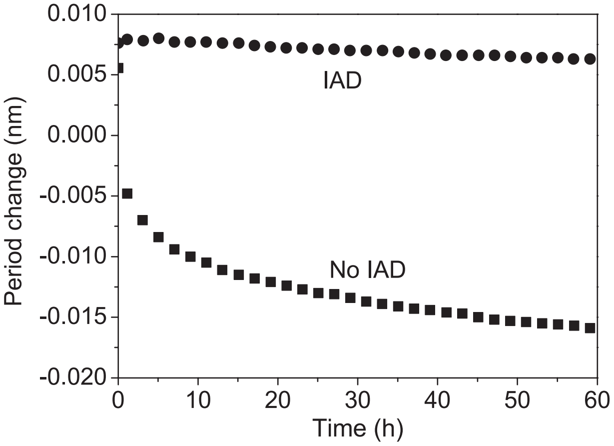

Figure 6.1: Period change over time for multilayers with and without ion treatment of the B_4C barrier layers, annealed at 200°C. Each symbol denotes an average of 10 data points, the statistical error of the data points is 0.5 pm.

increase we observed a decrease of the period which is attributed to interdiffusion induced $MoSi_2$ formation, as observed in samples without B_4C barriers [29, 31]. We observed a clear decrease in the formation of $MoSi_2$ in the multilayer with IAD B_4C barrier layers, which implies that the diffusion barrier properties of the B_4C have improved by the ion assistance during the layer deposition.

Generally, there could be several reasons for this improvement [87]. Firstly, the chemical interaction, between B_4C and Mo and/or Si, could increase due to an increased ion-induced intermixing zone. From literature we know that chemical reactions between B_4C and Si or Mo do exist [45–47, 86], especially upon thermal annealing. If the chemical compounds which are formed have a lower formation enthalpy than $MoSi_2$, it will be more difficult to form more silicide at the interface and the diffusion rate will decrease. Secondly, the density of the B_4C layer could increase, which would decrease the diffusion speed due to a smaller amount of voids in the structure. The link between ion treatment and barrier density, and therefore the barrier properties, has been shown in for instance references [88, 89], for different compounds. A similar effect may be expected with B_4C barrier layers. We will demonstrate that this is the case.

6.3.2 Treatment of a single B_4C interface type

Since the chemistry at opposite interface types (i.e. the B_4C-on-Mo and the B_4C-on-Si interface) is in principle expected to be different, the effect of ion treatment

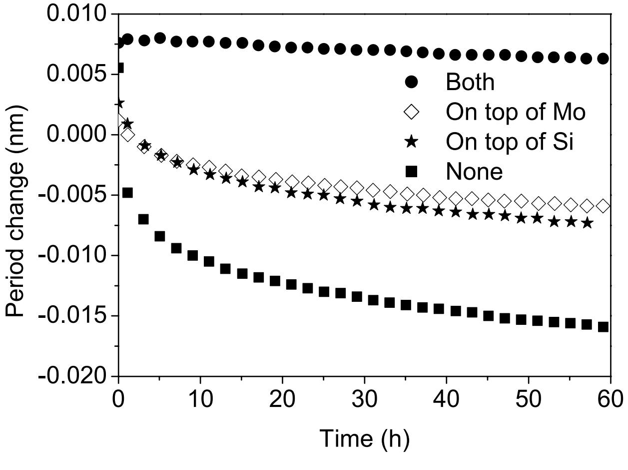

Figure 6.2: Period change over time of multilayers with ion treatment of B_4C layers applied either on top of Si or on Mo. As reference, the data for the treatment of all B_4C and that for treatment of none of the B_4C layers is shown as well. Each symbol denotes an average over 10 data points, the statistical error of the data points is 0.5 pm.

during deposition can be different as well. In principle, the thermal stability effect observed in figure 6.1 could be caused by an effect at both interfaces. To clarify this, both types of interfaces were studied independently. In figure 6.2 we observe that the period change of a multilayer with IAD applied at the B_4C-on-Mo layer is almost identical to that of a multilayer with IAD applied at the opposite, B_4C-on-Si layer. This indicates that the effect of ion treatment of the B_4C is the same at both interfaces. The small difference that is still observed could be explained by a minor difference in the absolute thickness of the B_4C interfaces for both systems. We therefore conclude that a change in the chemistry at the interface does not to play a large role in the observed improved stability of multilayers with B_4C layers deposited using ion assistance.

6.3.3 Single B_4C layer

The density and composition of a thin layer inside a multilayer can not easily be determined directly. To obtain information on the effect of ion treatment on the B_4C layer, we prepared single B_4C layers (nominal thickness 15 nm) with and without IAD, and determined their density and composition by GIXR and XPS. The GIXR reflective curves were fitted using the software program IMD [61]. The model stack consisted of a Si substrate, a 2 nm thick SiO_2 layer (the native oxide on the Si wafer substrate), and a B_4C layer with varying density, thickness and roughness.

The results of the GIXR scan and the fitted model are shown in figure 6.3. The critical angle region is the most sensitive to changes in the density and is therefore shown at a linear scale in the insets. The resulting model parameters for the layer without IAD are: a thickness of 17.8±0.05 nm, a density of 2.3 ± 0.1 g/cm^3 and a roughness of 6 ± 1 Å. The layer with IAD has a fitted thickness of 16.8±0.05 nm, a density of 2.6 ± 0.1 g/cm^3 and roughness of 4.5 ± 1 Å. These values should be compared to the tabulated bulk density of B_4C of 2.52 g/cm^3 [79], showing that the density of the layer without ion assistance is clearly below this value, while the density of the ion assisted case is around this value, within the accuracy of the fit. These results confirm the an increase of the B_4C density due to IAD.

Furthermore, XPS measurements revealed that the stoichiometry of the layers was the same with and without IAD, apart from a 1% residual presence of Kr atoms in the layer in the case of IAD. Due to the high mass of Kr atoms compared to B or C atoms, the density of the layer could increase by the addition of these Kr atoms. However, a worst case scenario, in which a Kr atom is added to the structure without removing a B or C atom, would only result in a density increase from 2.3 to 2.4 g/cm^3 for 1% Kr contamination. In reality the atomic radius of Kr is approximately 1.5 times larger than that of B or C atoms [90], suggesting that addition of Kr to the structure should come at a loss of B and/or C atoms, increasing the density to a value well below 2.4 g/cm^3, i.e. by no means explaining the increase to 2.6 g/cm^3 that was observed. This confirms that the density of a B_4C layer increases when grown with ion assistance, namely by 13%.

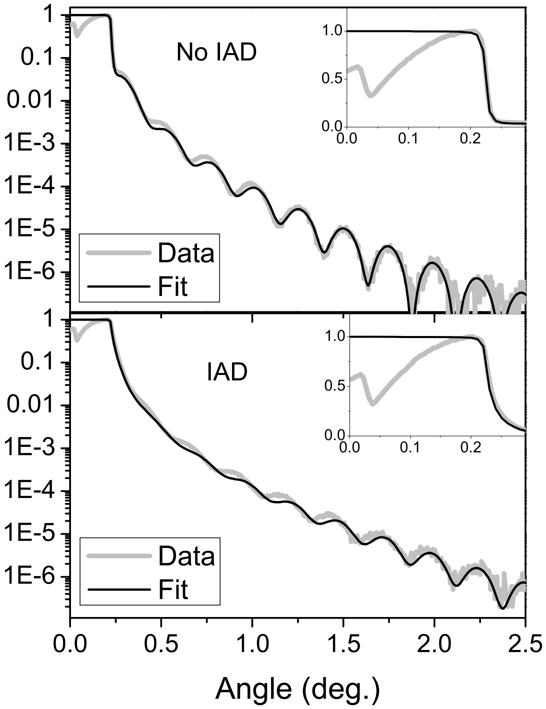

Figure 6.3: GIXR reflective curves of B_4C single layer films grown with (bottom) and without (top) ion assistance (IAD). The measured data is indicated by the thick grey line and the fit by a thin black line. The insets show the critical angle at a linear scale.

6.3.4 Partial treatments

To separate the effects of increased density from those of improved chemical stability at the interfaces, multilayers with treatment of only a part of the B_4C layer were produced, allowing us to probe the depth dependence of the effect. Since no difference was observed in the effect of treating B_4C-on-Si or B_4C-on-Mo (section 6.3.2), the partial ion treatment was performed on both interfaces simultaneously. Multilayers with ion treatment during the first 25%, 50% and 75% of B_4C deposition were selected, and thermally annealed at 200°C. Figure 6.4 shows a clear trend that the multilayers become more stable when a larger fraction of the layer is treated.

To quantify the improved stability, due to the increased fraction of B_4C treatment, the diffusion coefficients were determined from the data in figure 6.4, using the method described in chapter 5. These coefficients are presented in figure 6.5, where a clear linear dependence is observed in the diffusion coefficient plot versus the fraction of the treated B_4C layer. The ions had a penetration depth of approximately 0.75 nm (derived from TRIM calculations to be discussed hereafter) while the

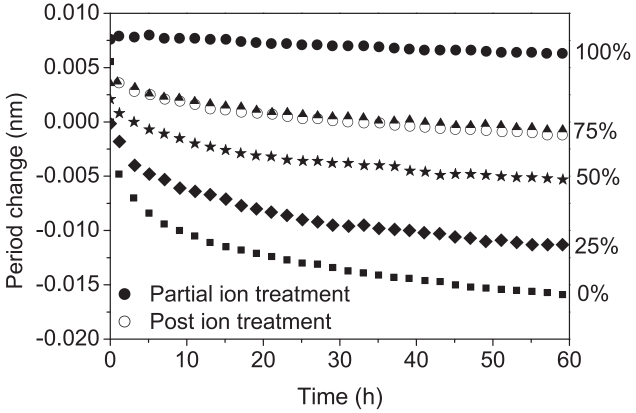

Figure 6.4: Period change as a function of annealing time at 200°C for multilayers fabricated applying ion treatment for a percentage of the barrier layer growth. The solid symbols represent data for multilayers of which the initial parts, ranging from 0 to 100%, of the B_4C layers were treated using ions. The open symbols denote the data for post-deposition treatment of the B_4C layer growth. Each symbol denotes an average of 10 data points, the statistical error of the data points is 0.5 pm.

treatment was started from the beginning of the layer growth. If enhanced chemical stability would be the main cause for the stabilization effect observed, the largest effect would be observed when only 25% of the layer was treated. The difference between the 75% and 100% cases would in this case be negligible, since the interface is not reached by ions during the growth of the last quarter of the layer.

As a result of the ion-induced density increase, the denser part of the layer will have more effective diffusion barrier properties, and correspondingly a lower diffusion coefficient. Since all B_4C layers are equally thick, the diffusion coefficient, D, of the partially treated B_4C layers can be approximated as the weighted average (i.e. $fD_{IAD} + (f-1)D_{No-IAD}$, where f is the fraction of the layer which is treated by ions) of the diffusion coefficients with full treatment and without treatment. This is similar to the case of Hart's equation [91], where the diffusion coefficient through a material with small crystallites is approximated by a weighted average of the diffusion coefficients through the crystals and the amorphous material between the crystals. The linear trend observed in figure 6.5 is in agreement with such a weighted average over the diffusion coefficients of the ion treated and not ion treated parts of the B_4C layer.

To check the effect of the ion penetration depth, a particular multilayer was studied in which only a post deposition treatment by Kr^+ ions for a period of 30 s was performed on the barrier layers using the same ion flux and energy as during the full layer IAD treatment procedure. This 30 s duration was chosen because it results in an ion to atom ratio of approximately 1:1, similar to the IAD case. The data in fig-

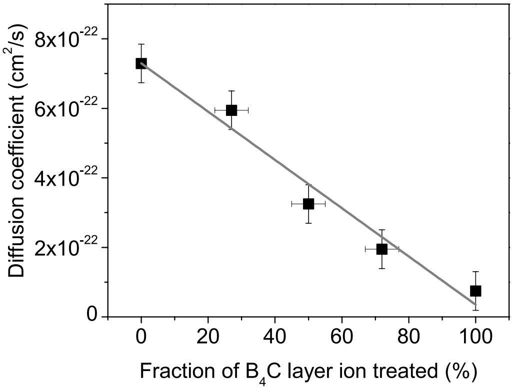

Figure 6.5: The diffusion coefficient plotted against the percentage of the layer treated by ions.

ure 6.4 shows that this multilayer has the same thermal stability as the 75% partial IAD sample. To explain this we did TRIM calculations [92], which showed that the average penetration depth in B_4C of Kr^+ ions with an energy of 80 eV and an incidence angle of 45° ranges between 0.7 and 0.8 nm depending on the B_4C density (values between 2.3 and 2.6 g/cm^3). This means that in the case of ion treatment after deposition of the B_4C layer, effectively the top 70-80% of the B_4C layer was densified, and that the ions did not penetrate to the B_4C-on-Mo and B_4C-on-Si interfaces. The results of treatment of the top $\sim$75% of the B_4C layer thus matched well with the results of the treatment of the initial 75% of the B_4C layer, confirming that the increased thermal stability resulting from ion assisted deposition of the B_4C layer is a 'bulk' density enhancement effect.

6.4 Conclusions

We observed a significant improvement in the thermal stability of B_4C diffusion barriers in Mo/Si multilayer structures when they were treated with 80 eV Kr^+ ions during deposition (IAD). We showed that the thermal annealing results are invariant to the interface type treated, being either the B_4C-on-Si or the B_4C-on-Mo interface. This observation basically rules out chemical causes for the enhanced stability, because they are argued to be different for both types of interfaces. Secondly, we observed that the interface diffusion coefficient was linearly dependent on the percentage of the layer treated, independent of the growth stage where the treatment took place: either at the conclusion of the deposition of the layer or at its initial growth stage. These findings clearly show that it is the ion-induced increase in the B_4C layer density that is the reason for the enhanced thermal stability observed.

Chapter 7

Damage mechanisms of MoN/SiN multilayer optics for next-generation pulsed XUV light sources

Abstract

We investigated the damage mechanism of MoN/SiN multilayer XUV optics under two extreme conditions: thermal annealing and irradiation with single shot intense XUV pulses from the free-electron laser facility in Hamburg - FLASH. The damage was studied ”post-mortem” by means of X-ray diffraction, interference-polarizing optical microscopy, atomic force microscopy, and scanning transmission electron microscopy. Although the timescale of the damage processes and the damage threshold temperatures were different (in the case of annealing it was the dissociation temperature of Mo_2N and in the case of XUV radiation it was the melting temperature of MoN) the main damage mechanism is very similar: molecular dissociation and the formation of N_2, leading to bubbles inside the multilayer structure.

7.1 Introduction

The rapid development of a new generation of extreme ultraviolet (XUV) radiation sources providing ultra-short (from atto- to nanoseconds) pulses creates new challenges for optics. Instruments like free-electron lasers (FELS) [25, 93, 94], higher harmonic generating sources (HHG) [95, 96], high-energy coherent sources based on laser plasmas [97], and capillary discharge lasers [98] produce pulses of very high intensity which may induce radiation damage in optical coatings. Two damage mechanisms are of special importance: (a) permanent damage of the coatings due to structural changes and (b) change of the optical properties of materials under high intensity XUV irradiation. They are new compared to the ones observed in the previous generation of light sources, like plasma sources used in lithography or synchrotrons. Both mechanisms may be a limiting factor for many scientific and industrial applications. Therefore, for a proper design of optics for current and future XUV light sources, it is crucial to understand the physical mechanisms leading to radiation damage.

It is especially important for multilayer coated mirrors where, at the resonant angle, the absorbed energy density is the highest. They are widely used in ”front-line” experiments like XUV time resolved holography as a part of the imaging system [23], as diffraction limited XUV beam focusing optics for warm dense matter creation [99, 100] and as a part of the delay line for one colour pump and probe studies on XUV transmission of solids [101]. Recently, the single shot damage mechanism in one type of these optical coatings - the Mo/Si multilayer - was studied [27, 102] at the FLASH (Free-electron LASer in Hamburg) facility (providing fs XUV pulses) and using an XUV plasma source at the Laser Lab Goettingen, Germany (with ns pulse duration). Melting of amorphous Si layers followed by diffusion of Mo atoms into the molten Si and subsequent molybdenum silicide formation proved to be the leading damage mechanism in these multilayers. To block this damage processes, one should use materials with high melting points and with low diffusion constants, preventing intermixing of the layers. These conditions are fulfilled by MoN/SiN multilayers. The melting temperatures of the individual layers are higher than that of silicon. Moreover, below the temperature that one of the compounds melts, the atomic diffusion coefficient in MoN/SiN multilayers is 11 orders of magnitude lower than in Mo/Si multilayers [32].

The goal of this chapter is to determine the damage threshold and the damage mechanism for MoN/SiN multilayers exposed to an intense ultra-short pulse of XUV radiation. The results are compared to the damage caused by thermal annealing of the multilayers.

7.2 Experimental

The MoN/SiN multilayer coatings used in this work have been deposited on superpolished Si substrates using e-beam evaporation of Mo atoms and magnetron sputtering of Si atoms in a UHV background of 1×10^{-8} mbar, with post-deposition smoothing using low energy ion treatment of the Si layers [64, 103–105]. Nitridation of the Mo and Si layers was achieved by low energy nitrogen ion treatment during deposition [106–108]. X-ray photo-electron spectroscopy (XPS) was used to qualify the nitridation process. E-beam deposition of Mo layers was selected due to the higher quality nitride. XPS showed atomic concentration ratios between Mo and N and Si and N that were both equal to 1 ± 0.1, signifying MoN and SiN formation. Since the most common stoichiometry for silicon nitride is Si_3N_4, the nitridation of the Si was not saturated.

The as-deposited samples were further characterized by means of hard X-ray ($\lambda =$ 0.15406 nm) and XUV reflectometry. The first technique provides information on the layered structure, including layer thicknesses and multilayer period. The latter technique determines the multilayer performance, i.e. the angular resolved reflectivity of the multilayer for s-polarized light at 13.5 nm for low (non-destructive) irradiation intensities. From these measurements the performance of the multilayer for any polarization and angle can then be predicted by means of simulations with the software package IMD [61]. The multilayers consisted of 40 bilayers of MoN and SiN, with a periodicity of 8.18 nm and a MoN layer thickness of 40% of the total thickness. The resonant angle and maximum reflectance for 90% s-polarized light were determined to be 27 degrees off-normal incidence and 26.5%, respectively (see figure 7.1).

The sample was irradiated at the FLASH facility in Hamburg, Germany [25, 26]. The radiation wavelength was 13.45 ± 0.05 nm and the XUV pulse duration was in the order of 10 fs (FWHM). The sample was aligned at resonant angle with respect to the incident photon beam which was p-polarized. Since the pulse energy fluctuated from pulse to pulse in the range of 0.01-1 μJ it was measured with a gas monitor detector [109]. The radiation was focused with a grazing incidence carbon-coated ellipsoidal mirror with a focal length of 2 m. The footprint of the beam on the sample had an area at 1/e intensity level of 66 ± 3 μm^2. To obtain a Gaussian beam shape, a 3 mm diameter circular aperture in front of the focusing mirror was used. Most of the experiments were performed in ”high intensity” mode, with the sample in the focus of the beam. For the given energy fluctuation, this mode corresponded to a beam fluence range of 15 - 1500 mJ/cm^2. In addition, for the purpose of reflectance studies, measurements at lower intensities were performed with the sample placed $\sim$70 mm out of focus, corresponding to a $\sim$ 15000 μm^2 footprint area at 1/e intensity level and a fluence range of approximately 0.05-5 mJ/cm^2 for the same energy range. The sample was irradiated in single shot mode, i.e. after each irradiation the sample was moved and was irradiated at an unperturbed position. The reflected radiation intensity was measured with a photodiode [27].

After exposing the MoN/SiN sample to the XUV pulses, the irradiated spots were investigated with different techniques: optical microscopy with differential interference contrast - DIC (with a Nomarski prism) sensitive to changes of the morphology and optical properties of the materials, atomic force microscopy (AFM) providing a 2D depth map, scanning electron microscopy (SEM) showing the morphology of irradiated spots, and cross-sectional scanning transmission electron microscopy (STEM) to analyze the structural changes below the irradiated surface.

In order to get better insight in the thermal behaviour of the MoN/SiN multilayer, a sample from the same coating run was sequentially thermally annealed at 3 different temperatures. The sample was heated to 500°C, 700°C and 900°C in a vacuum furnace ($< 10^{-5}$ mbar). In each step the sample was annealed for a period of 30 minutes. In order to investigate the structure of the layers, the samples were characterized at each temperature with wide angle X-ray diffraction (WAXRD) and grazing incidence X-ray reflection (GIXR). In case of the sample annealed at the highest temperature the surface morphology and internal structure were investigated by means of AFM and STEM scans respectively.

7.3 Results

7.3.1 Reflectometry

XUV reflectivity measurements were carried out using 13.5 nm radiation in three different intensity regimes. The reflectivity at low-intensity (well below the expected damage threshold) was measured at the Center for X-Ray Optics (CXRO) at Berkeley, USA, using 90% s-polarized radiation from the Advance Light Source (ALS), for angles ranging from $10^\circ - 50^\circ$ off-normal. These measured values were transformed to p-polarized radiation by means of IMD [61] simulations. The reflectivity curve and the IMD simulation for 90% s-polarized light as well as the results for p-polarized light are shown in figure 7.1. The reflectivity measurements at middle and high intensities were performed at FLASH at $28.2 \pm 0.3^\circ$ off-normal. The reflectivity of p-polarized radiation at this angle is shown in table 7.1 for all three intensity regimes. The reflectivity is constant, within the error-bars, over the entire intensity-range investigated, i.e. from 100 W/cm^2 to approximately 5×10^{13} W/cm^2, which corresponds to fluences up to 500 mJ/cm^2. This indicates that the damage caused by high intensity femtosecond pulses is not affecting the reflection during the pulse itself and occurs on timescales longer than the pulse duration. This is in agreement with theoretical models [110], where significant change of the optical properties of femtosecond duration pulses is predicted only for fluences above 20 J/cm^2.

Table 7.1: Reflectivity of a MoN/SiN multilayer, at $28.2\pm0.3^\circ$ off-normal incidence for 13.5 nm p-polarized radiation.

Facility	Mean intensity (W/cm^2)	Reflectivity (%)
LS at CXRO	1×10^2	7.7 ± 1.0
FLASH (low-intensity regime)	1×10^{11}	7.0 ± 0.2
FLASH (high-intensity regime)	5×10^{13}	6.9 ± 0.3

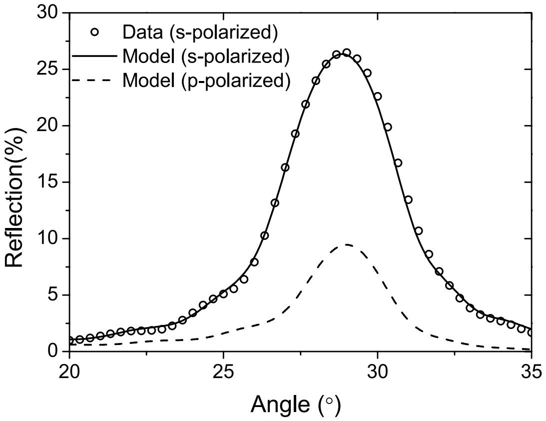

Figure 7.1: Reflectivity curve for 90% s-polarized light (λ = 13.5 nm), including a model simulation using IMD. Applying the same model, the expected reflectivity for p-polarized radiation has been calculated.

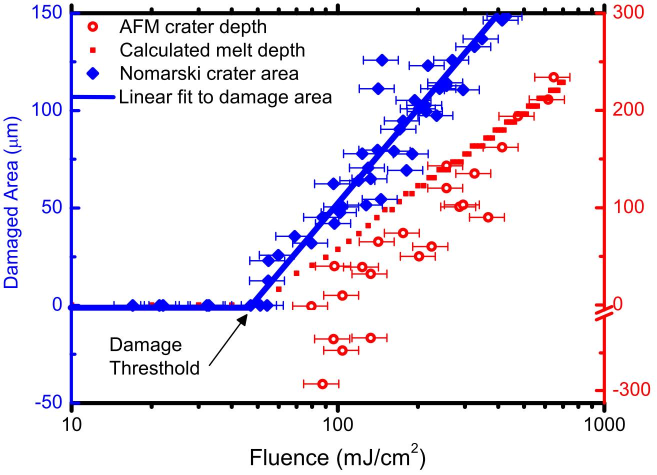

Figure 7.2: Dependency of the damaged area/depth on the incident beam fluence. The damaged area (blue solid diamonds) was measured by DIC microscopy while the depth of the craters (open red circles) was determined by AFM. The negative values of the AFM correspond to the height of the hills; the depth-axis has been compressed for the negative values. The calculated melt depth (red squares) corresponds to the melting of MoN layers, assuming an averaging of the temperature over each bilayer shortly after energy deposition (see text for details).

7.3.2 Optical microscopy with differential interference contrast

Of each irradiated spot an image was made with a DIC optical microscope. For the purpose of the initial analysis, the damage was defined as the radiation-induced surface changes observable in the image. In figure 7.2 the damaged area is plotted as a function of the logarithm of the pulse energy (blue markers). The single shot damage threshold, which is determined [111, 112] from the intersection of the line fitted to the experimental data points with the x-axis, is equal to 48 ± 7 mJ/cm^2.

7.3.3 Atomic force microscopy

The morphology of the MoN/SiN multilayer surface after irradiation was further investigated with AFM. Example pictures of three types of observed damage are shown

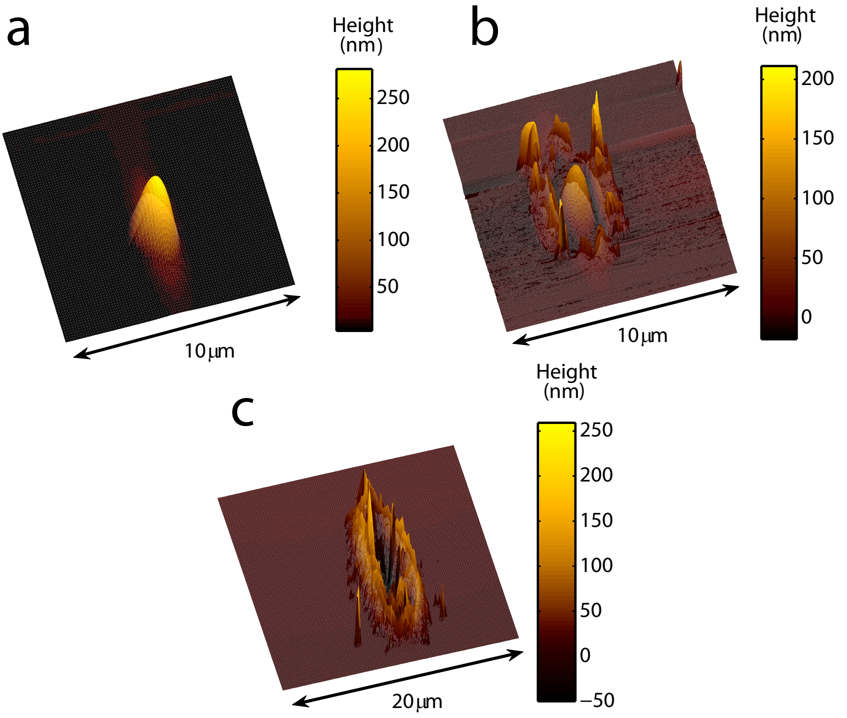

Figure 7.3: AFM images illustrating the characteristic surface morphology of the multilayer irradiated at three fluence regimes. Just above the damage threshold we observe a smooth hill (a). At intermediate fluences a hill and a crater with side walls can be observed (b). At high fluences, only a crater with high side walls is observed (c).

in figure 7.3(a-c). At low fluences, from the damage threshold up to approximately 100 mJ/cm^2, smooth hills are formed (a). The heights of these hills were between 1 nm and 200 nm. For fluences above 140 mJ/cm^2, a crater is formed which is surrounded by side walls (c). Both the depth of the crater and the dimensions of the wall increase with increasing fluence. The crater's depth varies between 50 nm and 250 nm while the walls height ranges between 40 and 400 nm with an approximately constant width of 1.5 μm. In contrast to the very smooth surface of the hill in the first stages of damage, the wall structure is very rough. In some of the irradiated spots a small hill of about 10 nm height is observed at the bottom of the crater. In an intermediate intensity region, for fluences between 100 and 140 mJ/cm^2 the damage spot consists of a large hill ($>$100 nm), which is surrounded by a small side wall (b).

The fluence dependency of the depth of the craters and the height of the hills (negative values) is plotted in figure 7.2. In case of the spots from the intermediate intensity regime, both the depth of the crater and the height of the hills are presented. The damage threshold was calculated similarly as for optical microscopy. In case of the AFM data it is equal to 80 ± 13 mJ/cm^2, which is higher than the value obtained from the DIC microscopy data. This difference will be addressed in section 7.3.5

7.3.4 Scanning electron microscopy and scanning transmission electron microscopy

One of the spots, exposed to a fluence of 141 mJ/cm^2 (the same as presented in figure 7.3c), was further studied by scanning electron microscopy. The SEM image (figure 7.4) shows that on the edge of the crater many semidetached layers are stacked over each other. They form the wall observed in the AFM map in figure 7.3c. The STEM technique was used to analyze the structural changes below that crater. A thin tungsten layer was deposited on the crater area as a protective layer (and can be seen in figure 7.5a as a black layer on top of the multilayered structure). Next, a 60 nm thin cross-section along the white line marked in the SEM picture (figure 7.4), was made by means of a focused ion beam (FIB). For high resolution images this slab was thinned by low energy argon ion beam polishing. STEM images at different positions with respect to the crater borders were registered with variable magnifications. The results are shown in figure 7.5.

In figure 7.5a an overview image of the crater is shown. The undamaged part of the multilayer can be seen at the bottom of the figure. Above this area we observe structures consisting of pillars of peeled off layers with holes in between (white areas). There is a sharp boundary between the undamaged multilayer and the area where the layers have been peeled off. In figure 7.5b a magnified area of one of the pillars is presented. Due to the transversal distribution of the pulse intensity, the absorbed energy density increases from left to right in the picture. At the lowest fluence, at the location indicated by arrow I in figure 7.5b, no damage can be observed. At increased fluences, (at location II) new features appear: light areas in the dark MoN layer. Since STEM was used in the bright mode, the white areas indicate that the layer has crystallized. In addition to the crystallization, the MoN layer also expands. The expansion continues until the MoN layer completely delaminates from

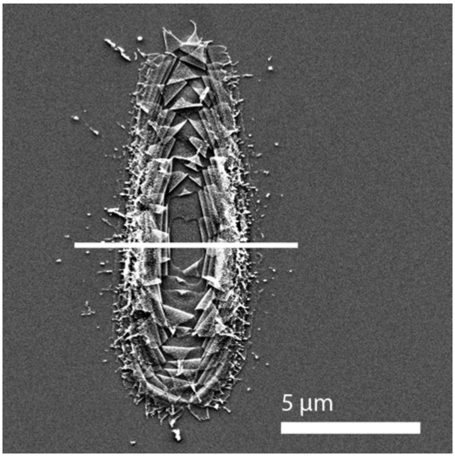

Figure 7.4: SEM picture of the crater created by irradiation with a fluence of 141 mJ/cm^2. The crater is surrounded by partially detached layers positioned over each other. The white line indicates the location for the cross-section STEM pictures in figure 7.5.

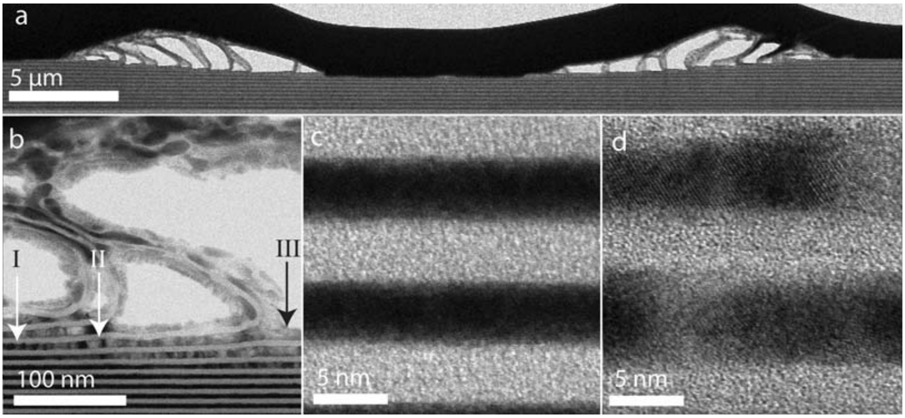

Figure 7.5: STEM images of the sample cross-section below the irradiated spot: (a) an overview of the crater, (b) magnified image of one of the pillars, (c) and (d) magnified images of the undamaged and the first stages of damage, respectively. The darker areas correspond to MoN and the lighter areas correspond to SiN. On image (b) three regions are marked (see text for details).

the underlying multilayer, which can be seen at location III. Magnified images of the multilayer far away from the crater and in close proximity of the crater are shown on figure 7.5c and figure 7.5d, respectively. The crystallization and expansion of the MoN near the crater can be clearly seen in this comparison. In contrast to the changes observed in the MoN layers after exposure, the SiN layer appears to stay intact and forms pillars in between the holes.

7.3.5 Modeling of molten volume

To further explore the mechanisms responsible for the damage, we addressed the thermal aspects directly after exposure. We estimated the fluence dependent number of the melted MoN layers. The calculations consist of 3 steps. In the first one the depth profile of the energy deposited (absorbed radiation) in the multilayer is calculated. Next it is assumed (in a simplified model) that the heat transfer leads to a temperature equalization over each bilayer. The corresponding temperature profile can be calculated based on the deposited energy density and material constants. The temperature profile is then compared to the melting temperature of the MoN layer and the melted depth (number of bilayers in which MoN is melted) is calculated.

Due to the radiation absorption, energy is deposited in the multilayer. The optical flux absorbed at a given depth is proportional to the product of the local field intensity, the real part of the refractive index, and the absorption coefficient. The field intensity can be calculated using IMD software for a given multilayer structure model and radiation fluence. The optical constants can also be obtained from IMD. As a result the depth profile of the absorbed energy density can be obtained as a function of the radiation fluence.

Because of a non-uniform energy absorption in the multilayer, the initial temperature is unequally distributed over the bilayers, with maxima in the MoN layers. However, due to strong temperature gradients and heat exchange between the layers, the temperature profile gets smoothened very rapidly. This process is much faster than the heat dissipation to the substrate, due to a much higher temperature gradient. Therefore, it may be considered that shortly after the pulse the temperature is approximately constant over the entire bilayer. The corresponding temperature profile can be calculated from the deposited energy density (averaged over each bilayer) and thermodynamical properties of the materials. Since the thermodynamic constants of SiN and MoN are unknown, the enthalpy of SiN is approximated by the one of Si_3N_4. The enthalpy per MoN molecule is approximated by the enthalpy of only the molybdenum atoms. The contributions of the nitrogen atoms and the atomic interactions are neglected. Since nitrogen atoms are much lighter than Mo atoms, such an approximation seems to be valid, although it may lead to an overestimation of the temperature in the MoN layers.

The calculated temperature can be compared with the melting temperature of each material - the melting temperatures of both MoN and Si_3N_4 are known from literature [79] to be 1750°C and 1900°C respectively. The layers whose temperature rises above that threshold are considered to melt after irradiation.

From the above described model, the number of molten MoN layers can be calculated. In figure 7.2 we present the position of the deepest molten MoN layer (red solid squares). The depth of the craters as measured by AFM can be correlated (see figure 7.2) to the number of molten MoN layers (assuming delamination of all the molten layers). The data correspond to each other for fluences above 300 mJ/cm^2. For lower fluences the AFM measured crater depths are lower than the calculated molten depths. This difference can be partly explained by an underestimation of the crater depth for low fluences caused by the hills observed in the centre of the crater. Moreover, the STEM data show that one or two layers below the crater do not delaminate and only crystallites are formed within them after irradiation. However, the DIC technique is sensitive not only to morphological changes of the material (as AFM) but also structural ones, including formation of the crystallized MoN layer. The damage threshold found from the optical microscopic studies is approximately the same as the melting threshold resulting from the simulations.

7.3.6 Thermal annealing

In order to obtain a better understanding of the thermal behaviour of MoN/SiN multilayers we have sequentially annealed the MoN/SiN multilayer at three different temperatures, 500°C, 700°C and 900°C for 30 minutes. After each exposure the crystallinity and the period of the multilayer were determined by WAXRD and GIXR respectively, at a wavelength of 0.15406 nm; the measurement geometries are discussed is section 2.3.3 and 2.3.2. From the GIXR spectra, the period of the multilayer at each annealing step was determined by fitting the Bragg peak positions with the modified Bragg law (equation 2.3). From the as-deposited state to the state upon annealing to 500°C the period increased by 0.09 nm, which is attributed to expansion in the SiN layer. In the next step, annealing to 700°C, the period did not change. At 900°C the GIXR spectrum did not provide an accurate measure of the period anymore, the reason for this will be discussed below.

The results of the WAXRD measurements are shown in figure 7.6, the diffraction pattern of the reference spectrum is identified as tetragonal Mo_2N [*], as indicated with the dotted lines and the Miller indices on the top of the graph. Apparently, already at room temperature, randomly orientated polycrystalline Mo_2N crystallizes inside the layer. Since the deposited ratio between Mo and N is 1:1, the excess of N must be incorporated in the uncrystallized part of the layer or diffuse towards the SiN layer. During annealing to 500°C the WAXRD peaks become sharper, and all the peaks shift to higher angles. The sharper peaks indicate an increase in crystallite size [58], the peak shifts are caused by an isotropic contraction of the lattice parameters. In the next step, annealing to 700°C, the WAXRD spectrum does not change significantly, except for a small shift of the (111) peak. At 900°C, the spectrum shows two additional peaks and a large change in the (111) peak. The two new peaks, at 95° and 99°, can be attributed to cubic Mo_2N[†]. The reference peak positions of this crystalline phase are indicated with dashed lines and Miller

---

[*] β-Mo_2N, PDF card number 25-1366

[†] δ-Mo_2N, PDF card number 25-1368

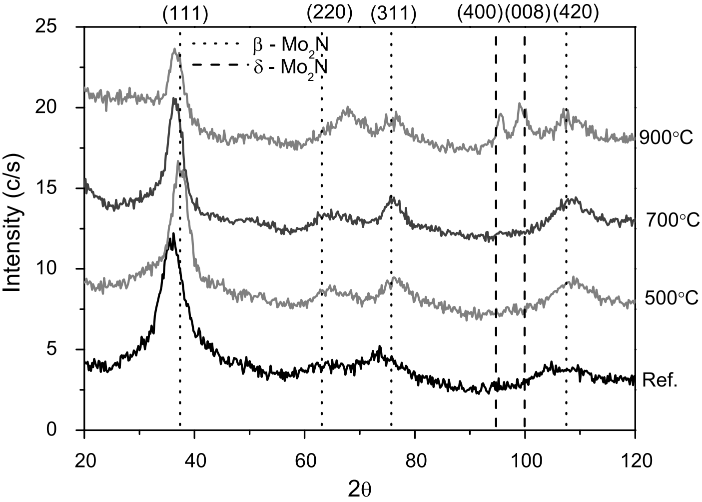

Figure 7.6: XRD spectra from a MoN/SiN multilayer taken before annealing, and after annealing at 500°C, 700°C, and 900°C. Every dataset is plotted with an offset of 5 counts for clarity.

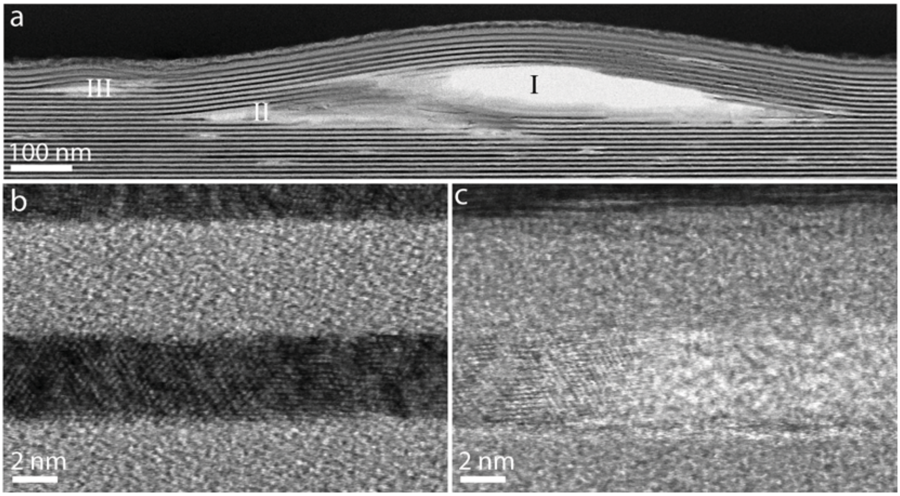

Figure 7.7: STEM images of the multilayer annealed to 900°C. (a) Example of three bubbles, marked with I-III. (b) Magnified image of the highly ordered crystalline structure present in most of the MoN layers. (c) Magnified image of an amorphous, low density, structure that can be found at various locations in the MoN layers.

indices as well. The peak shift of the (111) peak at 700°C can be attributed to the start of the transformation to δ-Mo_2N.

After annealing to 900°C, AFM investigations showed the formation of hills all over the multilayer surface, which were not present at 500°C and 700°C. The hills vary in height from 6 to 70 nm and in width at their base from 0.2 to 1 μm. Further cross-sectional STEM was performed on the multilayer annealed at 900°C. In figure 7.7a it is shown that the hills are caused by bubble formation inside the multilayer (I-III). Apart from the bubbles, structural changes are also observed inside the MoN layers, one of which is magnified in figure 7.7c. They are amorphous and, since they appear very light in the STEM picture, have a lower density. Most likely these are the onset of the formation of bubbles. At all the other positions in the MoN layers we observe highly ordered crystallites (figure 7.7b).

7.4 Discussion

The MoN/SiN multilayer was exposed to two different extreme conditions: thermal annealing and single shot fs-XUV laser pulse irradiation at the FLASH facility. Although the main parameters of the exposures (timing, temperature and lateral distribution of the absorbed heat) were completely different, similarities in the mechanisms responsible for damage in the multilayer were observed. In both cases crystallization of the MoN layer and the formation of bubbles in the MoN layer are the main cause of damage.

The as-deposited state of the MoN layers in the studied samples is mostly an amorphous mix of Mo and N atoms in a ratio of 1:1. In between the MoN a small amount of β-Mo_2N crystals have formed. When the temperature was raised during annealing, the WAXRD spectra showed that the Mo_2N crystallites increase in size. At 900°C the pattern of δ-Mo_2N appears and the AFM and STEM results reveal bubble formation in the structure. The Gibbs free energy of Mo_2N formation in the reaction $2\text{Mo(s)} + \frac{1}{2}\text{N}_2 \rightleftarrows \text{Mo}_2\text{N}$ for an N_2 pressure of 1 bar can be written as [113]:

$$\Delta G^0_{Mo_2N} = -57320 + 53.89T \tag{7.1}$$

where $\Delta G^0_{Mo_2N}$ is expressed in J/mol and T is the temperature in Kelvin. Mo_2N formation is energetically favourable up to the (dissociation) temperature of 790°C [79]. This temperature can increase with increasing pressure or concentration of N_2 [113, 114]. In the annealing experiment at 500°C and 700°C, below the dissociation temperature, Mo_2N crystals are formed. After annealing to 900°C, well above the dissociation temperature, the Mo_2N crystallites start to dissociate into Mo and N_2 gas. This process saturates due to the increase of the nitrogen concentration. However, as observed in the STEM images, at some positions the dissociation process leads to formation of volumes of clearly lower density due to a small amount of released N_2 gas. They are the onsets of the bubble formation. At some of them, where there is a "weak point" in the multilayer structure, the MoN layer breaks apart and the SiN layers delaminate, which leads to the formation of bubbles. The development of a bubble decreases the N_2 concentration and more gas can be released due to further dissociation.

In the case of FLASH, we do not observe any damage or significant crystallization below the melting point of MoN. Atoms simply do not have enough mobility in the solid phase and can not move over significant distances in the short period that the irradiated area is at an enhanced temperature (it can be assumed that the heat conductance to the Si substrate cools the sample down to room temperature in a time shorter than 1 μs). Above the melting point of MoN, atoms are much more mobile in the liquid MoN phase. STEM images show that crystals are formed at the edge of the melted area and bubbles develop closer to the surface. In line with the annealing results, it is likely that the Mo_2N crystals are formed and N_2 gas is released what leads to bubble formation. However, at the temperatures and multilayer composition used in this study, the phase diagram is not well known [113]. Therefore the mechanisms of the formation of the N_2 bubbles and the Mo_2N crystals inside the MoN layers can not be determined with absolute certainty. We propose two different models here. The common starting point for both of them is melting of the MoN layer followed by heat dissipation to the substrate and layer solidification.

In the first model we presume that during solidification of MoN the temperature is above the dissociation temperature and therefore Mo_2N can not form, only solid Mo and N_2 gas. At the edge of the molten volume, the heat dissipation is faster due to the direct thermal contact with cooler layers below. Therefore an under-cooled liquid may form at the edges of the damaged volume. The temperature of this under-cooled liquid can drop below the dissociation temperature of Mo_2N (which can be enhanced due to high nitrogen concentrations). Thus, the thermodynamically favourable, Mo_2N crystals will form there.

In the second model we presume that the dissociation of Mo_2N can not occur due to the very high concentration of nitrogen, higher than the eutectic concentration. Due to the difference in stoichiometry between the Mo_2N crystals and the molten MoN phase the extra nitrogen must be released. Since the solvability of the nitrogen in liquid MoN is much higher than in Mo_2N, the N_2 is pushed away from crystals and dissolves in the liquid. Thus in the final state, after cooling, there are Mo_2N crystals surrounded by gaseous N_2. The more time the solidification process takes, the bigger crystals are formed (in figure 7.5b the crystal size increases with increasing initial temperature). At the same time the concentration of N_2 in the liquid increases which results in higher pressure in the bubbles after the solidification process ends. Since the main direction of the heat dissipation is towards the substrate, the deeper layers need less time to solidify, which explains the formation of small crystals below the crater (see figure 7.5b).

In both models, at the final state, the SiN layers have delaminated due to release of N_2 gas. At fluences just above the damage threshold, the SiN layer stays intact on top of the bubble (figure 7.3. At higher fluences, more N_2 is released, therefore the pressure on the SiN layers becomes too high and the bubble 'burst' and the SiN layers fall back on the substrate (figure 7.3c and figure 7.4).

Finally we compare the results for MoN/SiN multilayers to those of Mo/Si multilayers. It is remarkable that for the MoN/SiN structure of the multilayer the damage threshold (48±7 mJ/cm^2) is almost the same as tor the Mo/Si multilayer (45±7 mJ/cm^2), reported earlier [27]. This is partly related to the optical properties of both coatings. The reflectivity of the Mo/Si multilayer is $42 \pm 1\%$, while the reflectance of the MoN/SiN multilayer is $7 \pm 1\%$. The lower reflectance leads to enhanced absorption in the presently studied case, which causes the temperatures in the materials to be higher. Therefore, the increased melting temperature of MoN and SiN compared to the one of Si is not sufficient to increase the damage threshold. On the other hand, the decreased atomic diffusivity [32] in the studied sample below the melting temperature increased the critical temperature in the annealing experiment, compared to the Mo/Si multilayer. Concluding, compared to Mo/Si multilayers the MoN/SiN coatings are expected to have a higher temperature robustness for slow heating and a similar single shot damage threshold in terms of laser energy.

7.5 Summary and conclusions

We have investigated the damage mechanism of MoN/SiN multilayers resulting from two potential damage processes: continuous thermal annealing and single shot irradiation with femtosecond XUV pulses at the FLASH facility. In the case of thermal annealing, the formation of Mo_2N crystals in the MoN layer occurs below 790°C. Above this temperature, the MoN layer dissociates into Mo and gaseous N_2 which agglomerates in the form of bubbles in the multilayer materials. In case of the XUV laser irradiations, permanent damage of the multilayer occurs on a much longer timescale than the pulse duration, and consequently does not affect the reflection process within the pulse. The single-shot damage threshold of the multilayer is determined to be 48 ± 7 mJ/cm^2. At this fluence the MoN layer reaches the melting temperature. ”Post-mortem” studies of the multilayer show that crystals form at the edge of the melted area and bubbles develop closer to the multilayer surface. Since the thermodynamical data are not available for the atomic concentrations and temperatures studied, we propose two possible models describing the XUV damage process. Both lead to the release of the excess N_2, which forms bubbles in the multilayer structure, but they differ by the role of the dissociation process. In the first model MoN decomposition is the key process and in the second decomposition is blocked by the saturating nitrogen concentration, but due to the difference in stoichiometry between the Mo_2N crystals and the molten MoN phase the extra nitrogen must be released.

Although the main parameters of the exposure (timing, temperature and lateral distribution of the heating) were completely different, the main damage mechanism is very similar: crystallization to Mo_2N and outgassing of N_2, leading to bubble formation inside the multilayer structure. However, the timescale of the damage processes (less than 1 microsecond vs. hours, for pulsed and continues annealing, respectively) and the damage threshold temperatures (approximately 1750°C vs. 790°C) are different. This is caused by the difference in the atom mobility in the solid and liquid phases, which changes by many orders of magnitude when crossing the melting point.

The results show that MoN/SiN multilayer optics can be used at femtosecond XUV light sources for fluences up to 48 ± 7 mJ/cm^2 under the condition that the repetition rate of the source allows the deposited heat to dissipate between subsequent pulses. The nature of the damage mechanism (melting of the MoN layer and releases of gaseous nitrogen) allows for extrapolation of the results for other 4$^{\text{th}}$ generation light sources with pulses longer than those of FLASH. In the previously studied Mo/Si multilayers the damage threshold was determined by melting of the Si layers. The melting temperature of MoN is much higher than that of Si, but the observed damage threshold of MoN/SiN multilayers is similar to the damage threshold of the Mo/Si multilayers. This is caused by increased absorption, and therefore enhanced temperatures in the MoN/SiN multilayers. However, the MoN/SiN multilayers are more suitable for slow heating at extended temperatures compared to the Mo/Si case (below the dissociation temperature).

Chapter 8

Valorization and outlook

8.1 Application of multilayer optics

In the past decade, thin single and multilayered films have become an integral part of many state-of-the-art analytical and imaging instruments using short wavelength radiation. One such an application, which recently receives large interest from the semiconductor industry, is the use of multilayer systems as reflective coatings for optical elements in photo projection lithography. Lithography equipment in general is used to produce the integrated circuits that have become common in all electronic devices currently used throughout our society. Manufacturers strive to develop faster, more powerful, and smaller devices with reduced power consumption, presenting huge challenges for the field of semiconductor manufacturing. The last decades the developments in this field have been very rapid and shrinkage of transistor size can be described by Moore's law* which states that the number of transistors per unit area in integrated circuits doubles every 18 months. For the 18 nm half-pitch node, industry now most likely is going to switch to EUV lithography in 2012 [115, 116], requiring the development of high reflectance multilayer coatings and controlling coating lifetime to meet the high requirements. Understanding possible thermal damage is a major aspect of this.

The work described in this thesis is part of the research programme eXtreme UV Multilayer Optics, or 'XMO'. XMO is an Industrial Partnership Programme which is jointly financed by the 'Stichting voor Fundementeel Onderzoek der Materie' (FOM) and by Carl Zeiss SMT GmbH in Oberkochen, Germany. Carl Zeiss has a long tradition in developing the high-performance optical systems for the lithography equipment produced by ASML. In the past years, Carl Zeiss has initiated an R&D pro-

---

[*] It could be argued that Moore's law is not a 'law' but a roadmap guide or even a self fulfilling prophecy, which industry uses as a guideline for how fast they need to develop integrated circuits and related instrumentation processes.

gramme on EUVL optics, and has chosen FOM as a partner in the multilayer research activities. The program consists of fundamental research on layer growth, roughness development and new multilayer designs. The success of this project, symbolized by a world record on EUV reflectivity of 70.3% [84], and the need for continued research on lifetime aspects recently lead to a new IPP programme called 'Controlling photon and plasma induced processes at EUV optical surfaces', or CP3E, which is carried out together with both ASML and Carl Zeiss, with base funding by Carl Zeiss and FOM.

Multilayer optics can also be used in many other short wavelength applications, like free electron lasers or space telescopes [11]. These applications, together with EUVL, critically require that the optical properties of the multilayer coating will not change over long periods of time, either through high intensity and/or prolonged exposure to radiation. In addition, the high cost of the high accuracy optics for these short wavelengths necessitates a prolonged period of faithful operation.

8.2 Thermal stability of multilayers

One of the main threats to multilayer optics lifetime is thermal damage. At power loads well below those leading to crystallization or even melting of the layer materials, thermal damage in the multilayer structure readily occurs. For relatively low power loads, the absorbed radiation already raises the internal multilayer temperature to such a level that thermally induced interdiffusion in the multilayer changes the layered structure, and with prolonged exposure this can lead to severe imaging distortions.

The model described in chapter 5 provides a prediction for the period change and the amount of interface growth over time in Mo/Si multilayer structures when exposed to thermal loads. This model can predict the lifetime of the optics within a relatively short measurement if the temperature during usage is constant and well know. Since the diffusion coefficient can be described by the Arrhenius law, we are able to predict the lifetime for every temperature, if there are no structural changes expected. The model can also be used for multilayers with diffusion barriers, to observe the differences in thermal stability and lifetime for different systems.

The typical lifetime of multilayer optics demanded for EUVL applications is 3-10 years. According to the model described in chapter 5 a Mo/Si multilayer without any barrier layers will have a period change of several angstroms if kept at a temperature of 200°C. This period change will reduce the reflection at 13.5 nm to a few percent and is therefore unacceptable. Within this PhD project multilayer coatings with diffusion barriers have been developed which have shown not to change for several thousands of hours and which can meet the requirements for the industrial application.

A common diffusion barrier material is B_4C. This thesis has contributed to the understanding of the functioning of this diffusion barrier by showing, in chapter 4, that molybdenum boride compounds are formed at the interfaces. MoB is therefore suggested to be used as an alternative for Mo in multilayers. MoB/Si multilayer structures have a calculated reflectivity of approximately 66%[†], and the research presented in chapter 4 shows that the thermal stability of such multilayers would indeed be very promising.

In chapter 6 we learned from diffusion experiments that ion bombardment of a B_4C barrier layer during growth improves its quality as a diffusion barrier. If two B_4C diffusion barriers are applied, the diffusion coefficient reduces with an order of magnitude. When, in addition those B_4C barrier layers are treated by ions, the diffusion coefficient reduces again by a factor of 7. The data analysis showed that the improvement is a direct result of the densification of the B_4C layer, and not of increased chemical reactions at the interface. The direct link between barrier density and diffusion constant can be used to improve B_4C barrier layers and may be applied more generally for other diffusion barriers.

8.3 Radiation stability of multilayers

Thermal annealing is a very suitable technique to study the effects of thermally enhanced diffusion, as caused by the absorption of radiation by the optics. In addition to thermal damage due to diffusion, absorption of photons in a material may also have additional direct photochemical and physical effects. In chapter 7 we investigate the differences and similarities between damage induced by thermal annealing and damage induced by very intense, fs pulses of EUV radiation produced by a free electron laser. Although the timescale and absorbed energies in these two experiments were notably different, we observed the same basic damage mechanism. A similar study of Mo/Si multilayers, which is not included in this thesis but in reference [27], supports this similarity between the damage mechanism by radiation and damage by annealing, although the timing and threshold energies are very different.

In both the MoN/SiN as in the Mo/Si multilayers, the damage threshold for FEL radiation was related to melting of one of the constituent materials. In case of MoN/SiN, this material was MoN, while in case of Mo/Si this was Si. Below the damage threshold, no damage of our multilayers was observed, using the femtosecond pulses. Below this fluence they can therefore be used as sustainable optics in short wavelength free electron lasers.

The value of the damage threshold is also considered relevant, in for instance, EUV mask inspection tools, since these may employ high radiation densities. The mask, or reticle, in EUVL consist of a multilayer with a pattern made from an EUV-absorbing material on top of it. This pattern is very small and it could easily be affected by small errors in the multilayer or dust particles on top of the surface. To check these kind of errors, mask inspection is considered mandatory. During such inspection short (ns) but intense pulses of radiation may be needed to reduce the inspection time, dictated by the resolution required and the large mask surface area. The free electron laser conditions might thus be very representative for mask inspection procedures. Our work has given an indication for boundary conditions

---

[†] This was calculated using IMD, presuming the same roughness as Mo/Si multilayers, and a tabulated density of the MoB layer.

for such inspection, though commercial EUV inspection devices are still in an early phase of development.

8.4 Outlook

Based on the collective results in this thesis, several suggestions for further elementary studies on multilayer optics can be done. In chapter 5 we suggested that in the period before the parabolic growth law applies, reshaping or reformation of the interface could take place. These initial processes could be investigated by molecular dynamics simulations. In this case the deposition process of two layers could be simulated to obtain a realistic multilayer structure. After that, the temperature in this simulated structure will have to be raised to reveal the kind of compounds that are formed in the initial diffusion stages, e.g. minutes. Experimental verification of these compounds could be achieved via extended X-ray absorption fine structure (EXAFS) analysis or with low energy ion scattering (LEIS), both on well controlled few layer model systems which are annealed *in-situ*. The installation of LEIS inside one of the coating facilities at Rijnhuizen is planned within the CP3E project.

In future studies selectively reducing diffusion on one of the interfaces combined with *in-situ* annealing experiments could be used to study the individual interfaces. If the diffusion through one specific interface is further identified, the respective results will suggest specific diffusion barriers for each type of interface, to further improve the total multilayer stability and optical response. It should be noted that, as chapter 4 shows, the barrier can influence the diffusion properties of the multilayer dramatically, so chemical reactions between the barrier material and the Mo or Si layers should in this case be avoided.

An obvious valorization case in this respect is the further development of the basic physics that will enable a class of optics suited for the fourth generation of X-ray sources, namely soft X-ray free electron lasers (FEL). This class of sources is being developed world wide at increasing pace. Currently plans are being made to build an X-ray FEL at the Groningen University in The Netherlands. The FOM knowledge on radiation-robust multilayer optics is very valuable for this new FEL, and the research in this thesis has indicated pathways to further develop the physics to meet the stringent demands of this application.

To increase the damage threshold for optics for the short high intensity light pulses from a FEL, newly developed multilayers should meet three conditions. First of all, the materials should have a high melting point. Secondly, the reflectance should be high, to meet the required performance. Thirdly, the absorption in the material should be low, which will prevent the temperature to increase to the melting point. A good example of such a multilayer, which can be further studied in future high heat load applications (for instance FELS) is the Mo/SiC multilayer [53]. SiC has a melting temperature which is higher than that of Si (SiC: 2730°C, Si:1414°C), while it still has a reflection of 52% at normal incidence. The absorption in the SiC layer is slightly higher then the absorption of Si (see figure 1.3), but much lower than the absorption of for instance Mo_2N.

The methods to study diffusion on a nanometer scale could also be applied for other thin film applications in non-optical fields. Thin films will be increasingly important in energy research, for instance in the field of thin film solar cells and thin film batteries. The lifetime and functioning of these devices might critically depend on the ability to control interface diffusion processes, eventually down to the atomic level. The model to study diffusion on a nanometer scale, developed in this work, can be very useful to do fundamental research on diffusion in these two fields. This might fit within the plans for setting up a research institute of the type as currently foreseen with the Dutch Institute for Fundamental Energy Research, or DIFFER.

Chapter 9

Summary

Multilayered thin film structures are widely applied as reflective coatings for optical elements in the extreme ultraviolet wavelength regime. In this thesis we investigate the structural and chemical changes that occur in Mo/Si based multilayers under direct and indirect, radiation induced thermal loads and other heating schemes mimicking these causes. This thesis addresses thermally induced diffusion in such multilayers, focussing on reaction mechanisms at the interfaces and how these are modified in the presence of a diffusion barrier layer material. In addition, we address the effects of intense femtosecond laser pulses on the multilayer structure, and compare them to those resulting from purely thermal annealing.

A new, *in-situ* X-ray diffraction method is introduced to study diffusion induced interface growth and measure diffusion speeds in Mo/Si multilayers during thermal annealing. This method can determine the change in the interface thickness with a picometer accuracy, which is at least a factor of 10 better than previously used methods such as TEM. Because of the high accuracy it is possible to study diffusion at relatively low temperatures, at the very onset of interface growth. A diffusion-reaction model was developed to describe the interface growth. With this model the structural changes in the multilayer, and related lifetime of multilayer coated optics, can be predicted for temperatures at least up to 275°C.

In high temperature applications, the Mo layers may exhibit a quasi-amorphous or poly-crystalline structure, depending on the exact optical design as well as barrier layer thicknesses. Since interdiffusion speeds can depend on the crystallinity of a material, it is important to investigate the effects of the Mo crystalline structure on the interdiffusion speeds in Mo/Si multilayers, which was not studied before. In this thesis the crystallinity was shown to have a large influence on the diffusion speeds through the interfaces. The diffusion speeds through quasi-amorphous Mo appeared to be faster than through poly-crystalline Mo.

Apart from the crystalline structure of Mo, also the structure of, and chemical interactions with, barrier layer materials such as B_4C can influence the diffusion speeds in Mo/Si based multilayers. We have shown that for B_4C barrier layers, the formation of a molybdenum boride compound decreases the diffusion speed significantly, especially when the Mo layer is quasi-amorphous. In addition, when the density of the B_4C layer increases from 2.3 to 2.6 g/cm^3, the diffusion coefficient decreases with a factor of 7. Concluding, the diffusion properties of thin film multilayer structures are determined by both the structure *and* the chemical interactions of the individual (barrier-)layers.

Apart from the effects of thermal annealing, the damage mechanisms of intense femtosecond pulses are also investigated, to find a possible difference in damage mechanism between continuous heat loads and ultrafast pulsed heat loads. This investigation was performed on thermally stable MoN/SiN multilayers. We find that the damage mechanisms for annealing and pulsed irradiation are fundamentally the same. In both cases, the MoN layer dissociates and N_2 gas is released, which subsequently forms bubbles in the MoN layer which may lead to delamination.

Chapter 10

Samenvatting

Multilaagstructuren met lagen van enkele nanometers dik worden veel gebruikt als reflectieve coatings voor optische elementen in het extreem ultraviolet golflengtegebied. In dit proefschrift onderzoeken we de structurele en chemische veranderingen die tijdens verwarming, die door bestraling veroorzaakt kan zijn, plaatsvinden. Ook bespreken we thermisch geïnduceerde diffusie in deze multilaagstructuren, waarbij de focus ligt op de reacties op de grenslagen en hoe deze veranderen onder invloed van diffusiebarrières. Bovendien onderzoeken we de effecten van intense femtoseconde laser pulsen op de multilaagstructuur en vergelijken deze met de effecten van alleen thermische verwarming.

We introduceren een nieuwe X-ray diffractie methode om de door diffusie geïnduceerde interlaaggroei gedurende thermisch verwarmen *in-situ* te volgen en zo de diffusiesnelheden in Mo/Si multilagen te kunnen meten. Met deze methode kan de interlaaggroei tot op een picometer nauwkeurig bepaald worden, wat zeker een factor 10 beter is dan met vorige methoden zoals TEM. Door deze hoge precisie is het mogelijk om de diffusie te bestuderen op relatief lage temperaturen, vanaf het begin van het de interlaaggroei. Ook is er een model ontwikkeld dat de interlaaggroei beschrijft met een diffusie-reactie model. Dit model beschrijft de structurele veranderingen in de multilaag en de daaraan gerelateerde levensduur van de met een multilaag gecoate optieken. De structurele veranderingen kunnen met dit model worden beschreven tot op een temperatuur van tenminste 275°C.

Bij toepassingen waar een hoge temperatuur noodzakelijk is, kunnen de molybdeenlagen een quasi-amorfe of poly-kristallijne structuur hebben, afhankelijk van de dikte van de molybdeenlaag. Aangezien de interdiffusiesnelheid af kan hangen van de kristallijne structuur van het materiaal, is het belangrijk om de invloed van de kristallijne structuur van de Mo laag op de diffusiesnelheid in Mo/Si multilagen te onderzoeken, wat hiervoor nog niet gedaan was. In dit proefschrift laten we zien dat de kristallijne structuur van de Mo laag een grote invloed heeft op de diffusiesnelheid.

Behalve de kristallijne structuur van Mo, kunnen ook de structuur en de chemische interacties met diffusiebarrière materialen, zoals B_4C, de diffusiesnelheden in op Mo/Si gebaseerde multilagen beïnvloeden. Wij laten zien dat B_4C diffusiebarrières de diffusiesnelheden significant verlagen door vorming van molybdeen boride verbindingen, zeker wanneer Mo een quasi-amorfe structuur heeft. We laten ook zien dat een stijging van de B_4C dichtheid van 2.3 naar 2.6 g/cm^3 de diffusiecoëfficient doet afnemen met een factor 7. Concluderend, de diffusieeigenschappen van een dunnelaag multilaagstructuur worden bepaald door zowel de structuur als de chemische interacties van de individuele (barrière-)lagen.

Naast de effecten van thermische verwarming, hebben we ook de beschadigingsmechanismes bij bestraling met intense femtoseconde laserpulsen onderzocht. De verschillen in de beschadigingsmechanismes tussen continu verwarmen en ultrasnelle gepulseerde verwarming werd onderzocht in thermisch stabiele MoN/SiN multilagen. De beschadigingsmechanismen voor continu thermisch verwarmen en gepulseerde straling bleken fundamenteel hetzelfde te zijn. In beide gevallen dissocieert de MoN laag en komt er N_2 gas vrij, wat bellen maakt in de MoN laag en kan leiden tot delaminatie van de lagen.

Acknowledgements

This PhD thesis could not have been made without the help and support from many colleagues and friends. First I would like to thank my daily supervisor, Robbert, for all the discussions, the checking of my papers and the fun we had. Although you are very busy you always found time to help me whenever I needed it. Also the enthusiasm for the pies that I like to make was unrivaled. A big thank you also has to go to Andrey, you were always critical and always made time for lengthy scientific discussions, which have improved the quality of my thesis. Fred, I would like to thank you for giving me the opportunity to do my PhD in such a nice group. You were the one who helped me most by being the final critical check after the discussions between me, Andrey and Robbert.

Also the help from Erwin, Ryszard and Eric has been very valuable. Erwin, thanks for al the XPS analysis and the help with the interpretation of the data. Ryszard, thank you for collaborating with me on all the work described in chapter 7 and for inviting me into your home during my visit to Warschau to measure the data in figure 7.6. Eric, thank you for helping me to get coating time. I really enjoyed swimming with you during the lunch break.

The other PhD students and the postdocs in the nSI group contributed with scientific help or advise and/or by making my stay at Rijnhuizen very enjoyable. Therefore a big Thank you! goes to: Tim, Toine, Michael, Mike, Eddie, Steven, Marko, Rolf, Igor and Alexey. Some of you I would like to thank separately. Ileana, your PhD work has been the starting point for mine, thanks for al the help in the first year and for agreeing to be my paranimf. Véronique, you were my only female group member after Ileana left, thank you for everything, it was nice that at least one person noticed that I had a new pair of shoes. Jeroen, you started as a student, where you helped me a lot with getting to grips with the new *in-situ* annealing setup. But perhaps even more importantly, thank you for al the great laughs. I would like to thank Hirokazu for introducing me to Japanese cinema, you have taught me that there is more than Ghibli manga. And finally, I would like to thank Juequan for the last year of sharing a room at work and introducing me to your wife and son, I have never seen a more

”funny guy” as your little one!

All the experiments described in this thesis would not have been possible without the excellent technical support which is present in the nSI group. All of the technicians in this group are always ready to help you with everything. Especially the help with the annealing setup, the diffractometer (which I like to lovingly call ”Cuka”) and the production of the multilayers was extremely valuable. For this I would like to thank: Arend-Jan, Ronald, Machiel, Frenk, Kees, Santi, Peter, Rob and Fabian.

I have enjoyed my time at Rijnhuizen very much. I liked going swimming in the break, thanks for all the people who joined me and/or drove me there. It was fun being part of the Ontspannings Vereniging Rijnhuizen (OVR) for the last two years. And the park is an inspiring place to walk and read papers in the summer, especially when the cat was kind enough to honor me with her presence. Thanks to everyone for making Rijnhuizen such a wonderful place to work!

In the sometimes stressful time of my PhD it is nice to spend a nice evening or a day in the weekend with family and friends. In this light I would like to thank: Margriet, Tim, Eric (thanks for the LaTeX support!), Lianne, Jose, Bas, Haili, Luiz, Robbie and Vera. I also would like to give a very warm thank you to my parents, Ron and Hannie, they have always supported and stimulated me, during my PhD, but also during all the years before that. Finally, a very special thanks to Willem, you are always there, whether I was frustrated when things did not go as planned or happy because things did go according to plan, I could always count on you to listen or be happy for me.

Saskia
Z

Curriculum Vitae

Saskia Bruijn was born on the 30th of November 1980 in Strijen. She started her secondary school in 1993 in Rotterdam at the Sint-Montfortcollege, where she graduated cum laude in 1999. From 1999-2006 she studied general sciences at the Radboud University in Nijmegen. During this time two internships were carried out at this university, one in the solid state chemistry group and one in the applied physics group. In the solid state chemistry group she worked on the development of a Schlieren microscope in order to study diffusion around a growing KDP crystal. During the second internship she worked on diamond growth on Mo substrates, which among other things were tested for corrosion resistance. In 2006, she started her PhD research at the FOM Institute for Plasma Physics Rijnhuizen in Nieuwegein under the supervision of her promotor Professor Fred Bijkerk. A selection of the results of this research can be read in this thesis.

List of publications

This thesis is based on the following publications:

- **Chapter 1:**
  S. Bruijn, R.W.E. van de Kruijs, A.E. Yakshin, and F. Bijkerk, ”The Effect of Mo Crystallinity on Diffusion through the Si-on-Mo Interface in EUV Multilayer Systems,” *Defect and Diffusion Forum* **283-286**, 657-661 (2009).
- **Chapter 2:**
  S. Bruijn, R.W.E. van de Kruijs, A.E. Yakshin, E. Zoethout, and F. Bijkerk, ”Thermally induced decomposition of B_4C barrier layers in Mo/Si multilayer structures,” *Surface and Coatings Technology* **205**, 2469-2473 (2010).
- **Chapter 3:**
  S. Bruijn, R.W.E. van de Kruijs, A.E. Yakshin, and F. Bijkerk, ”*In-situ* study of the diffusion-reaction mechanism in Mo/Si multilayered films,” *Applied Surface Science* **257**, 2707-2711 (2011).
- **Chapter 4:**
  S. Bruijn, R.W.E. van de Kruijs, A.E. Yakshin, and F. Bijkerk, ”Ion assisted growth of B_4C diffusion barrier layers in Mo/Si multilayered structures” *submitted*.
- **Chapter 5:**
  R. Sobierajski, S. Bruijn, A.R. Khorsand, E. Louis, R.W.E. van de Kruijs, T. Burian, J. Chalupsky, J. Cihelka, A. Gleeson, J. Grzonka, E.M. Gullikson, V. Hajkova, S. Hau-Riege, L. Juha, M. Jurek, D. Klinger, J. Krzywinski, R. London, J.B. Pelka, T. Plocinski, M. Rasinski, K. Tiedtke, S. Toleikis, L. Vysin, H. Wabnitz, and F. Bijkerk, ”Damage mechanisms of MoN/SiN multilayer optics for next-generation pulsed XUV light sources,” *Optics Express* **19**, 193-205 (2011).

Other publication:

- A.R. Khorsand, R. Sobierajski, E. Louis, S. Bruijn, E.D. van Hattum, R.W.E. van de Kruijs, M. Jurek, D. Klinger, J.B. Pelka, L. Juha, T. Burian, J. Chalupsky, J. Cihelka, V. Hajkova, L. Vysin, U. Jastrow, N. Stojanovic, S. Toleikis, H. Wabnitz, K. Tiedtke, K. Sokolowski-Tinten, U. Shymanovich, J. Krzywinski, S. Hau-Riege, R. London, A. Gleeson, E.M. Gullikson, and F. Bijkerk, ”Single shot damage mechanism of Mo/Si multilayer optics under intense pulsed XUV-exposure,” *Optics Express* **18**, 700-712 (2010).

Patent:

- R.W.E. van de Kruijs, S. Bruijn, T. Tsarfati, A.E. Yakshin, F. Bijkerk and E. Louis, ”Reduction of diffusion at Mo/Si interfaces by boride barriers and boron passivation” DE 102009032751 A1, priority date 16 September 2008.

Bibliography

[1] X.C. Wang, W.B. Mi, E.Y. Jiang, and H.L. Bai. Structure and mechanical properties of titanium nitride/carbon nitride multilayers. *Applied Surface Science*, 255(7):4005–4010, 2009.

[2] M. Baraket, D. Mercs, Z. G. Zhang, and C. Coddet. Mechanical and tribological properties of CrN/Ag and CrSiN/Ag nanoscale multilayers. *Surface and Coatings Technology*, 204(15):2386, 2010.

[3] M. N. Baibich, J. M. Broto, A. Fert, F.N. Van Dau, F. Petroff, P. Etienne, G. Creuzet, A. Friederich, and J. Chazelas. Giant magnetoresistance of (001)Fe/(001)Cr magnetic superlattices. *Physical Review Letters*, 61(21): 2472, 1988.

[4] G.S. Smith. Structural color of Morpho butterflies. *American Journal of Physics*, 77(11):1010, 2009.

[5] S. Kinoshita, S. Yoshioka, and K. Kawagoe. Mechanisms of structural colour in the morpho butterfly: Cooperation of regularity and irregularity in an iridescent scale. *Procedings Royal Society London*, B269:1417, 2002.

[6] P. Vukusic and J. Roy Sambles. Photonic structures in biology. *Nature*, 424 (6950):852, 2003.

[7] S. Berthier, E. Charron, and A. Da Silva. Determination of the cuticle index of the scales of the iridescent butterfly Morpho menelaus. *Optics Communications*, 228(4-6):349, 2003.

[8] T. R. Matin, M. K. Leong, B. Y. Majlis, and I. C. Gebeshuber. Correlating nanostructures with function: Structural colors on the wings of a malaysian bee. *AIP Conference Proceedings*, 1284(1):5, 2010.

[9] D. Attwood. *Soft X-rays and Extreme Ultraviolet Radiation - Principles and Applications*. Cambridge University Press, Cambridge, 1999.

[10] E. Zoethout, G. Sipos, R. W. E. van de Kruijs, A. E. Yakshin, E. Louis, S. Muellender, and F. Bijkerk. Stress mitigation in Mo/Si multilayers for EUV lithography. volume 5037, page 872, 2003.

[11] J.P. Delaboudinire, G.E. Artzner, J. Brunaud, A.H. Gabriel, J.F. Hochedez,

F. Millier, X.Y. Song, B. Au, et al. EIT: Extreme-ultraviolet imaging telescope for the SOHO mission. *Solar Physics*, 162(1):291, 1995.

[12] E. Hecht. *Optics, fourth edition.* Pearson education, San Francisco, 2002.

[13] V. Bakshi. *EUV Lithography*. SPIE John Wiley and Sons, Inc., Washington, 2009.

[14] S. Wurm. Lithography perspective for the 22 nm half-pitch node. *Solid State Technology*, page 978, 2010.

[15] J. Hollenshead and L. Klebanoff. Modeling radiation-induced carbon contamination of extreme ultraviolet optics. *Journal of Vacuum Science and Technology B*, 24(1):64, 2006.

[16] J. Chen, E. Louis, C.J. Lee, H. Wormeester, R. Kunze, H. Schmidt, D. Schneider, R. Moors, et al. Detection and characterization of carbon contamination on EUV multilayer mirrors. *Optics Express*, 17(19):16969, 2009.

[17] D.J.W. Klunder, M.M.J.W. van Herpen, V.Y. Banine, and K. Gielissen. Debris mitigation and cleaning strategies for Sn-based sources for EUV lithography. volume 5751, page 943, 2005.

[18] K. Motai, H. Oizumi, S. Miyagaki, I. Nishiyama, A. Izumi, T. Ueno, Y. Miyazaki, and A. Namiki. Atomic hydrogen cleaning of Ru-capped EUV multilayer mirror. volume 6517, pages 65170F–8, 2007.

[19] S. Bajt, H.N. Chapman, N. Nguyen, J. Alameda, J.C. Robinson, M. Malinowski, E. Gullikson, A. Aquila, et al. Design and performance of capping layers for extreme-ultraviolet multilayer mirrors. *Applied Optics*, 42(28):5750, 2003.

[20] T. Tsarfati, E. Zoethout, R.W.E. van de Kruijs, and F. Bijkerk. Growth and sacrificial oxidation of transition metal nanolayers. *Surface Science*, 603(7): 1041, 2009.

[21] M.G. Pelizzo, A.J. Corso, G. Monaco, P. Nicolosi, M. Suman, P. Zuppella, and D. Cocco. Multilayer optics to be used as FEL fundamental suppressors for harmonics selection. *Nuclear Instruments and Methods in Physics Research Section A*, In Press, Corrected Proof, 2011.

[22] H.N. Chapman and K.A. Nugent. Coherent lensless X-ray imaging. *Nature Photonics*, 4(12):833, 2010.

[23] H.N. Chapman, S.P. Hau-Riege, M.J. Bogan, S. Bajt, A. Barty, S. Boutet, S. Marchesini, M. Frank, et al. Femtosecond time-delay X-ray holography. *Nature*, 448(7154):676, 2007.

[24] S. Marchesini, H. He, H.N. Chapman, S.P. Hau-Riege, A. Noy, M.R. Howells, U. Weierstall, and J.C.H. Spence. X-ray image reconstruction from a diffraction pattern alone. *Physical Review B*, 68(14):140101, 2003.

[25] W. Ackermann, G. Asova, V. Ayvazyan, A. Azima, N Baboi, J. Bahr, V. Balandin, B. Beutner, et al. Operation of a free-electron laser from the extreme ultraviolet to the water window. *Nature Photonics*, 1(6):336, 2007.

[26] K. Tiedtke, A. Azima, N. von Bargen, L. Bittner, S. Bonfigt, S. Dusterer, B. Faatz, U. Fruhling, et al. The soft X-ray free-electron laser flash at desy: beamlines, diagnostics and end-stations. *New Journal of Physics*, 31(2): 023029, 2009.

[27] A.R. Khorsand, R. Sobierajski, E. Louis, S. Bruijn, E.D. van Hattum, R.W.E. van de Kruijs, M. Jurek, D. Klinger, et al. Single shot damage mechanism of Mo/Si multilayer optics under intense pulsed XUV-exposure. *Optics Express*, 18(2):700, 2010.

[28] S. Yulin, T. Feigl, T. Kuhlmann, N. Kaiser, A.I. Fedorenko, V.V. Kondratenko, O.V. Poltseva, V. A. Sevryukova, et al. Interlayer transition zones in Mo/Si superlattices. *Journal of Applied Physics*, 92(3):1216, 2002.

[29] R. S. Rosen, D. G. Stearns, M. A. Viliardos, M. E. Kassner, S. P. Vernon, and Y. D. Cheng. Silicide layer growth-rates in Mo/Si multilayers. *Applied Optics*, 32(34):6975, 1993.

[30] R.W.E. van de Kruijs, E. Zoethout, A.E. Yakshin, I. Nedelcu, E. Louis, H. Enkisch, G. Sipos, S. Mullender, and F. Bijkerk. Nano-size crystallites in Mo/Si multilayer optics. *Thin Solid Films*, 515(2):430, 2006.

[31] I. Nedelcu, R.W.E. van de Kruijs, A.E. Yakshin, and F. Bijkerk. Thermally enhanced interdiffusion in Mo/Si multilayers. *Journal of Applied Physics*, 103 (8):083549, 2008.

[32] H. Nakajima, M. Ikebe, Y. Muto, S. Yamaguchi, and H. Fujimori. Diffusion behaviour and superconducting properties of sputtered-deposited Mo/Si and MoN/SiN multilayers. *MRS Int'l. on Adv. Mats.*, 10:405, 1989.

[33] S. Braun, H. Mai, M. Moss, R. Scholz, and A. Leson. Mo/Si multilayers with different barrier layers for applications as extreme ultraviolet mirrors. *Japanese Journal of Applied Physics*, 41:4074, 2002.

[34] F.R. de Boer, R. Boom, W.C.M. Mattens, A.R. Miedema, and A.K. Niessen. *Cohesion in metals. Transition metal alloys*. North-Holland, 1988.

[35] I. Nedelcu, R.W.E. van de Kruijs, A.E. Yakshin, and F. Bijkerk. Temperature-dependent nanocrystal formation in Mo/Si multilayers. *Physical Review B*, 76 (24):245404–8, 2007.

[36] V. I. T. A. de Rooij-Lohmann, A. W. Kleyn, F. Bijkerk, H. H. Brongersma, and A. E. Yakshin. Diffusion and interaction studied nondestructively and in real-time with depth-resolved low energy ion spectroscopy. *Applied Physics Letters*, 94(6):063107, 2009.

[37] T. Voss, A. Strohm, S. Matics, P. Scharwaechter, and W. Frank. A novel technique for measuring diffusivities of short-lived radioisotopes in solids. *Zeitschrift Fur Metallkunde*, 93(10):1077, 2002.

[38] J. DuMond and J.P. Youtz. An X-ray method of determining rates of diffusion in the solid state. *Journal of Applied Physics*, 11(5):357, 1940.

[39] W.H. Wang, H.Y. Bai, M. Zhang, J. H. Zhao, X. Y. Zhang, and W. K. Wang. Interdiffusion in nanometer-scale multilayers investigated by in situ low-angle X-ray diffraction. *Physical Review B*, 59(16):10811, 1999.

[40] H. Nakajima, H. Fujimori, and M. Koiwa. Interdiffusion and structural relaxation in Mo/Si multilayer films. *Journal of Applied Physics*, 63(4):1046, 1988.

[41] H. Schmidt, M. Gupta, T. Gutberlet, J. Stahn, and M. Bruns. How to measure atomic diffusion processes in the sub-nanometer range. *Acta Materialia*, 56 (3):464, 2008.

[42] U. Gosele and K.N. Tu. Growth kinetics of planar binary diffusion couples:

"thin-film case" versus "bulk cases". *Journal of Applied Physics*, 53(4):3252–3260, 1982.

[43] W. Jost. *Diffusion in solids, liquids, gases*. Academic press inc., New York, 1952.

[44] T. Bottger, D. C. Meyer, P. Paufler, S. Braun, M. Moss, H. Mai, and E. Beyer. Thermal stability of Mo/Si multilayers with boron carbide interlayers. *Thin Solid Films*, 444(1-2):165, 2003.

[45] S. Bruijn, R.W.E. van de Kruijs, A.E. Yakshin, E. Zoethout, and F. Bijkerk. Thermally induced decomposition of B_4C barrier layers in Mo/Si multilayer structures. *Surface and Coatings Technology*, 205(7):2469, 2010.

[46] V.I.T.A. de Rooij-Lohmann, A.E. Yakshin, R.W.E. van de Kruijs, E. Zoethout, A.W. Kleyn, E.G. Keim, M. Gorgoi, F. Schafers, et al. Enhanced diffusion upon amorphous-to-nanocrystalline phase transition in Mo/B_4C/Si layered systems. *Journal of Applied Physics*, 108(1):014314–5, 2010.

[47] I. Nedelcu, R.W.E. van de Kruijs, A.E. Yakshin, and F. Bijkerk. Microstructure of Mo/Si multilayers with B_4C diffusion barrier layers. *Applied Optics*, 48(2): 155, 2009.

[48] A. Patelli, J. Ravagnan, V. Rigato, G. Salmaso, D. Silvestrini, E. Bontempi, and L.E. Depero. Structure and interface properties of Mo/B_4C/Si multilayers deposited by rf-magnetron sputtering. *Applied Surface Science*, 238(1-4):262, 2004.

[49] S. Bruijn, R. W. E. van de Kruijs, A. E. Yakshin, and F. Bijkerk. The effect of Mo crystallinity on diffusion through the Si-on-Mo Interface in EUV multilayer systems. *Defect and Diffusion Forum*, 283:657, 2009.

[50] H. Takenaka and T. Kawamura. Thermal stability of Mo/C/Si/C multilayer soft X-ray mirrors. *Journal of Electron Spectroscopy and Related Phenomena*, 80: 381, 1996.

[51] S. Yulin, N. Benoit, T. Feigl, and N. Kaiser. Interface-engineered EUV multilayer mirrors. *Microelectronic Engineering*, 83(4-9):692, 2006.

[52] N. Kaiser, S.A. Yulin, and T. Feigl. Si-based multilayers with high thermal stability. volume 4146, page 91, 2000.

[53] S. A. Bajt and D. G. Stearns. High-temperature stability multilayers for extreme-ultraviolet condenser optics. *Applied Optics*, 44(36):7735, 2005.

[54] Y. Ishii, H. Takenaka, T. Kawamura, T. Haga, and H. Kinoshita. Thermal stability of Mo-based multilayer X-ray mirrors. volume 2015, page 132, 1994.

[55] S. Bajt, D. G. Stearns, and P. A. Kearney. Investigation of the amorphous-to-crystalline transition in Mo/Si multilayers. *Journal of Applied Physics*, 90(2): 1017, 2001.

[56] Antonio Cervellino, Cinzia Giannini, and Antonietta Guagliardi. Determination of nanoparticle structure type, size and strain distribution from X-ray data for monatomic f.c.c.-derived non-crystallographic nanoclusters. *Journal of Applied Crystallography*, 36(5):1148, 2003.

[57] R. Resel, E. Tamas, B. Sonderegger, P. Hofbauer, and J. Keckes. A heating stage up to 1173K for X-ray diffraction studies in the whole orientation space. *Journal of Applied Crystallography*, 36:80, 2003.

[58] A. L. Patterson. The scherrer formula for X-ray particle size determination. *Physics Review*, 56(10):978, 1939.

[59] B.E. Warren. *X-Ray Diffraction*. Dover pulblications, inc., New York, 1990.

[60] B.D. Cullity and S.R. Stock. *Elements of X-ray Diffraction*. Prentice Hall, New Jersey, 2001.

[61] D.L. Windt. IMD - software for modeling the optical properties of multilayer films. *Computers in Physics*, 12(4):360, 1998.

[62] H.J. Voorma. *Mo/Si Multilayer Optics for Micro-Lithography*. PhD thesis, Delft University of Technology, 1997.

[63] B.Q. Wua and A. Kumar. Extreme ultraviolet lithography: A review. *Journal of Vacuum Science and Technology B*, 25(6):1743, 2007.

[64] E. Louis, H.J. Voorma, N.B. Koster, F. Bijkerk, Y.Y. Platonov, S.Y. Zuev, S.S. Andreev, E.A. Shamov, and N. N. Salashchenko. Multilayer coated reflective optics for extreme uv lithography. *Microelectronic Engineering*, 27(1-4):235, 1995.

[65] R. Schlatmann, C. Lu, J. Verhoeven, E. J. Puik, and M. J. van der Wiel. Modification by Ar and Kr ion bombardment of Mo/Si X-ray multilayers. *Applied Surface Science*, 78(2):147, 1994.

[66] J.M. Poate, K.N. Tu, and J.W. Mayter. *Thin Films-interdiffusion and reactions*. John Wiley and Sons, inc., New York, 1978.

[67] E.N. Zubarev, A.V. Zhurba, V.V. Kondratenko, V.I. Pinegyn, V.A. Sevryukova, S.A. Yulin, T. Feigl, and N. Kaiser. The structure, diffusion and phase formation in Mo/Si multilayers with stressed Mo layers. *Thin Solid Films*, 515(17):7011, 2007.

[68] P. Jonnard, I. Jarrige, R. Benbalagh, H. Maury, J. M. Andre, Z. Dankhazi, and G. Rolland. Physico-chemical and X-ray optical characterizations of a Mo/Si multilayer interferential mirror upon annealing. *Surface Science*, 589 (1-3):164–172, 2005.

[69] M. Ishino, O. Yoda, H. Takenaka, K. Sano, and M. Koike. Heat stability of Mo/Si multilayers inserted with compound layers. *Surface and Coatings Technology*, 169-170:628, 2003.

[70] S. Bajt, J. Alameda, T. Barbee, W.M. Clift, J.A. Folta, B. Kaufman, and E. Spiller. Improved reflectance and stability of Mo/Si multilayers. *Opitcial engineering*, 41:1797, 2002.

[71] H. Maury, P. Jonnard, J.M. Andre, J. Gautier, M. Roulliay, F. Bridou, F. Delmotte, M.F. Ravet, et al. Non-destructive X-ray study of the interphases in Mo/Si and Mo/B_4C/Si/B_4C multilayers. *Thin Solid Films*, 514(1-2):278, 2006.

[72] E.J. Chi, J. Shim, J. Kwak, and H. Baik. Silicide formation by solid-state diffusion in Mo/Si multilayer thin films. *Journal of Materials Science*, 31(13):3567, 1996.

[73] S. Cho, S. Choi, S.C. Hong, Y. Kim, J.B. Ketterson, B.J. Kim, Y. C. Kim, and J.H. Jung. Ferromagnetism in Mn-doped Ge. *Physical Review B*, 66 (3):033303, 2002.

[74] Ueda Kenji, Tabata Hitoshi, and Kawai Tomoji. Magnetic and electric properties of transition-metal-doped ZnO films. *Applied Physics Letters*, 79(7):988,

2001.

[75] P. Heitjans and S. Indris. Diffusion and ionic conduction in nanocrystalline ceramics. *Journal of Physics-Condensed Matter*, 15(30):R1257, 2003.

[76] S.C. Jeong, I. Katayama, H. Kawakami, H. Ishiyama, H. Miyatake, M. Sataka, A. Iwase, S. Okayasu, et al. Simulation study on the measurements of diffusion coefficients in solid materials by short-lived radiotracer beams. *Japense Journal of Applied Physics*, 42(7A):4576, 2003.

[77] L. Reimer and H. Kohl. *Transmission Electron Microscopy*. Springer science, New-York, 2008.

[78] A.E. Yakshin, E. Louis, P.C. Görts, E.L.G. Maas, and F. Bijkerk. Determination of the layered structure in Mo/Si multilayers by grazing incidence X-ray reflectometry. *Physica B: Condensed Matter*, 283(1-3):143, 2000.

[79] David L. Lide, editor. *CRC Handbook of Chemistry and Physics, 90th Edition*. 2009-2010.

[80] K. Hiruma, S. Miyagaki, H. Yamanashi, Y. Tanaka, and I. Nishiyama. Performance and quality analysis of Mo-Si multilayers formed by ion-beam and magnetron sputtering for extreme ultraviolet lithography. *Thin Solid Films*, 516 (8):2050, 2008.

[81] Marcel Salamon, Andreas Strohm, Thilo Voss, Pauli Laitinen, Riihim, auml, Iiro ki, Sergiy Divinski, Werner Frank, auml, is, auml, Jyrki nen, and Helmut Mehrer. Self-diffusion of silicon in molybdenum disilicide. *Philosophical Magazine*, 84(8):737, 2004.

[82] M. Salamon and H. Mehrer. Diffusion in molybdenum disilicide. *Zeitschrift Fur Metallkunde*, 96(8):833, 2005.

[83] W.G. Sloof, O. B. Loopstra, Th H. De Keijser, and E. J. Mittemeijer. Diffusion and structural relaxation in amorphous Mo/Si multilayers. *Scripta Materialia*, 20:1683, 1986.

[84] A. E. Yakshin, R. W. E. van de Kruijs, I. Nedelcu, E. Zoethout, E. Louis, F. Bijkerk, H. Enkisch, and S. Mullender. Enhanced reflectance of interface engineered mo/si multilayers produced by thermal particle deposition. volume 6517, page 65170I, 2007.

[85] R. Stuik, E. Louis, A. E. Yakshin, P. C. Gorts, E. L. G. Maas, F. Bijkerk, D. Schmitz, F. Scholze, G. Ulm, and M. Haidl. Peak and integrated reflectivity, wavelength and gamma optimization of Mo/Si, and Mo/Be multilayer, multielement optics for extreme ultraviolet lithography. *J. Vac. Sci. Technol. B*, 17:2998–3002, 1999.

[86] V. I. T. A. de Rooij-Lohmann, L. W. Veldhuizen, E. Zoethout, A. E. Yakshin, R. W. E. van de Kruijs, B. J. Thijsse, M. Gorgoi, F. Schafers, and F. Bijkerk. Chemical interaction of B_4C, B, and C with Mo/Si layered structures. *Journal of Applied Physics*, 108(9):094314, 2010.

[87] M.A. Nicolet. Diffusion barriers in thin films. *Thin Solid Films*, 52(3):415, 1978.

[88] W.H. Lee, Y.L. Kuo, H.J. Huang, and C. Lee. Effect of density on the diffusion barrier property of tiN_x films between Cu and Si. *Materials Chemistry and Physics*, 85(2-3):444, 2004.

[89] Ying Wang, Fei Cao, Lei Shao, and Ming-hui Ding. Diffusion barrier capability

of Zr-Si films for copper metallization with different substrate bias voltage. *Thin Solid Films*, 517(18):5593, 2009.

[90] P. Pyykk and M. Atsumi. Molecular single-bond covalent radii for elements 1118. *Chemistry A European Journal*, 15(1):186, 2008.

[91] P. Heitjans and J. Krger, editors. *Diffusion in Condensed Matter: Methods, Materials, Models*. Springer, Berlin, 2005.

[92] James F. Ziegler, Jochen P. Biersack, and Matthias D. Ziegler. *SRIM - The Stopping and Range of Ions in Matter*. 2008.

[93] T. Shintake, H. Tanaka, T. Hara, T. Tanaka, K. Togawa, M. Yabashi, Y. Otake, Y. Asano, et al. A compact free-electron laser for generating coherent radiation in the extreme ultraviolet region. *Nature Photonics*, 2(9):555, 2008.

[94] E. Allaria, C. Callegari, D. Cocco, W.M. Fawley, M. Kiskinova, C. Masciovecchio, and F. Parmigiani. The FERMI@Elettra free-electron-laser source for coherent X-ray physics: photon properties, beam transport system and applications. *New Journal of Physics*, 12(7):075002, 2009.

[95] P. Balcou, R. Haroutunian, S. Sebban, G. Grillon, A. Rousse, G. Mullot, J. P. Chambaret, G. Rey, et al. High-order-harmonic generation: towards laser-induced phase-matching control and relativistic effects. *Applied Physics B: Lasers and Optics*, 74(6):509, 2002.

[96] S. Kazamias, D. Douillet, F. Weihe, C. Valentin, A. Rousse, S. Sebban, G. Grillon, F. Aug, et al. Global optimization of high harmonic generation. *Physical Review Letters*, 90(19):193901, 2003.

[97] B. Rus, T. Mocek, A. R. Prg, M. Kozlov, G. Jamelot, A. Carillon, D. Ros, D. Joyeux, and D. Phalippou. Multimillijoule, highly coherent X-ray laser at 21 nm operating in deep saturation through double-pass amplification. *Physical Review A*, 66(6):063806, 2002.

[98] S. Heinbuch, M. Grisham, D. Martz, and J. J. Rocca. Demonstration of a desk-top size high repetition rate soft X-ray laser. *Optics Express*, 13(11): 4050, 2005.

[99] B. Nagler, U. Zastrau, R. R. Faustlin, S.M. Vinko, T. Whitcher, A.J. Nelson, R. Sobierajski, et al. Turning solid aluminium transparent by intense soft X-ray photoionization. *Nature Physics*, 5(9):693, 2009.

[100] A.J. Nelson, S. Toleikis, H. Chapman, S. Bajt, J. Krzywinski, J. Chalupsky, L. Juha, J. Cihelka, et al. Soft X-ray free electron laser microfocus for exploring matter under extreme conditions. *Optics Express*, 17(20):18271, 2009.

[101] R. Sobierajski, M. Jurek, D. Klinger, J. Krzywinski, J.B. Pelka, H. Chapman, S.P. Hau-Riege, R. London, et al. Evolution of optical properties of surfaces under influence of ultra short pulses of intense EUV radiation. *HASYLAB Annual Report*, page 395, 2006.

[102] F. Barkusky, A. Bayer, S. Dring, P. Grossmann, and K Mann. Damage threshold measurements on EUV optics using focused radiation from a table-top laser produced plasma source. *Optics Express*, 18(5):4346, 2010.

[103] E. Louis, H.J. Voorma, N.B. Koster, L. Shmaenok, F. Bijkerk, R. Schlatmann, J. Verhoeven, Y.Y. Platonov, et al. Enhancement of reflectivity of multilayer mirrors for soft X-ray projection lithography by temperature optimization and

ion bombardment. *Microelectronic Engineering*, 23(1-4):215, 1994.

[104] E. Louis, A.E. Yakshin, P.C. Goerts, S. Oestreich, R. Stuik, E.L.G. Maas, M. J. H. Kessels, F. Bijkerk, M. Haidl, S. Muellender, M. Mertin, D. Schmitz, F. Scholze, and G. Ulm. Progress in mo/si multilayer coating technology for euvl optics. volume 3997, page 406, 2000.

[105] H.J. Voorma, E. Louis, F. Bijkerk, and S. Abdali. Angular and energy dependence of ion bombardment of Mo/Si multilayers. *Journal of Applied Physics*, 82(4):1876, 1997.

[106] E.P. Donovan, G.K. Hubler, M.S. Mudholkar, and L.T. Thompson. Ion-beam-assisted deposition of molybdenum nitride films. *Surface and Coatings Technology*, 66(1-3):499, 1994.

[107] R. Kärcher, L. Ley, and R.L. Johnson. Electronic structure of hydrogenated and unhydrogenated amorphous SiN_x $(0 < x < 1.6)$: A photoemission study. *Physical Review B*, 30(4):1896, 1984.

[108] I. Kusunoki, T. Takaoka, Y. Igari, and K. Ohtsuka. Nitridation of a Si(100) surface by 100-1000 ev $\text{N}_2{}^+$ ion beams. *The Journal of Chemical Physics*, 101(9):8238, 1994.

[109] K. Tiedtke, J. Feldhaus, U. Hahn, U. Jastrow, T. Nunez, T. Tschentscher, S.V. Bobashev, A.A. Sorokin, et al. Gas detectors for X-ray lasers. *Journal of Applied Physics*, 103(9):094511, 2008.

[110] S.P. Hau-Riege, R.A. London, H.N. Chapman, and M. Bergh. Soft-X-ray free-electron-laser interaction with materials. *Physical Review E*, 76(4):046403, 2007.

[111] J. Chalupsk, L. Juha, J. Kuba, J. Cihelka, V. Hjkov, S. Koptyaev, J. Krsa, A. Velyhan, et al. Characteristics of focused soft X-ray free-electron laser beam determined by ablation of organic molecular solids. *Optics Express*, 15(10): 6036, 2007.

[112] J. M. Liu. Simple technique for measurements of pulsed Gaussian-beam spot sizes. *Optics Letters*, 7(5):196, 1982.

[113] Hermann Jehn and Peter Ettmayer. The molybdenum-nitrogen phase diagram. *Journal of the Less Common Metals*, 58(1):85, 1978.

[114] K. Frisk. A thermodynamic evaluation of the Cr-N, Fe-N, Mo-N and Cr-Mo-N systems. *Calphad*, 15(1):79, 1991.

[115] C. Wagner, N. Harned, P. Kuerz, M. Lowisch, H. Meiling, D. Ockwell, R. Peeters, K. van Ingen-Schenau, E. van Setten, J. Stoeldraijer, and B. Thuering. EUV into production with ASML's NXE platform. volume 7636, page 76361H, 2010.

[116] R. de Leeuw. EUV into production with ASML's NXE platform, 2010.